LINEAR PROPERTIES OF THE CROSS-FIELD ION ACOUSTIC INSTABILITY IN A DOUBLE PLASMA DEVICE

BY

CLEMENS ARNOLD DEMPERS

Submitted in partial fulfilment of
the requirements for the degree of
Master of Science
in the
Department of Physics,
University of Natal.

Durban
March 1990

To my Parents

PREFACE

The experimental work described in this thesis was carried out at the Plasma Physics Research Institute at the University of Natal, Durban, from March 1986 to November 1989 under the supervision of Professor P.J. Barrett.

These studies represent the original work by the author and have not been submitted in any form to another University. Where use was made of the work of others it has been duly acknowledged in the text.

ACKNOWLEDGEMENTS

I wish to thank my supervisor, Professor P.J. Barrett , for his guidance and Professors M.A. Hellberg and R. Bharuthram for many helpful discussions. Dr. M.J. Alport, Dr R.G. Greaves and Mr. E.G. van Niekerk provided valuable assistance and advice on the experimental side of this project.

The staff of the Physics Department workshop provided much needed technical assistance and particular thanks to Mr. W. de Beer and Mr. A. Atkinson.

I appreciate the hard work and encouragement from Cindy Simon, and I am also specially grateful to my Parents for their unfailing support and understanding.

Finally, I would like to thank the Council for Scientific and Industrial Research and the Atomic Energy Corporation for their financial support for the duration of this work.

ABSTRACT

This thesis deals with the dependence of the linear spatial growth rate of the cross-field ion acoustic instability on various plasma parameters. A kinetic theory model, with elastic and inelastic ion-neutral collisions included, is presented and used to conduct a numerical survey of the instability. The growth rate is computed as a function of distance into the plasma, taking into account the attenuation of the ion beam by charge exchange collisions. Further calculations show the variation in growth rate as a function of the following quantities: electron and ion beam temperature, electron density, beam velocity, background ion temperature, magnetic field, the angle between magnetic field direction and wave vector and the finite width of the plasma.

The instability was observed in a double plasma device where an ion beam was passed through a background of stationary magnetized electrons. The magnetic field was sufficiently weak to allow approximately rectilinear ion motion. The growth rate of the wave was studied using interferometer techniques. It was identified by the dispersion relation as the cross-field ion acoustic wave propagating as the slow mode of the beam. It was found that the background ions play an important role in determining the phase velocity. Experimental data of the growth rate dependence on wave number, beam velocity and magnetic field strength were found to be well described by the theoretical model. The growth rate dependence of magnetic field direction on plasma width was furthermore found to be in qualitative agreement with the model.

Contents

List of Symbols

Roman Symbols

A	Probe collecting area
b	$\frac{1}{2}(k_\perp \rho_e)^2$
B	Magnetic field
c	Speed of light
C_e	Electron thermal velocity
C_{ib}	Beam ion thermal velocity
C_{io}	Rest ion thermal velocity
C_s	Ion sound speed
D	Plasma width in the z-direction
e	Charge of the electron
$\mathbf{E}$	Electric field
f	Frequency
f_i	Ion velocity distribution function
f_e	Electron velocity distribution function
i	$\sqrt{-1}$
I_e	Electron probe current
I_{eo}	Electron probe saturation current
I_n	Modified Bessel function of the first kind of order n
j_R	Current density for the rest ions
j_B	Current density for the beam ions
$\mathbf{k}$	Wave vector; $(k_r + ik_i)$
k_r	Real part of $\mathbf{k}$
k_i	Imaginary part of $\mathbf{k}$
$k_\parallel$	Component of $\mathbf{k}$ parallel to the magnetic field direction
$k_\perp$	Component of $\mathbf{k}$ perpendicular to the magnetic field direction
m_e	Electron mass
m_i	Ion mass
n_e	Electron density
n_B	Beam ion density
n_R	Rest ion density
n_N	Background neutral density
N_o	Plasma density $(n_B + n_R)$
p_o	Neutral gas pressure
$\mathbf{r}$	Position vector

r_p	Probe radius
t	Time co-ordinate
T_e	Electron temperature
T_{ib}	Beam ion temperature
T_{io}	Background ion temperature
$\mathbf{V}$	Velocity vector
V_o	Ion beam velocity
V_p	Plasma potential
V_ϕ	Wave phase velocity
W_o	Beam energy
Z	Plasma dispersion function

Greek Symbols

α	Ratio of beam to total ion density
γ	imaginary part of ω
Γ_n	$e^{-b}I_n(b)$
ϵ	Ratio of elastic to inelastic collision frequencies
ε	Energy density
ε_L	Longitudinal dielectric constant
θ	Angle between $\mathbf{B}$ and $\mathbf{z}$
θ_k	Angle between ion beam direction and $\mathbf{k}$
ϕ	Scalar potential
λ_{ce}	Elastic ion-neutral collision mean free path
λ_{ci}	Inelastic ion-neutral collision mean free path
λ_D	Electron Debye length
ν_i	Inelastic ion-neutral collision frequency
ν_e	Elastic ion-neutral collision frequency
ν_{en}	Electron-neutral collision frequency
ρ_e	Electron Larmour radius
σ	Collision cross section
λ	Wave length
ω	Wave angular frequency vector
$\overline{\omega}$	$\omega - \mathbf{k} \cdot \mathbf{V_o}$
ω_{ce}	Electron cyclotron frequency
ω_{LH}	Lower Hybrid frequency
ω_{pe}	Electron plasma frequency
ω_{pi}	Electron plasma frequency

Chapter 1

INTRODUCTION

Electrostatic instabilities ($\tilde{\mathbf{E}} = -\nabla\tilde{\phi}$ is parallel to $\mathbf{k}$) are excited when a current is drawn through a (magnetized) plasma. One such instability is the cross-field ion acoustic instability. It is driven unstable when the free energy available from an ion beam is fed into the wave whose amplitude then grows exponentially. This instability has been observed in ion beam experiments, collisionless shocks and toroidal heating devices. It also occurs naturally and has been detected by satellite measurements in the magneto sphere.

1.1 Cross-Field Electrostatic Instabilities

All plasma instabilities can be classed as either reactive or dissipative instabilities [30,39,48]. In a dissipative instability, coupling occurs between a wave and resonant plasma particles. If power flows from a negative energy wave to the particles, the wave will grow and if it is a positive energy wave, it will damp.

The energy density for linear electrostatic waves is given by:

$$\varepsilon = \frac{1}{4}\varepsilon_o \mid E \mid^2 \frac{\partial}{\partial\omega}\{\omega\,\varepsilon_L(\omega,k)\}_{\varepsilon_L=0}$$

where ε_L is the longitudinal dielectic constant. A negative energy wave is defined as a wave that has a negative energy density: $\varepsilon < 0$. It has

been shown by Lashmore-Davies [38] that the slow mode of a particle beam ($\omega/k < V_o$) is a negative energy wave. In a reactive instability two waves of unlike energy couple and energy is exchanged between the two waves and not with the plasma. When negative and positive energy waves couple, both will grow.

The dispersion relation for cross-field electrostatic instabilities in an infinite homogeneous collisionless plasma is [33,38]

$$1 + k^2\lambda_D{}^2 - \frac{T_e}{2T_i} Z'\left(\frac{\omega - kV_o}{kc_i}\right) + \frac{\omega}{k_\parallel c_e} \sum_{n=-\infty}^{\infty} e^{-b} I_n(b) Z\left(\frac{\omega - n\omega_{ce}}{k_\parallel c_e}\right) = 0 \qquad (1.1)$$

where V_o is the velocity of the ions, $b = \frac{1}{2}(k_\perp \rho_e)^2$, $c_{e,i}$ the electron and ion thermal velocities, λ_D the electron Debye length and ω_{ce} the electron gyrofrequency. Cross-field electrostatic instabilities can be divided into three broad categories:

1.1.1 Cross-field ion acoustic instability

The dispersion relation 1.1 can be simplified for the cross-field ion acoustic instability (CFIAI) to [31]

$$\omega/k = V_o - \frac{C_s}{\sqrt{1 + k^2\lambda_D^2}}$$

where C_s is the ion sound speed, λ_D the electron Debye length and V_o the drift velocity of the ions relative to the electron population. Being a negative energy wave, the cross-field ion acoustic wave will grow if $V_o > C_s$ [38]. The wave is of the dissipative type, that is, the wave couples with a small fraction of resonant ions and electrons in the plasma. A further condition for growth is $T_e > T_i$ as this avoids ion Landau damping. For $\rho_e > \lambda_\perp$ (where ρ_e is the electron Larmour radius and $\lambda_\perp$ is the wavelength perpendicular to the magnetic field direction), the instability behaves as if there is no magnetic field present [24,25].

For $k_\perp \rho_e \leq 1$ the electrons are constrained to essentially one-dimensional motion, along $\mathbf{B}$, and this enhances the growth rate compared to the $B = 0$

case [3,5,38], due to inverse Landau damping;

$$\left.\frac{\partial f_e}{\partial v_\parallel}\right|_{v_\parallel=\omega/k_\parallel} \gg \left.\frac{\partial f_e}{\partial v_\perp}\right|_{v_\perp=\omega/k_\perp}.$$

For $k_\perp \rho_e \gg 1$ the behavior approximates that of the non-magnetic case [24,25]. The instability propagates almost perpendicular to the magnetic field, i.e.,

$$1 \gg k_\parallel/k_\perp > \sqrt{m_e/m_i}.$$

As this angle approaches 90° ($k_\parallel/k_\perp$ small) the wave changes from a dissipative to a reactive instability. There are two possibilities:

1.1.2 Modified two-stream instability

It can be shown from equation 1.1 that two waves, the lower hybrid mode,

$$\omega_{LH} \approx \omega_{pi}\sqrt{1+\omega_{pe}^2/\omega_{ce}^2},$$

and the Doppler-shifted electron mode,

$$\omega \approx k_\perp V_o - (k_\parallel/k_\perp)\sqrt{m_i/m_e}\,\omega_{LH},$$

couple to produce the modified two-stream instability (MTSI) [39], with $\omega_{pi,e}$ the ion and electron plasma frequencies and ω_{ce} the electron cyclotron frequency. For $\omega_{pe} < \omega_{ce}$ this electron mode is just the Doppler-shifted electron plasma wave almost perpendicular to $\mathbf{B_o}$:

$$\omega \approx k_\perp V_o - (k_\parallel/k_\perp)\omega_{pe}$$

As $\omega/k < V_o$ the Doppler-shifted electron mode is a negative wave and the lower hybrid mode is a positive energy wave which couples to produce a reactive instability - the modified two-steam instability; occurring at

$$k_\parallel/k_\perp \approx \sqrt{m_e/m_i}.$$

As $k_\parallel/k_\perp$ is increased above this value the instability changes to the ion-acoustic instability. If $k_\parallel/k_\perp$ is reduced from this value, the instability goes over into another reactive instability, the electron drift instability.

1.1.3 Electron cyclotron drift instability

The electron cyclotron drift instability (ECDI) is also known as the beam cyclotron instability. It is produced by the coupling of the ion acoustic wave (positive energy wave) and a slow Doppler-shifted electron cyclotron wave (negative energy wave) [50,26]. The maximum growth rate occurs when the instability propagates exactly perpendicular to the magnetic field; $k_{\|}/k_{\perp} = 0$ and $k_{\perp}\rho_e \gg 1$. From equation 1.1 it can be shown that [39]

$$\gamma/\omega_{ce} = \frac{\sqrt{\mathrm{n}}}{(8\pi)^{1/4}}(\frac{m_e}{m_i})^{1/4}(1 + k^2\lambda_D^2)^{-3/4}$$

and the frequency is

$$\omega = k_{\perp}V_o - \mid \mathrm{n} \mid \omega_{ce},$$

where n is the summation index given in equation 1.1. The growth rate is proportional to $\sqrt{\mid \mathrm{n} \mid}$. As V_o increases more harmonics can grow, and the maximum growth rate occurs at higher values of $\mid \mathrm{n} \mid$. For a given value of n the growth rate is only weakly dependent on V_o/C_e and for $V_o/C_e \ll 1$ the instability only exists for $k_{\|}/k_{\perp} \approx 0$. If $k_{\|}/k_{\perp}$ is sufficiently large the slow electron cyclotron wave will be Landau damped and the instability will change to a dissipative cross-field ion acoustic wave.

The main features of the electrostatic instabilities are summarized in Table 1.

Instability	$\bar{\omega}$	k	Value of $(k_{\|}/k_{\perp})$ for maximum growth rate	Type of Instability
CFIAI	kC_s	$1 \leq k\rho_e < k_D$	V_o/C_e	Dissipative
MTSI	ω_{LH}	$0 \leq k\rho_e \leq 1$	$\sqrt{m_e/m_i}$	Reactive
ECDI	ω_{ce}	$1 \leq k\rho_e < k_D$	0	Reactive

Table 1.1: Summary of some characteristics of the electrostatic instabilities. Where CFIAI, MTSI and ECDI refer to the cross-field ion acoustic instability, modified two-stream instability and the electron cyclotron drift instability, respectively.

1.2 Review of the Cross-Field Ion Acoustic Instability.

1.2.1 Theoretical investigations

AREVEF [3] derives the linear dispersion relation using the Vlasov equation, assuming $T_e \gg T_i$ and $(k_\perp \rho_e)^2 \ll 1$. It is shown that with $k_\parallel/k_\perp \approx \sqrt{m_e/m_i}$ the instability is restricted to drift speeds V_o such that: $1 < V_o/C_s < 2$.

LASHMORE-DAVIES and MARTIN [39] present a detailed linear study of electrostatic instabilities driven by an $\mathbf{E} \times \mathbf{B}$ drift. They find that the magnetic field increases the normalized growth rate, γ/ω_{ce} for $k_\perp \rho_e \leq 1$. For $k_\perp \rho_e \geq 4$ the behaviour approximates that of the magnetic field free case. For $T_e = T_i$ the modified two-stream instability (characterized by $k_\parallel/k_\perp \approx \sqrt{m_e/m_i}$) changes into the cross-field ion acoustic instability as $k_\parallel/k_\perp$ increases above $\sqrt{m_e/m_i}$.

GARY and SANDERSON [26] derive a linear dispersion relation for electrostatic waves in a vlasov plasma of unmagnetized ions and magnetized electrons undergoing both $\mathbf{E} \times \mathbf{B}$ and $\nabla \mathbf{B}$ drifts. Attention is paid to oblique propagation and wavelengths larger than ρ_e. The maximum growth rate of the cross field ion acoustic instability is shown to be larger than that of the ion acoustic instability. A summary of the main properties of the electrostatic instabilities is presented.

GARY [24] extends the work of GARY and SANDERSON [26] with $T_e/T_i = 10$ and considers oblique and perpendicular propagation of ion-acoustic waves in a perpendicular shock. He concludes that the growth rate decreases rapidly as $k_\parallel/k_\perp$ increases and the growth rate approximates that of the unmagnetized case for propagation within a few degrees of perpendicular.

GARY [25] continues by examining the case for $T_e \approx T_i$. He finds that the growth rate is smaller than that for $T_e \gg T_i$ due to ion Landau damping.

PRIEST and SANDERSON [44] show that a temperature gradient increases the growth rate dramatically in a perpendicular shock . Both density and magnetic field gradients produce small effects.

CAVALIERE *et al.* [15] investigates a model of ion acoustic waves in a weakly ionized, bounded plasma. They find that the waves are strongly absorbed at the plasma boundary if a space-charge sheath exists at the wall.

ALAN and SANDERSON [2] investigate cross field ion-acoustic waves in a plasma with an electron temperature gradient. It is shown that the gradient drift is a more effective destabilising agent than the beam drift.

BHARUTHRAM and HELLBERG [8] numerically investigate drifts in the beam direction caused by small gradients: $\nabla \mathbf{B}$, $\nabla \mathbf{N}$ and ∇T_e. The temperature drift has a destabilising effect for $k_\perp \rho_e \geq 1$ but stabilizes the instability for $k_\perp \rho_e \leq 1$. The density gradient tends to stabilizes all cases. The maximum growth rate is also found to be parallel to the net drift.

BHARUTHRAM and HELLBERG [9] investigate the cross-field ion acoustic instability in the presence of a sheared magnetic field and a density gradient. The shear damping rate is found and the critical shear length is shown to vary as $(m_i/m_e)^{1/3}$ and as $((V_o - C_s)/C_s)^{-2/3}$.

BHARUTHRAM *et al.* [10] use the Bhatnager-Gross-Krook model to study the effects of charge transfer and elastic ion neutral collisions on the cross-field ion acoustic instability. The results are reported to be in reasonable agreement with experimental data.

1.2.2 Experimental studies

BISKAMP [12] investigates the dispersion relation for the ion acoustic waves that propagate in perpendicular shock wave geometry. The results are reported to be in qualitative agreement with satellite observation of the earth's bow shock [21].

BARRETT *et al.* [5] investigate the cross-field ion acoustic instability in two different plasma configurations – a streaming cesium-plasma device and a double plasma device. As measurements of k proved difficult, the dimensionless quantity $s = k_\perp/k_\parallel \sqrt{m_e/2m_i}$ is treated as a free parameter. $k_\parallel$ is assumed to be of order π/L where L is the plasma length parallel to the magnetic field direction. However this does not lead to good agreement be-

tween experiment and theory and the authors conjecture that the plasma appears infinitive due to sheath effects at the plasma boundaries.

HAYZEN and BARRETT [33] observed the cross-field ion acoustic instability in a double plasma device. The spatial growth rate was measured and good agreement with theory was obtained by taking the finite width of the plasma into account. Normalized $k_\perp \rho_e$ and magnetic field direction was varied.

HIROSE *et al.* [34] observed an electrostatic instability in a toroidal turbulent heating device, and interpreted it in terms of ion acoustic waves excited by a radial ∇T_e across a toroidal magnetic field. The observed anamalous electron thermal transport was explained by the ion acoustic instability.

GALLAGHER [23] analyzed satellite observations and found electric field emissions within the frequency range 150 Hz to 1 kHz in the dayside magneto sheath. Evidence strongly suggests the source to be ion acoustic wave generation upstream from the earths bow shock.

D'ANGELO [19] measured the ion beam attenuation in a double plasma device. This was mainly caused by charge-exchange collisions but at higher neutral pressure ion beam scattering took place due to ion acoustic turbulence.

1.3 Summary of the Thesis

This thesis deals with the dependence of the linear growth rate of the cross-field ion acoustic instability on various plasma parameters. The usual derivation of the dispersion relation is presented in Chapter 2 with elastic and inelastic ion-neutral collisions included. A numerical survey is also conducted using typical plasma parameters. In Chapter 3 the experimental apparatus is described and the methods of data analysis explained. The experimental observations are presented in Chapter 4. This begins with a section on the steady state properties of the plasma. Then growth rate measurements are presented for various values of different plasma parameters, and are compared with theory. Wave front measurements and the discrepancies between theory and experiment are discussed in the final part of this chapter. Chapter 5 concludes this thesis with a summary and suggests further extensions to this project.

Chapter 2

THEORY

In this chapter an extension to the theoretical model previously used by HAYZEN [31] is presented. The new model, derived by BHARUTHRAM [7,10], includes elastic and inelastic ion neutral collisions, which account for the experimentally observed stationary background ions. The software needed for the numerical survey was developed by the author in FORTRAN and run on a HP9000 computer.

This chapter contains four parts: In section 2.1 the derivation of the dispersion relation of the cross-field ion acoustic instability is presented; elastic and inelastic ion-neutral collisions are included. Special cases of the instability are examined in section 2.2 and a physical interpretation presented in section 2.3. Section 2.4 concludes this chapter with a computational survey of this model.

2.1 The Cross-Field Ion Acoustic Instability:

2.1.1 Basic assumptions:

We consider the case of an infinite homogeneous plasma consisting of an unmagnetized ion beam drifting through a background population of magnetized electrons at right angles to the magnetic field. Both the ion and electron velocity distributions are assumed to be maxwellian. Furthermore we shall make the following assumptions:

- The perturbed quantities in the wave vary as

$$e^{i(\mathbf{k}\cdot\mathbf{r}-\omega t)}.$$

- The growth rate γ (imaginary part of ω) satisfies the condition:

$$\omega_{ci} \ll \gamma \ll \omega_{ce},$$

where ω_{ci} and ω_{ce} respectively are the ion- and electron-cyclotron frequencies. This condition implies that for the time scale under consideration γ^{-1}, the electrons are considered to be magnetized, while the ions are not.

- The electric field of the wave is produced by charge separation. The electric field $\tilde{\mathbf{E}}$ can then be written as the negative gradient of the scalar potential $\tilde{\phi}$:

$$\tilde{\mathbf{E}} = -\nabla\tilde{\phi} = \mathbf{k}\tilde{\phi}.$$

Maxwell's equation

$$\nabla \times \tilde{\mathbf{E}} = -\frac{\partial \tilde{\mathbf{B}}}{\partial t}$$

implies that

$$\omega\tilde{\mathbf{B}}(= \mathbf{k} \times \tilde{\mathbf{E}}) = 0,$$

i.e., that the magnetic field is unperturbed ($\tilde{\mathbf{B}} = 0$) and the waves are longitudinal, with k parallel to $\tilde{\mathbf{E}}$.

- The wave model is non-relativistic, i.e., the phase velocity

$$V_\phi = \frac{w}{k} \ll c.$$

- The magnetic field and electron temperature are uniform, and the density gradients are negligible.

2.1.2 The collision term

We consider the Boltzmann equation:

$$\frac{\partial f_j}{\partial t} + \mathbf{V} \cdot \frac{\partial f_j}{\partial \mathbf{r}} + q(\mathbf{E} + \mathbf{V} \times \mathbf{B}) \cdot \frac{\partial f_j}{\partial \mathbf{V}} = (\frac{\partial f_j}{\partial t})_c$$

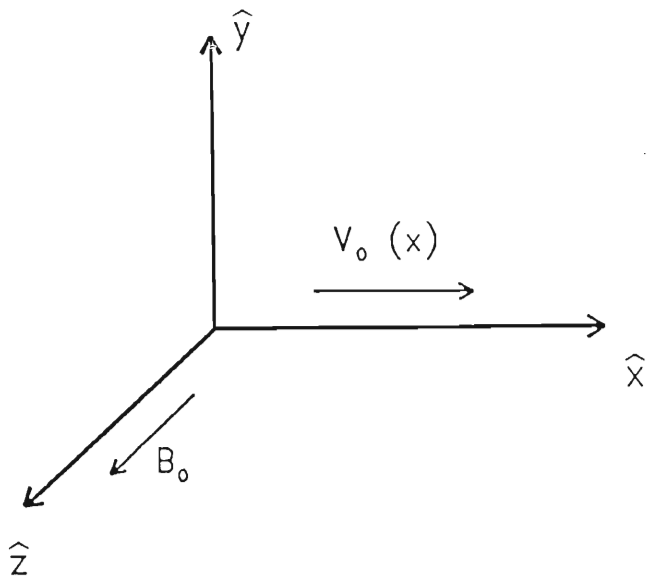

Figure 2.1: The wave propagates along the $\hat{x}$ direction with a velocity $V_o(x)$. An external magnetic field $B_o\hat{z}$ is present.

where $(\frac{\partial f_j}{\partial t})_c$ is the total collision term and the subscript j refers to the electron and ion species [37,18]. The Bhatnagar-Gross-Krook (BGK) [11,18] collision model is adopted. In this model an isotropic ion beam of density N_o moves from the source to the target plasma. When the beam enters the target region at $(x = 0)$ it has an initial drift velocity $V_o\hat{x}$. We consider a cartesian co-ordinate system in this region defined by $x \geq 0$; $-\infty \leq y \leq +\infty$; $-\infty \leq z \leq +\infty$. The electrons are at rest in the laboratory frame. The region is filled with neutral atoms of the same species as that of the ion beam. The neutral density is much greater than the beam density, $n_N \gg n_B$. There is a constant magnetic field $\mathbf{B} = (0,0,\mathbf{B}_o)$, but no external electric field is present. See Figure 2.1.

Using the BGK model, the Boltzmann equation for beam ions is:

$$\frac{\partial f_B}{\partial t} + \mathbf{V}\cdot\frac{\partial f_B}{\partial \mathbf{r}} + \frac{e}{m_i}(\mathbf{E} + \mathbf{V}\times\mathbf{B})\cdot\frac{\partial f_B}{\partial \mathbf{V}} = -\frac{\mathbf{V}}{\lambda_{\mathbf{ce}}}(f_B - f_{oB'}) - \frac{\mathbf{V}}{\lambda_{\mathbf{ci}}}(f_B) \quad (2.1)$$

where the terms on the right-hand side of the equation are the elastic and inelastic collision terms and $f_{oB'}$ is the stationary ion distribution function given in equation 2.5. Here λ_{ce} refers to the elastic and λ_{ci} to the inelastic mean free paths of the ions. The inelastic and elastic collision frequencies

can be written as

$$\nu_{i(e)} = \frac{\mathbf{V}}{\lambda_{ci(e)}}. \tag{2.2}$$

In general the mean free path λ is related to the collision cross section, σ and background neutral density, n_N according to

$$\lambda = (n_N \sigma)^{-1}. \tag{2.3}$$

Charge transfer collisions will cause the density n_N to change, but the condition $n_N \gg n_B$ means that the change in n_N is negligible. We shall assume that the collision cross-section σ is independent of velocity. This assumption is made on the basis of experimental measurements by BROWN *et al.* [14] which indicate a wide velocity range over which the collision cross-section varies little. The mean free path (equation 2.3) is therefore taken as constant and independent of velocity. The velocity dependence is however included in the definition of the collision frequencies (equation 2.2).

In using the BGK model we shall assume that the ion-collisions are the dominant type. Because of the very low percentage ionization of the argon gas, all Coulomb interactions have relatively low frequencies, and it can be shown that the electron-neutral collision frequency ν_{en} may be neglected. According to LEE [40]

$$\nu_{en} = \frac{15}{4} p_o a \sqrt{C_e} \left(\frac{C_e}{C_e^2 d + 1}\right)^{\frac{7}{2}}$$

where

$a = 3.74 \times 10^{-15} \mathrm{m}^{-4}\mathrm{s}^3\mathrm{torr}^{-1}$

$d = 3.48 \times 10^{-13} \mathrm{m}^{-2}\mathrm{s}^2$

C_e is the electron thermal velocity.

p_o is the neutral gas pressure in torr.

Using typical plasma parameters: $T_e = 2.4\mathrm{eV}$, $p_o = 3 \times 10^{-4}\mathrm{torr}$ the electron-neutral collision frequency is found to be: $\nu_e = 1.21 \times 10^6 \mathrm{s}^{-1}$. The electron mean free path is then:

$$\lambda_e = \frac{C_e}{\nu_e} = 0.8\mathrm{m}$$

As this distance is larger than the parallel dimension of the experimental device, the effect of electron-neutral collisions is neglected.

In dealing with the ion-neutral interactions, we shall distinguish between elastic and inelastic collisions. During elastic collisions of the beam ions with the stationary neutral atoms, the total kinetic energy stays constant and the internal states of the participating particles remain unchanged. During inelastic collisions the beam ions (with velocity $\mathbf{V}$) capture electrons from the stationary neutrals and thereby form a stationary background ion population and a neutral beam with a velocity slightly less than $\mathbf{V}$. The ions are stationary in the laboratory frame of reference and will be referred to as *rest* ions.

The elastic ion-neutral collisions cause the beam velocity to decrease with distance into the target plasma. Inelastic ion-neutral collisions result in the decrease of beam density and the increase of stationary background ions. Both these effects have been observed in the TP device (see Chapter 4). These effects have also been observed in the DP device by HAYZEN & BARRETT and by LEE [31,33,36,40].

2.1.3 The equilibrium beam ion distribution function

The Boltzmann equation 2.1 for the steady state can be written as

$$\mathbf{V} \cdot \frac{\partial f_B}{\partial \mathbf{r}} = -\frac{\mathbf{V}}{\lambda_{ci}} f_B - \frac{\mathbf{V}}{\lambda_{ce}} (f_B - f_{oB'}). \tag{2.4}$$

The background neutrals act as an infinite sink for the momentum and energy of the beam ions as they undergo elastic collisions. This is plausible as we have assumed $n_N \gg n_B$. The effect of elastic collisions will therefore be to change the beam distribution function to a stationary maxwellian distribution, given by:

$$f_{oB'}(\mathbf{r}, \mathbf{V}, t) = \frac{n_B(x)}{(\pi C_{io}^2)^{3/2}} exp(-\frac{V_x^2 + V_y^2 + V_z^2}{C_{io}^2}), \tag{2.5}$$

with $C_{io} = \sqrt{\frac{2T_{io}}{m_i}}$ the thermal speed of the non-drifting ions.

We will use perturbation theory to solve the Boltzmann equation above – equation 2.4. Introducing a perturbation parameter [7,10] $\epsilon = \frac{\nu_e}{\nu_i}$ the

equilibrium beam distribution function $F_{oB}(\mathbf{r},\mathbf{V})$ can be expanded:

$$F_{oB}(x,\mathbf{V}) = f_{oB}(x,\mathbf{V}) + \epsilon f_1(x,\mathbf{V}) + \epsilon^2 f_2(x,\mathbf{V}) + \cdots \tag{2.6}$$

where

$$f_{oB}(x,\mathbf{V}) = \frac{n_B(x)}{(\pi C_{iB}^2)^{\frac{3}{2}}} \exp(-\frac{(V_x - V_o)^2 + V_y^2 + V_z^2}{C_{iB}^2}) \tag{2.7}$$

and $C_{iB} = \sqrt{\frac{2T_{iB}}{m_i}}$. Substituting 2.6 into equation 2.4 :

$$\begin{aligned} V_x \frac{\partial(f_{oB} + \epsilon f_1 + \epsilon^2 f_2 + \cdots)}{\partial x} = & - \frac{\epsilon V}{\lambda_{ce}}((f_{oB} + \epsilon f_1 + \epsilon^2 f_2 + \cdots) - f_{oB'}) \\ & - \frac{V}{\lambda_{ci}}(f_{oB} + \epsilon f_1 + \epsilon^2 f_2 + \cdots). \end{aligned} \tag{2.8}$$

The first term on the right hand side has an additional factor ϵ, because it is assumed that inelastic collisions occur more frequently than elastic collisions,

$$\lambda_{ci} \ll \lambda_{ce}$$

i.e. the inelastic collision mean free path is much shorter than the elastic collision mean free path. To the lowest order in ϵ equation 2.8 only includes inelastic collision effects

$$V_x \cdot \frac{\partial f_{oB}}{\partial x} = -\frac{V}{\lambda_{ci}} f_{oB}. \tag{2.9}$$

If equation 2.7 is substituted in 2.9, $n_{oB}(0) = N_o$ and if we integrate using spherical co-ordinates in velocity space, we obtain

$$n_{oB}(x) = N_o \exp(\frac{-\alpha x}{\lambda_{ci}}) \tag{2.10}$$

where

$$\alpha = \frac{\frac{C_{iB}}{2\sqrt{\pi}V_o}\left(1 - \exp(-\frac{2V_o^2}{C_{iB}^2})\right) + \frac{1}{2}}{\frac{C_{iB}}{2\sqrt{\pi}V_o} + \frac{1}{2} - \frac{C_{iB}^2}{4V_o}\left(1 - \exp(-\frac{V_o^2}{C_{iB}^2})\left[1 - \mathrm{erf}(\frac{V_o}{C_{iB}})\right]\right)}. \tag{2.11}$$

In this calculation the spherical volume element is taken as

$$d\mathbf{V} = V^2 \sin\theta dV\ d\theta\ d\phi.$$

The integration over θ is carried out between the limits of 0 and $\pi/2$, because the beam ions have $V_x > 0$ in the region $x > 0$. The integration over velocity is between V_o and ∞ where V_o is the lower limit of V, because thermal motion will modify the ion beam drift velocity so that most ions will have a drift

speed greater than $V_o - C_{iB}$. This implies that $C_{iB} \ll V_o$. This assumption reduces equation 2.11 to

$$\alpha \simeq 1.$$

Equation 2.10 then reduces to

$$n_{oB}(x) = N_o e^{-x/\lambda_{ci}}. \tag{2.12}$$

Equation 2.12 can also be obtained by replacing V by V_y in equation 2.9. Because $C_{iB} \simeq C_{io}$ this result would generally hold for $V_o \gg C_i$. To first order in ϵ, both elastic and inelastic collision effects are included and 2.4 can then be written as

$$V_x \frac{\partial f_1}{\partial x} = -\frac{V}{\lambda_{ci}} f_1 - \frac{V}{\lambda_{ce}}(f_{oB} - f_{oB'}). \tag{2.13}$$

Using the boundary condition $f_1(0, \mathbf{v}) = 0$ this equation is integrated to obtain

$$\begin{aligned} f_1(x, \mathbf{v}) = & - \frac{x}{\lambda_{ce}} N_o e^{-x/\lambda_{ci}} \left[(\pi C_{iB}^2)^{-3/2} \exp\left(-\frac{(V_x - V_o)^2 + V_y^2 + V_z^2}{C_{iB}^2} \right) \right. \\ & \left. - (\pi C_{iB}^2)^{-3/2} \exp\left(-\frac{V_x^2 + V_y^2 + V_z^2}{C_{io}^2} \right) \right]. \end{aligned} \tag{2.14}$$

Using equations 2.5, 2.12 and 2.14

$$\begin{aligned} F_{oB}(x, \mathbf{v}) &= f_{oB}(x, \mathbf{v}) + f_1(x, \mathbf{v}) \\ &= n_{oB}(x)(1 - (x/\lambda_{ce}))(\pi C_{iB}^2)^{-3/2} \exp\left(-\frac{(V_x - V_o)^2 + V_y^2 + V_z^2}{C_{iB}^2} \right) \\ &\quad + n_{oB}(x)(x/\lambda_{ce})(\pi C_{iB}^2)^{-3/2} \exp\left(-\frac{V_x^2 + V_y^2 + V_z^2}{C_{io}^2} \right). \end{aligned} \tag{2.15}$$

Using this result the mean drift velocity $\overline{\mathbf{V}}(\mathbf{x})$ is given by

$$\begin{aligned} \overline{\mathbf{V}}(x) &= \frac{1}{n_{oB}(x)} \int \mathbf{V} F_{oB}(x, \mathbf{v})\, d\mathbf{V} \\ &= V_o(1 - x/\lambda_e)\hat{\mathbf{x}} \\ &= V_o \left(1 - (\frac{\lambda_{ci}}{\lambda_{ce}})(\frac{x}{\lambda_{ci}}) \right) \hat{\mathbf{x}}, \end{aligned} \tag{2.16}$$

but $\lambda_{ci}/\lambda_{ce} \ll 1$, therefore

$$\overline{\mathbf{V}} \simeq V_o \hat{\mathbf{x}} \simeq \text{constant}.$$

We will therefore disregard the spatial variation of the mean drift velocity, but not that of the ion beam density

$$n_{oB}(x) = N_o e^{-x/\lambda_{ci}}. \tag{2.17}$$

Experimental evidence of the ion beam attenuation is presented in section 4.1.

2.1.4 The equilibrium rest ion distribution function

The Boltzmann equation for the rest ions is:

$$\frac{\partial f_R}{\partial t} + \mathbf{V} \cdot \frac{\partial f_R}{\partial \mathbf{r}} + \frac{e}{m_i}(\mathbf{E} + \mathbf{V} \times \mathbf{B}) \cdot \frac{\partial f_R}{\partial \mathbf{V}} = -\frac{V}{\lambda_{ci}}(f_{oB'}). \tag{2.18}$$

For $V_o \gg C_i$, equations 2.5 and 2.17 show that the stationary beam distribution function is given by

$$f_{oB'}(x, \mathbf{V}) = N_o e^{-x/\lambda_{ci}} (\pi C_{io}^2)^{-3/2} exp(-\frac{V_x^2 + V_y^2 + V_z^2}{C_{io}^2}). \tag{2.19}$$

As mentioned before, the assumption $C_i \ll V_o$ allows us to set $V = V_x$ in equation 2.18 and thus obtain for the rest ions the steady state equation

$$V_x \frac{\partial F_{oR}}{\partial x} = (V/\lambda_{ci}) f_{oB'}. \tag{2.20}$$

After substituting for $f_{oB'}$, integrating with respect to x and using the condition $f_R(0, \mathbf{V}) = 0$, we find

$$F_{oR}(x, \mathbf{V}) = N_o(1 - e^{-x/\lambda_{ci}})(\pi C_{io}^2)^{-3/2} \exp(-\frac{\mathbf{V}^2}{C_{io}^2}). \tag{2.21}$$

The rest ion density is then given by

$$\begin{aligned} n_R(x) &= \int F_{oR}(x, \mathbf{V})\, d\mathbf{V} \\ &= N_o(1 - e^{-x/\lambda_{ci}}). \end{aligned} \tag{2.22}$$

From 2.12 and 2.22 it follows that

$$N_o = n_B(x) + n_R(x) \tag{2.23}$$

i.e., for every beam ion lost, a rest ion is created.

2.1.5 The dispersion relation for cross-field ion acoustic waves

Earlier analysis showed that in the absence of wave perturbations and assuming $C_i \ll V_o$, elastic and inelastic collisions modify the initial background distribution

$$F_{oB}(0,\mathbf{V}) = N_o(\pi C_{io}^2)^{-3/2}\exp(-\frac{(V_x-V_o)^2+V_y^2+V_z^2}{C_{io}^2}), \qquad (2.24)$$

to the following:

$$\begin{aligned} F_{oB}(x,\mathbf{V}) &= N_o e^{-x/\lambda_{ci}}(1-(x/\lambda_{ce}))(\pi C_{iB}^2)^{-3/2}\exp(-\frac{(V_x-V_o)^2+V_y^2+V_z^2}{C_{iB}^2}) \\ &\quad + N_o(x/\lambda_{ce})e^{-x/\lambda_{ci}}(\pi C_{iB}^2)^{-3/2}\exp(-\frac{V_x^2+V_y^2+V_z^2}{C_{io}^2}). \qquad (2.25) \end{aligned}$$

This equation is now taken to be the pseudo-equilibrium for the wave perturbations, i.e. it is taken to be the zero-order solution of the Boltzmann equation:

$$\frac{\partial f_B}{\partial t}+\mathbf{V}\cdot\frac{\partial f_B}{\partial \mathbf{r}}+\frac{e}{m_i}(\mathbf{E}+\mathbf{V}\times\mathbf{B})\cdot\frac{\partial f_B}{\partial \mathbf{V}} = -\frac{V_x}{\lambda_{ce}}(f_B-f_{oB'})-\frac{V_x}{\lambda_{ci}}(f_B) \quad (2.26)$$

Therefore, we can write

$$\begin{aligned} f_B(\mathbf{r},\mathbf{V},t) &= f_{oB}(x,\mathbf{V})+f_{1B}(\mathbf{r},\mathbf{V},t) \\ \mathbf{E}(\mathbf{r},t) &= \mathbf{E_1}(\mathbf{r},t) \\ \mathbf{B_1}(\mathbf{r},t) &= \mathbf{0} \qquad (2.27) \end{aligned}$$

with f_{1B} and $\mathbf{E_1}$ the perturbations due to the waves.

A similar argument holds for the rest ion distribution,

$$f_{oR}(x,\mathbf{V}) = N_o(1-e^{-x/\lambda_{ci}})(\pi C_{io}^2)^{-3/2}\exp(-\frac{V_x^2+V_y^2+V_z^2}{C_{io}^2}). \qquad (2.28)$$

This is taken to be the pseudo-equilibrium for wave perturbations, because it is the zero order solution of the rest ion Boltzmann equation,

$$\frac{\partial f_R}{\partial t} + \mathbf{V} \cdot \frac{\partial f_R}{\partial \mathbf{r}} + \frac{e}{m_i}(\mathbf{E} + \mathbf{V} \times \mathbf{B}) \cdot \frac{\partial f_R}{\partial \mathbf{V}} = -\frac{V_x}{\lambda_{ci}} f_{oB'}. \tag{2.29}$$

In the absence of perturbations the distribution functions 2.25 and 2.28 maintain a constant total ion density:

$$N_o = n_B(x) + n_R(x).$$

In order for this equation to be satisfied in the presence of perturbations, equations 2.26 and 2.29 are modified as follows:

Equation 2.26 for the beam ions becomes

$$\frac{\partial f_B}{\partial t} + \mathbf{V} \cdot \frac{\partial f_B}{\partial \mathbf{r}} + \frac{e}{m_i}(\mathbf{E} + \mathbf{V} \times \mathbf{B}) \cdot \frac{\partial f_B}{\partial \mathbf{V}} = -\nu_e(f_B - \frac{n_B(\mathbf{r},t)}{n_{oB}(x)} f_{oB'}) - \nu_i f_B \tag{2.30}$$

with $n_{oB}(x) = N_o \exp(-x/\lambda_{ci})$ and using 2.27 :

$$\begin{aligned} n_B(\mathbf{r},t) &= \int f_{oB}(x,\mathbf{V})\, d\mathbf{V} + \int f_{1B}(\mathbf{r},\mathbf{V},t)\, d\mathbf{V} \\ &= n_{oB}(x) + n_{1B}(\mathbf{r},t) \end{aligned} \tag{2.31}$$

where n_{1B} is the ion beam density perturbation and ν_e and ν_i are the elastic and inelastic collision frequencies.

Also the Boltzmann equation for the rest ions becomes

$$\frac{\partial f_R}{\partial t} + \mathbf{V} \cdot \frac{\partial f_R}{\partial \mathbf{r}} + \frac{e}{m_i}(\mathbf{E} + \mathbf{V} \times \mathbf{B}) \cdot \frac{\partial f_R}{\partial \mathbf{V}} = -\nu_i \frac{n_B(\mathbf{r},t)}{n_{oB}(x)} f_{oB'}. \tag{2.32}$$

With these modified equations, the local total ion density is conserved. This can be verified by adding 2.30 and 2.32 and integrating over velocity space.

The background ion density

If we now linearize 2.30 about the expression for pseudo equilibrium equation 2.25, we obtain:

$$\frac{\partial f_{1B}}{\partial t} + \mathbf{V} \cdot \frac{\partial f_{1B}}{\partial \mathbf{r}} - \frac{e}{m_i} \nabla\phi \cdot \frac{\partial f_{oB}}{\partial \mathbf{V}} = -V_x/\lambda_{ce}(f_{1B} - \frac{n_{1B}}{n_{oB}} f_{oB'}) - V_x/\lambda_{ci} f_{1B} \tag{2.33}$$

with $\mathbf{E_1} = -\nabla\phi_1$. We assume the perturbed quantities to be harmonic in space and time:

$$\begin{aligned} \phi_1(\mathbf{r},t) &= \sum_k \phi_{k\omega} e^{i(\mathbf{k}\cdot\mathbf{r}-\omega t)} \\ f_{1B}(\mathbf{r},\mathbf{V},t) &= \sum_k f_{Bk\omega}(\mathbf{V}) e^{i(\mathbf{k}\cdot\mathbf{r}-\omega t)} \\ n_{1B}(\mathbf{r},t) &= \sum_k n_{Bk\omega} e^{i(\mathbf{k}\cdot\mathbf{r}-\omega t)} \end{aligned} \tag{2.34}$$

From this we can derive the following [7,10]:

$$n_{Bk\omega} = \frac{\frac{e\phi_{k\omega}}{m_i} n_{oB}(x) \frac{k}{k'} \left[\frac{1-(x/\lambda_{ce})}{C_{iB}^2} Z'(\theta) + \frac{(x/\lambda_{ce})}{C_{io}^2} Z'(\theta') \right]}{1 - \frac{i}{2k'\lambda_{ce}} Z'(\theta')}, \tag{2.35}$$

with

$$\theta = \frac{\omega - k'V_o}{k'C_{iB}},\ \theta' = \frac{\omega}{k'C_{io}},\ k' = k - i(1/\lambda_{ce} + 1/\lambda_{ci})$$

where Z' is the derivative of the plasma dispersion function [22,18]

$$Z'(\varsigma) = -2[1 + \varsigma Z(\varsigma)]$$

in which ς is a complex number.

The rest ion density

A similar argument holds for the rest ions whose density is given by

$$\begin{aligned} n_{Rkw} &= \frac{e\phi_{k\omega}}{m_i} \frac{n_{oR}(x)}{C_{io}^2} Z'(\theta'') + \frac{i n_{Bk\omega}}{2k\lambda_{ci}} Z'(\theta'') \\ &= \frac{e\phi_{k\omega}}{m_i} Z'(\theta'') \left[\frac{n_{oR}(x)}{C_{io}^2} + \frac{i}{2k\lambda_{ci}} n_{oB}(x) \frac{k}{k'} \frac{\left[\frac{1-(x/\lambda_{ce})}{C_{iB}^2} Z'(\theta) + \frac{(x/\lambda_{ce})}{C_{io}^2} Z'(\theta') \right]}{\left(1 - \frac{i}{2k'\lambda_{ce}} Z'(\theta')\right)} \right] \end{aligned} \tag{2.36}$$

with $\theta'' = \omega/kC_{io}$.

The electron density

The distribution function of the stationary background electron population is assumed to be Maxwellian and is given by:

$$f_{oe}(\mathbf{V}) = N_o(m_e/2\pi T_e)^{3/2} e^{-mV^2/2T_e}.$$

The density can then be derived as:

$$n_{ek\omega} = \frac{e\phi_{k\omega}}{m_e}\frac{2N_o}{C_e^2}\left[1+\Gamma_o(b)(\frac{\omega}{k_\parallel C_e})Z(\frac{\omega}{k_\parallel C_e})\right] \tag{2.37}$$

in which the electron thermal speed $C_e = \sqrt{2T_e/m_e}$, $\Gamma_o(b) = e^{-b}I_o(b)$ and $I_o(b)$ is the modified Bessel function of order zero, with $b = k_\perp^2\rho_e^2$.

The solution of the dispersion relation

Using equations (2.35), (2.36) and (2.37), Poisson's equation can be written as

$$\phi_{k\omega} = \frac{4\pi e}{k^2}(n_{Bk\omega} + n_{Rk\omega} - n_{ek\omega}).$$

After substituting the relevant formula, this becomes:

$$\begin{aligned} 0 = 1 \quad &+ \quad k^2\lambda_D^2 + C_s^2 e^{-x/\lambda_{ci}}\frac{k}{k'}\frac{\left[\frac{1-(x/\lambda_{ce})}{C_{iB}^2}Z'(\theta) + \frac{(x/\lambda_{ce})}{C_{io}^2}Z'(\theta')\right]}{\left(1-\frac{i}{2k'\lambda_{ce}}Z'(\theta')\right)} \\ &- \quad Z'(\theta'')\left\{\frac{T_e}{2T_{io}}(1-e^{-x/\lambda_{ci}}) + \frac{i}{2k\lambda_{ci}}\frac{k}{k'}\frac{\left[\frac{1-(x/\lambda_{ce})}{C_{iB}^2}Z'(\theta) + \frac{(x/\lambda_{ce})}{C_{io}^2}Z'(\theta')\right]}{\left(1-\frac{i}{2k'\lambda_{ce}}Z'(\theta')\right)}\right\} \\ &+ \quad \Gamma_o(b)(\frac{\omega}{k_\parallel C_e})Z(\frac{\omega}{k_\parallel C_e}) \end{aligned} \tag{2.38}$$

where the Debye length λ_D and ion sound speed C_s are respectively defined by

$$\begin{aligned} \lambda_D &= \sqrt{\frac{T_e}{4\pi N_o e}} \\ C_s &= \sqrt{\frac{eT_e}{m_i}}, \end{aligned}$$

with T_e in electron volt and where

$$\begin{aligned} \theta &= \frac{\omega - k'V_o}{k'C_{iB}} \\ \theta' &= \frac{\omega}{k'C_{io}} \\ \theta'' &= \frac{\omega}{kC_{io}} \\ k' &= k - i(1/\lambda_{ce} + 1/\lambda_{ci}). \end{aligned}$$

2.2 Special Cases of the Dispersion Relation

In order to solve the dispersion relation analytically for the ion acoustic case we make the following assumptions [7,10]:

a) The ions are cold, i.e. T_{ib} and T_{io} are $\ll T_e$. If we further assume $\omega/k_\parallel \leq C_e$, it follows that

$$\left|\frac{\omega}{k_\parallel C_e}\right| \ll 1.$$

We can therefore use the power series expansion of the Z-function [22,18]:

$$\begin{aligned} Z(\varsigma) &= i\sqrt{\pi}e^{-\varsigma^2} - 2\varsigma\left[1 - \frac{2\varsigma^2}{3} + \cdots\right] \\ &\simeq i\sqrt{\pi} \end{aligned}$$

for $|\varsigma| \ll 1$, where ς is complex.

b) For the cold ions we assume:

$$|\theta| = \left|\frac{\omega - k'V_o}{k'C_{iB}}\right| \gg 1$$

$$|\theta'| = \left|\frac{\omega}{k'C_{io}}\right| \gg 1$$

$$|\theta''| = \left|\frac{\omega}{kC_{io}}\right| \gg 1$$

The following expansion of the Z-function can then be used:

$$Z(\varsigma) \simeq -\varsigma^{-1}(1 + \frac{1}{2\varsigma^2})$$

which is appropriate for $|\varsigma| \gg 1$. Therefore for the first derivative of the Z-function:

$$\begin{aligned} Z'(\varsigma) &= -2\left[1 + \varsigma Z(\varsigma)\right] \\ &= \varsigma^{-2} \end{aligned}$$

c) We also assume $\lambda_{ce} \gg \lambda_{ci}$ and, consequently,

$$k\lambda_{ce} \gg k\lambda_{ci} \gg 1.$$

d) Lastly we assume that the ion beam speed is much larger than the ion sound speed:

$$V_o \gg C_s.$$

Applying these assumptions to equation 2.38 we find the following solution to the real part of the dispersion relation:

$$\frac{\omega_k^r}{k} = V_o \pm \sqrt{1-(x/\lambda_{ce})}\left(\sqrt{\frac{N_o e^{-x/\lambda_{ci}}}{N_o}}\right)\frac{C_s}{\sqrt{1+k^2\lambda_D^2}} \tag{2.39}$$

where we define a complex frequency $\omega_k = \omega_k^r + i\gamma_k$. Alternatively, using equation 2.12, we can rewrite equation 2.39 as

$$\frac{\omega_k^r}{k} = V_o \pm \sqrt{1-(x/\lambda_{ce})}\left(\sqrt{\frac{n_{oB}}{N_o}}\right)\frac{C_s}{\sqrt{1+k^2\lambda_D^2}}. \tag{2.40}$$

Note that there are two modes. The positive sign corresponds to the fast mode of the ion acoustic wave propagating with a phase speed slightly higher than the beam speed.The slow mode corresponds to the negative sign in the equation and it is this growing mode that is observed experimentally.

The solution for the imaginary part of the dispersion relation is

$$\gamma_k = \frac{-\frac{n_{oB}(x)[1-x/\lambda_{ce}]}{m_i(\omega_k^r-kV_o)^2}\left\{\left(\frac{\lambda_{ce}^{-1}+\lambda_{ci}^{-1}}{k}\right)\left[1+\frac{2kV_o}{(\omega_k^r-kV_o)}\right]-\frac{k^2C_{io}^2}{2(\omega_k^r)^2k\lambda_{ci}}\right\}-\frac{2N_o\sqrt{\pi}\Gamma_o\omega_k^r}{m_eC_e^3k^2k_\parallel}}{2\left[\frac{n_{oB}(x)}{m_i}\left\{(\omega_k^r-kV_o)^{-3}+\frac{x}{\lambda_{ce}}\left((\omega_k^r)^{-3}-(\omega_k^r-kV_o)^{-3}\right)\right\}+\frac{n_{oR}(x)}{m_i(\omega_k^r)^3}\right]} \tag{2.41}$$

2.2.1 The collisionless case

In the absence of collisions the elastic and inelastic mean free paths, λ_{ce} and λ_{ci}, will tend to infinity. Consequently,

$$\lim_{\lambda_{ci}\to\infty}(e^{-x/\lambda_{ci}}) = 1$$

$$\lim_{\lambda_{ci}\to\infty}(1-x/\lambda_{ci}) = 1$$

$$\lim_{\lambda_{ci(e)}\to\infty} k' = 1.$$

The ion densities then have the following limiting values:

$$\lim_{\lambda_{ci}\to\infty} n_{oB}(x) = \lim_{\lambda_{ci}\to\infty} N_o e^{-x/\lambda_{ci}} = N_o$$

$$\lim_{\lambda_{ci}\to\infty} n_{oR}(x) = \lim_{\lambda_{ci}\to\infty} N_o(1 - e^{-x/\lambda_{ci}}) = 0.$$

Without collisions the dispersion relation therefore reduces to:

$$0 = 1 + k^2\lambda_D^2 + C_s^2\left[\frac{1}{C_{iB}^2}Z'(\theta)\right] + \Gamma_o(b)\left(\frac{\omega}{k_\parallel C_e}\right)Z\left(\frac{\omega}{k_\parallel C_e}\right). \qquad (2.42)$$

Using the relationships

$$\frac{C_s^2}{C_{iB}^2} = \left(\frac{T_e}{m_i}\right) / \left(\frac{2T_{iB}}{m_i}\right) = \frac{T_e}{2T_{iB}}$$

and

$$\lim_{\lambda_{ci(e)}\to\infty} \theta = \frac{\omega - kV_o}{kC_{iB}},$$

equation 2.42 can be rewritten as

$$0 = 1 + k^2\lambda_D^2 + \frac{T_e}{2T_{iB}}Z'\left(\frac{\omega - kV_o}{kC_{iB}}\right) + \Gamma_o(b)\left(\frac{\omega}{k_\parallel C_e}\right)Z\left(\frac{\omega}{k_\parallel C_e}\right). \qquad (2.43)$$

Making the usual assumptions for ion acoustic waves, i.e., $T_e \gg T_{iB}$ and $(\omega - kV_o)/(kC_{iB}) \gg 1$, the solution for the real part of the dispersion relation becomes:

$$\frac{\omega_k^r}{k} = V_o \pm \frac{C_s}{\sqrt{1 + k^2\lambda_D^2}}. \qquad (2.44)$$

The growth rate of the slow beam mode is

$$\frac{\gamma_k}{\omega_k^r} = \sqrt{\frac{\pi m_e}{8m_i}}\frac{k}{k_\parallel}\frac{\Gamma_o(b)}{(1 + k^2\lambda_D^2)^{3/2}}. \qquad (2.45)$$

This form of the dispersion relation was derived by HAYZEN and BARRETT [31,33].

Comparing the approximate phase velocity derived by BHARUTHRAM [7] (equation 2.40) with that derived by HAYZEN (equation 2.44) it is found that the second term on the left hand side of the equation is different by a factor $\sqrt{1 - (x/\lambda_{ce})}\sqrt{\frac{n_{oB}}{N_o}}$. Typical experimental data show that $\lambda_{ce} \gg x$ and $k^2\lambda_D^2 \ll 1$. Equation 2.40 for the slow mode then reduces to

$$\frac{\omega_k^r}{k} = V_o - \sqrt{\frac{n_{oB}}{N_o}}C_s.$$

This implies that the phase velocity in the beam frame, $V_o - \omega_k^r/k$, is less than its collision-free value by a factor $\sqrt{n_{oB}/N_o}$. This has been observed experimentally; see Chapter 4.

2.2.2 The ion acoustic instability

In the absence of collisions, magnetic field and drift velocity equation 2.42 reduces to the dispersion relation for ordinary ion acoustic waves,

$$0 = 1 + k^2\lambda_D^2 + \frac{T_e}{2T_{iB}} Z'(\frac{\omega}{kC_{iB}}).$$

Making the following assumptions: $T_e \gg T_{iB}$ and $\omega/(kC_{iB}) \gg 1$ this equation reduces to

$$0 = 1 + k^2\lambda_D^2 + \frac{C_s^2}{C_{iB}^2}(\frac{kC_{iB}}{\omega})^2$$

or

$$\frac{\omega^2}{k^2} = \frac{C_s^2}{1 + k^2\lambda_D^2}, \tag{2.46}$$

which is the usual ion acoustic dispersion relation.

2.3 Physical Interpretation

The cross-field ion acoustic instability is a dissipative instability – it is driven by a group of resonant electrons. As discussed in section 1.1.1, this slow mode of the beam is a negative energy wave, i.e., if energy is fed from the wave to the resonant electrons the wave will grow. If the slope of the electron distribution function is negative at the phase velocity it follows that more resonant electrons are travelling just slower than just faster than the wave. Energy can therefore be fed from the wave to the electrons. This will lead to growth of the wave with the growth rate proportional to the slope of the distribution function [16].

From the assumption $T_e \gg T_{iB}$ we have $C_s \gg C_{iB}$. The wave travels at approximately $\omega/k = V_o - \sqrt{n_{oB}/N_o}\,C_s$ and it follows that the ion distribution function has a positive slope and the unmagnetised electron distribution function has a very small negative slope. This generally means that the

electron inverse Landau damping is overcome by the ion Landau damping. The wave will therefore be damped.

In the presence of a magnetic field the electrons are restricted to essentially one-dimensional motion along the magnetic field direction, the electron larmour radius

$$\rho_e = \frac{C_e}{\omega_{ce}},$$

being much smaller than typical wavelengths of the instability (where ω_{ce} is the electron cyclotron frequency). The electrons can therefore not neutralize differences in wave potential by travelling in the direction of wave propagation ($\overline{ON}$), but accomplish this by moving parallel to the magnetic field direction $\overline{OM}$; see Figure 2.3. The effect of the magnetic field is to modify the electron thermal velocity C_e by a factor

$$\sin\theta_k = \overline{ON}/\overline{OM} = k_\parallel/k,$$

i.e.

$$C_e' = (k_\parallel/k)C_e = (\sin\theta_k)C_e$$

where C_e' is the projection of the electron thermal velocity onto the direction of the wave propagation. The effect on the electron distribution function is to increase the negative gradient at the phase velocity as indicated by a and b in Figure 2.2. This increased negative gradient causes the electron inverse Landau damping to overshadow the ion Landau damping, giving a net growth effect. Restricting the electron motion to one dimension thus increases the growth rate of the instability.

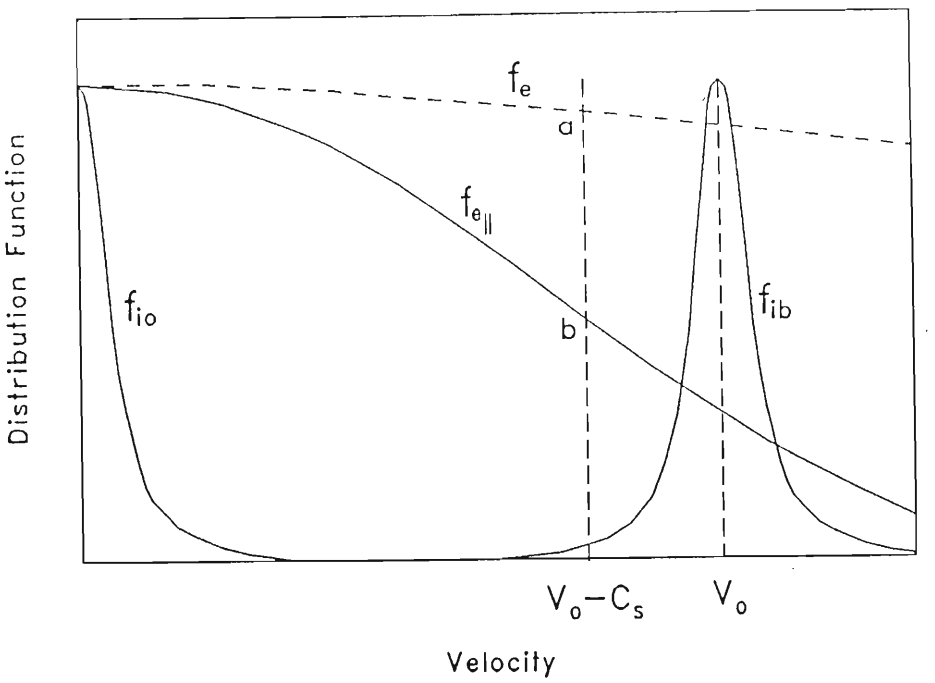

Figure 2.2: The rest and beam ion velocity distributions are indicated by f_{io} and f_{ib}. The dashed line corresponds to the distribution function for unmagnetized electrons. A magnetic field modifies the electron distribution to $f_{e\|}$ resulting in an increased slope at the phase velocity as labelled by *a* and *b*.

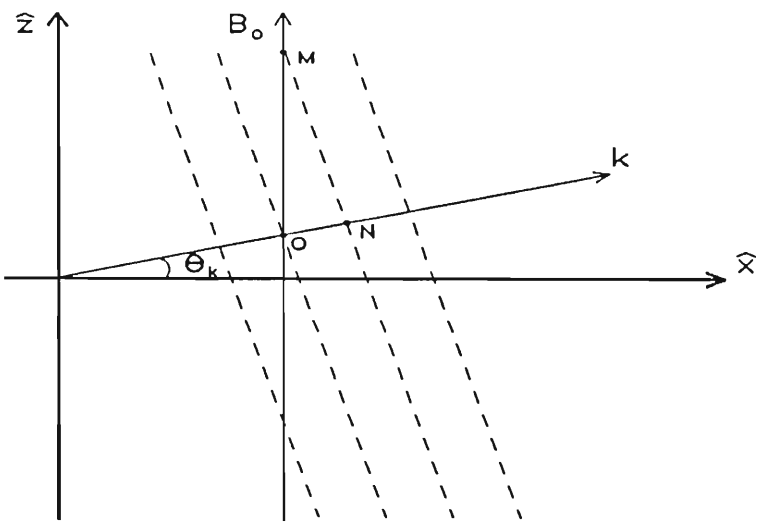

Figure 2.3: Restriction of electron movement parallel to the magnetic field

2.4 A Computational Survey of the Theoretical Model

In this section numerical solutions of the full dispersion relation 2.38 are presented. The following cases are examined:

- A comparison between spatial and temporal growth rates.
- The variation of growth rate with distance into the plasma.
- The effect of ion and electron temperature on the growth rate.
- The effect of electron density on the growth rate.
- The effect of beam velocity on the instability.
- The effect of the background ion temperature on the instability.
- The effect of the magnetic field on the growth rate.
- The effect of varying the angle θ_k between the beam and the direction of wave propagation.
- The effect of finite geometry on the growth rate.

2.4.1 A comparison between spatial and temporal growth rates.

The dispersion relation represents the relationship between ω and k. It can be solved either for complex frequency ($\omega = \omega_r + i\gamma$) and real wave number or for complex wave number ($k = k_r + ik_i$) and real frequency. The latter case is of more importance from an experimental point of view as a real frequency is injected into the plasma and a complex wave number is measured. This solution will therefore be used in the following discussions.

Figure 2.4 illustrates the difference between k_i/k_r and γ/ω_r, where growth rate is plotted against normalized wave number k. The parameter labelling the curves is V_o/C_s. From the diagram it is clear that the growth rates are approximately the same over a large range in k. There is a small difference in the region $0.2 \leq \frac{1}{\sqrt{2}}k\rho_e \leq 0.6$, which becomes larger as the beam velocity V_o

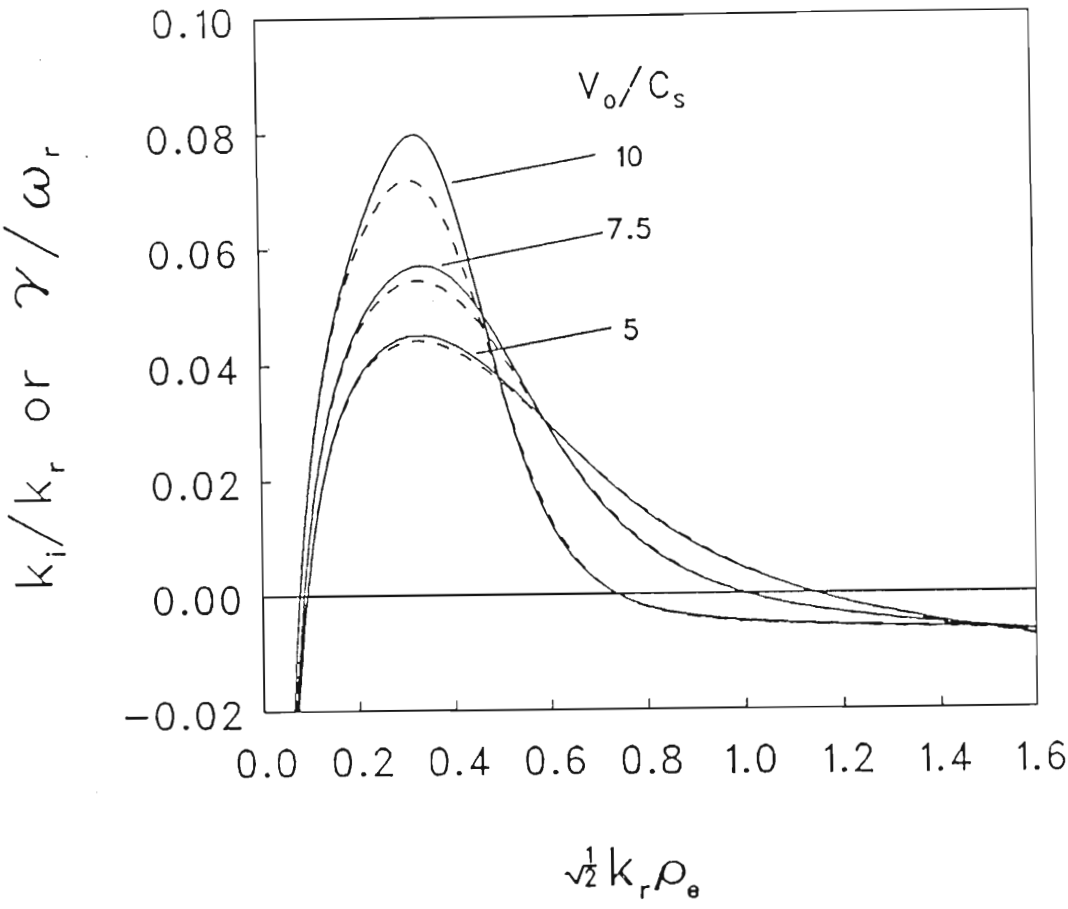

Figure 2.4: Temporal (solid line) and spatial (dashed line) growth rates are plotted against the normalized wave number for the following conditions: $T_e/T_{ib} = 48$, $T_e = 2.4$ eV, $B = 23$ gauss, $N_o = 1 \times 10^8$ cm^{-3}, $m_i/m_e = 73440$, $k_\parallel/k_\perp = 0.015$, $x = 35$ cm, $\lambda_{ce}/\lambda_{ci} = 100$, $\lambda_{ci} = 25$ cm, ($\lambda_{ce,i}$ being the mean free paths for elastic and inelastic ion neutral collisions). V_o/C_s is the parameter labeling the curves. The larger the beam velocity the larger the difference between temporal and spatial growth rates.

increases. The spatial and temporal growth rates of large amplitude plasma waves are related by Lee and Schmidt [41]:

$$\gamma = k_i \frac{\partial \omega}{\partial k}$$

It is assumed that this also applies to small amplitude waves. Furthermore if the approximate dispersion relation is used:

$$\frac{\omega}{k} = V_o - \sqrt{\alpha} C_s$$

with $\alpha = \frac{n_{oB}}{N_o}$, we find

$$\frac{\partial \omega}{\partial k} = \frac{\omega}{k}.$$

Therefore

$$\frac{\gamma}{\omega_r} \approx \frac{k_i}{k_r},$$

This is a reasonable approximation as illustrated by Figure 2.4.

In Figure 2.5 the normalized frequency (in the ion rest frame) is plotted against normalized wave number. The dashed line represents $|\bar{\omega}_r| / k = \sqrt{\alpha} C_s$. Wherever the gradient of the dispersion relation differs greatly from that of the curve for $\sqrt{\alpha}$ it follows that:

$$\frac{\partial \omega}{\partial k} > \frac{\omega}{k}$$

or

$$\frac{\partial \omega}{\partial k} < \frac{\omega}{k}.$$

The domains of wave number where these conditions apply are therefore also the domains over which the difference in temporal and spatial growth rates is maximum.

2.4.2 Variation of growth rate with distance into the plasma.

In Figure 2.6 the growth rate is represented as a function of x, distance into the target plasma. The distance is normalized with respect to the ion charge exchange mean free path, λ_{ci}. The curves show somewhat different behaviour for $V_o/C_s \geq 5$ and $V_o/C_s \leq 5$. If $V_o/C_s > 5$ the growth rate decreases monotonically with increasing x. The curves intersect, but not at a single point as was reported by BHARUTHRAM *et al.* [10]. Bharuthram

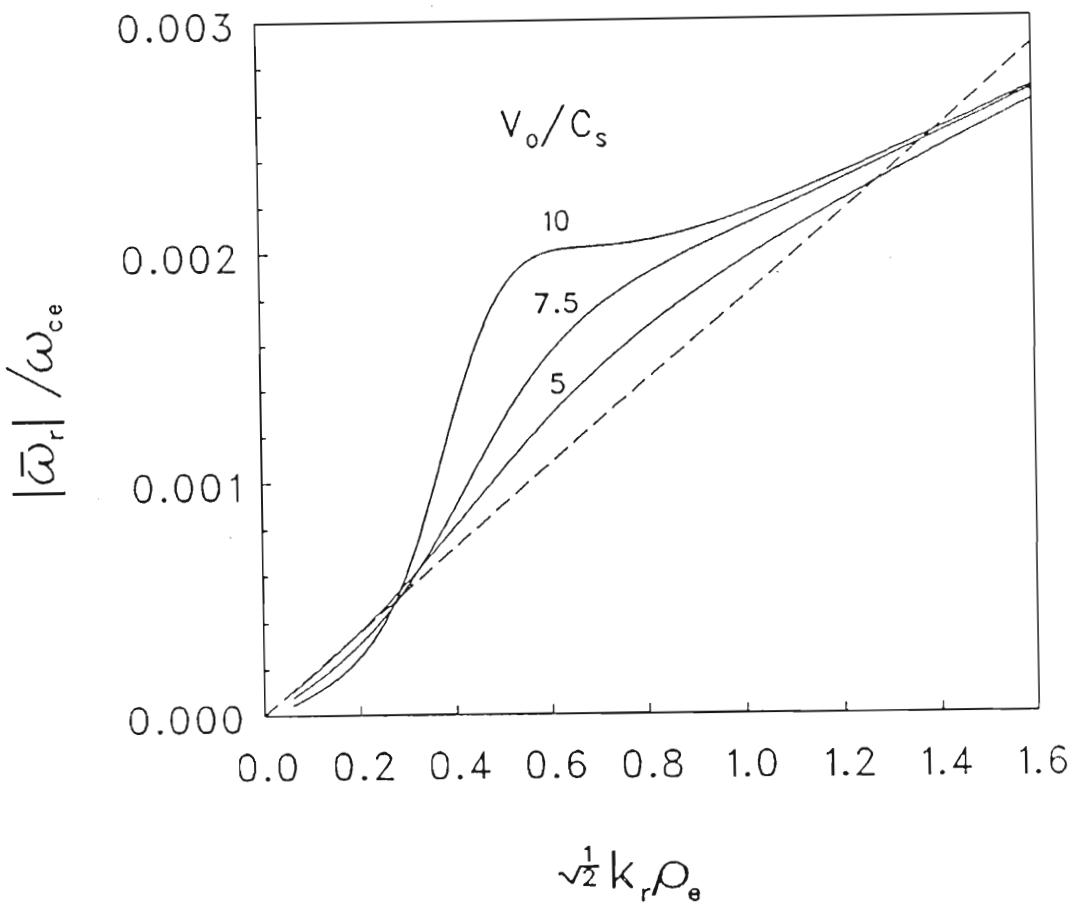

Figure 2.5: Normalized frequency in the ion rest frame is plotted against normalized wave number for the same conditions as in Figure 2.4: $T_e/T_{ib} = 48$, $T_e = 2.4$ eV, $B = 23$ gauss, $N_o = 1 \times 10^8$ cm^{-3}, $m_i/m_e = 73440$, $k_\parallel/k_\perp = 0.015$, $x = 35$ cm, $\lambda_{ce}/\lambda_{ci} = 100$, $\lambda_{ci} = 25$ cm. V_o/C_s is the parameter labelling the solid curves. The dashed line represents $\bar{\omega}/k = \alpha^{1/2} C_s$ in the ion rest frame.

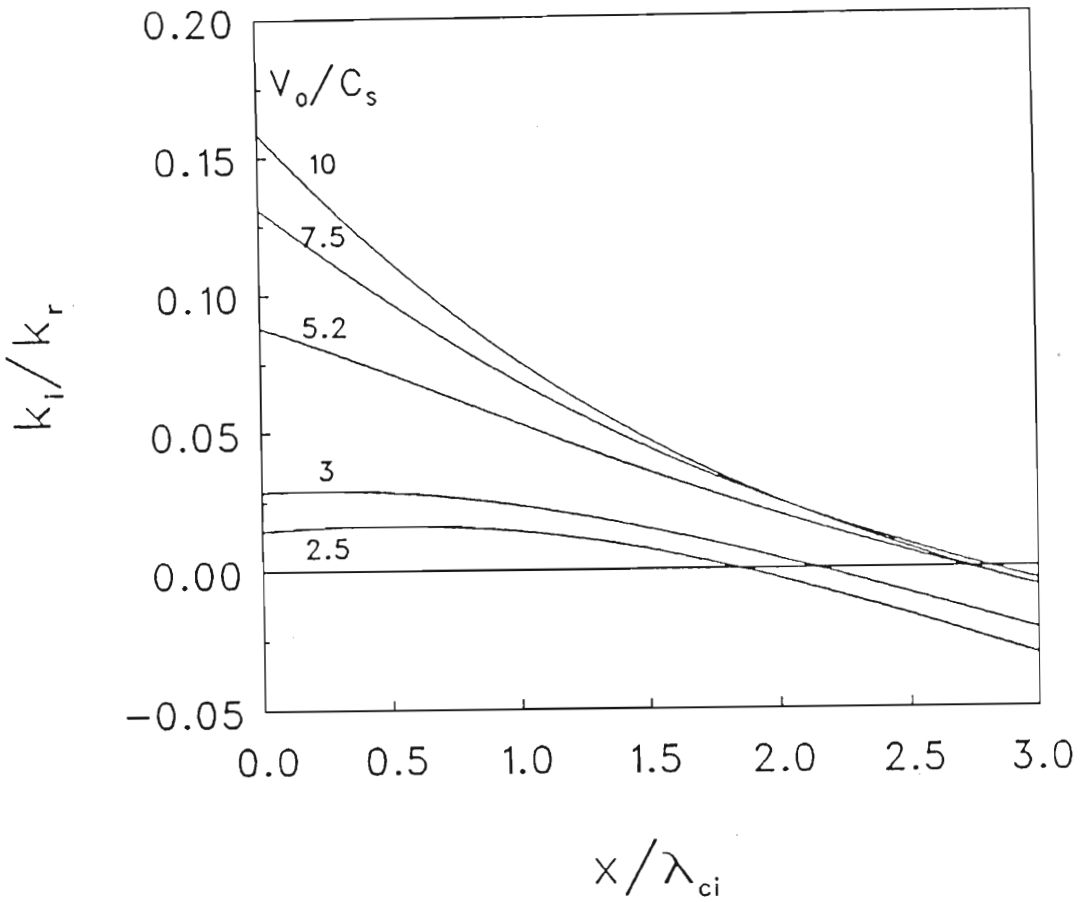

Figure 2.6: Growth rate as a function of normalized distance into the plasma for the conditions: $T_e/T_{ib} = 48$, $T_e = 2.4$ eV, $B = 23$ gauss, $N_o = 1 \times 10^8$ cm^{-3}, $m_i/m_e = 73440$, $k_\parallel/k_\perp = 0.015$, $\lambda_{ce}/\lambda_{ci} = 100$, $\lambda_{ci} = 25$ cm, $f = 350$ kHz. The parameter labeling the curves is V_o/C_s. As the beam velocity decreases the growth rate decreases for $x \leq 1.5\lambda_{ci}$.

used the approximate form of the dispersion relation 2.40 in which it is assumed that $V_o \gg C_s$; we find that their results are therefore not accurate if $V_o \geq C_s$.

For the condition $V_o < 5$, the growth rate is much smaller and shows a plateau before it starts to decrease at larger x. Furthermore, these low V_o curves do not intersect. This can be explained by inspection of the dispersion curves in Figure 2.7. These are obtained at $x = 10$ cm for different values of V_o/C_s. The dashed lines in this diagram represent the simplified dispersion relation for the ion acoustic instability: $\omega/k = V_o - \sqrt{n_{oB}/N_o}C_s$. At $V_o \gg C_s$ this approximation is good, but at $V_o > C_s$ there is a significant deviation from the ion acoustic approximation. In this region the ion acoustic instability becomes the ion-ion instability; (see section 2.5.5). The lower curves in figure 2.6 therefore correspond to the instability becoming the ion-ion instability.

As the mean free path for elastic ion neutral collisions is decreased (i.e. collision frequency is increased), the growth rate decreases. This effect is illustrated in Figure 2.8. The inelastic mean free path is held constant and the parameter labelling the curves is $\lambda_{ci}/\lambda_{ce}$. In the case of the $\lambda_{ci}/\lambda_{ce} = 0.5$ curve, for example, the instability becomes heavily damped at $x/\lambda_{ci} \approx 2$.

2.4.3 The effect of ion and electron temperature on the growth rate.

The growth rate is represented as a function of the parameter $b^{-1} = 1/2(k_r\rho_e)^{-2}$ in Figure 2.9. The parameter labelling the curves is T_e/T_i with T_i varying. As the ion temperature increases, the growth rate decreases (by ion Landau damping). In Figure 2.10 the parameter T_e/T_i again labels the curves, but now T_e is varying. In this case an increase in electron temperature also causes the growth rate to decrease. In this case an increase in electron temperature implies less inverse Landau damping; see Figure 2.2.

In Figure 2.9 where T_i is increased, the positive slope of the ion distribution function at the value of ω/k will also increase, because $\omega/k \approx V_o - C_s$ and $C_i \ll C_s$. With T_e remaining unchanged, the value of $\partial f_i/\partial v$ at the phase velocity becomes less negative and the inverse Landau damping therefore decreases – the overall growth rate decreases.

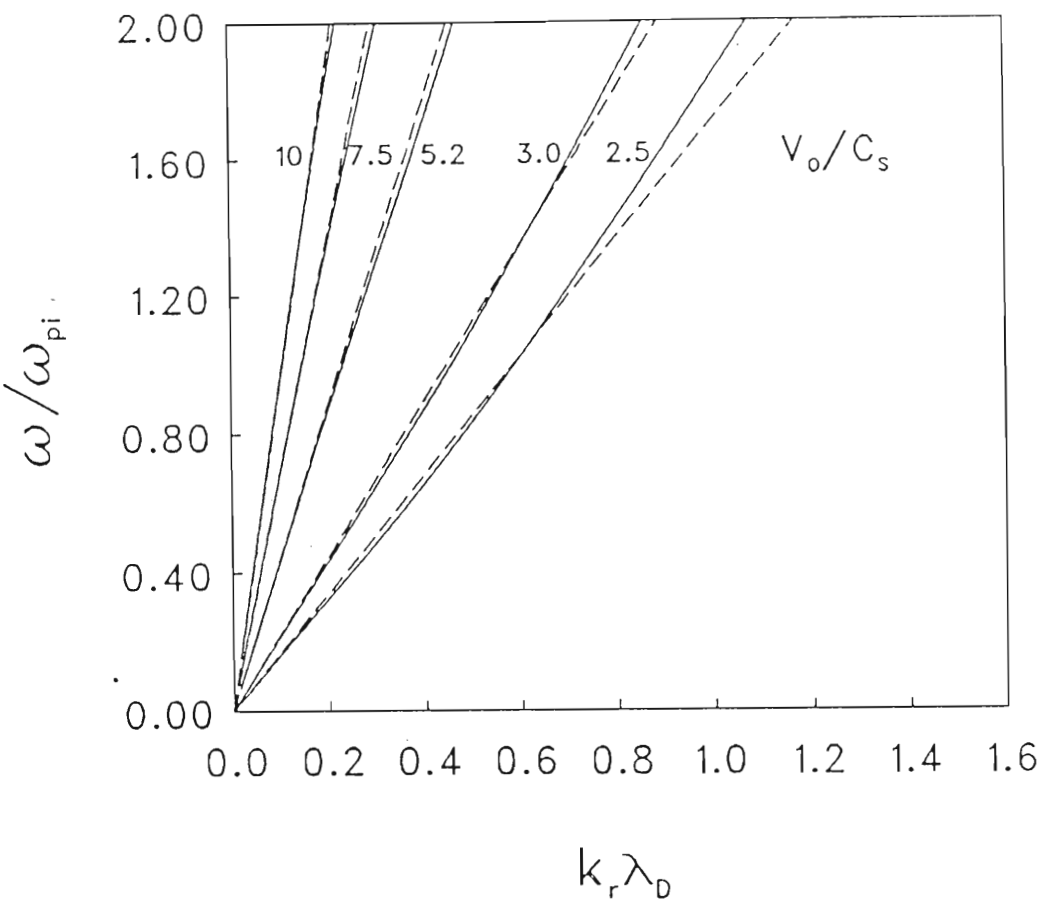

Figure 2.7: The dispersion relation at various beam velocities. The parameter labeling the curves is V_o/C_s. The full dispersion relation is used to calculate the solid curves and the dashed curves correspond to the simplified relation $\omega/k = V_o - \alpha^{1/2}C_s$. Where: $T_e/T_{ib} = 48$, $T_e = 2.4$ eV, $B = 23$ gauss $N_o = 1 \times 10^8$ cm^{-3}, $m_i/m_e = 73440$, $k_\parallel/k_\perp = 0.015$, $x = 10$ cm, $\lambda_{ce}/\lambda_{ci} = 100$, $\lambda_{ci} = 25$ cm. The discrepancy between the two dispersion relations becomes large at low values of V_o/C_s.

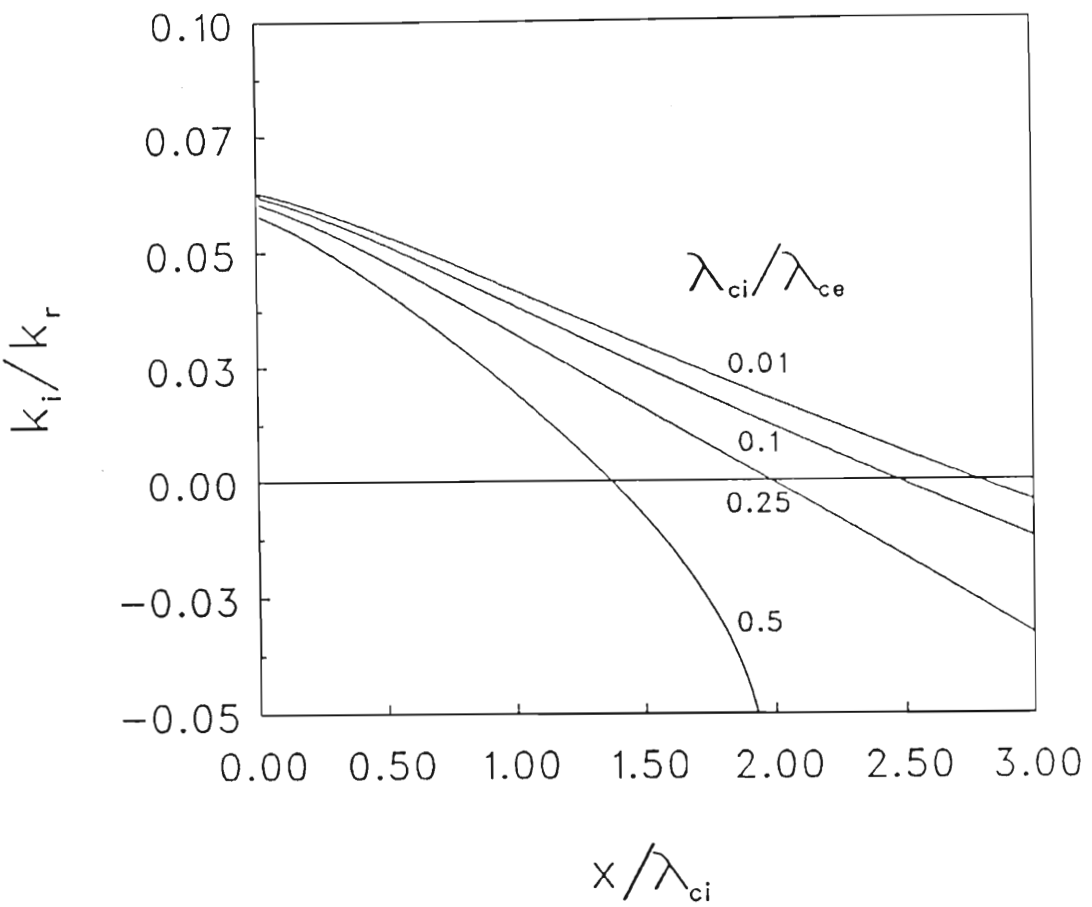

Figure 2.8: Growth rate as a function of normalized distance into the plasma at various values of ion neutral elastic collision mean free path. Where: $T_e/T_{ib} = 48$, $T_e = 2.4$ eV, $B = 23$ gauss, $W_o = 32$ eV, $V_o/C_s = 5.2$, $N_o = 1 \times 10^8$ cm^{-3}, $m_i/m_e = 73440$, $k_\parallel/k_\perp = 0.015$, $\lambda_{ci} = 25$ cm. The parameter labeling the curves is $\lambda_{ce}/\lambda_{ci}$.

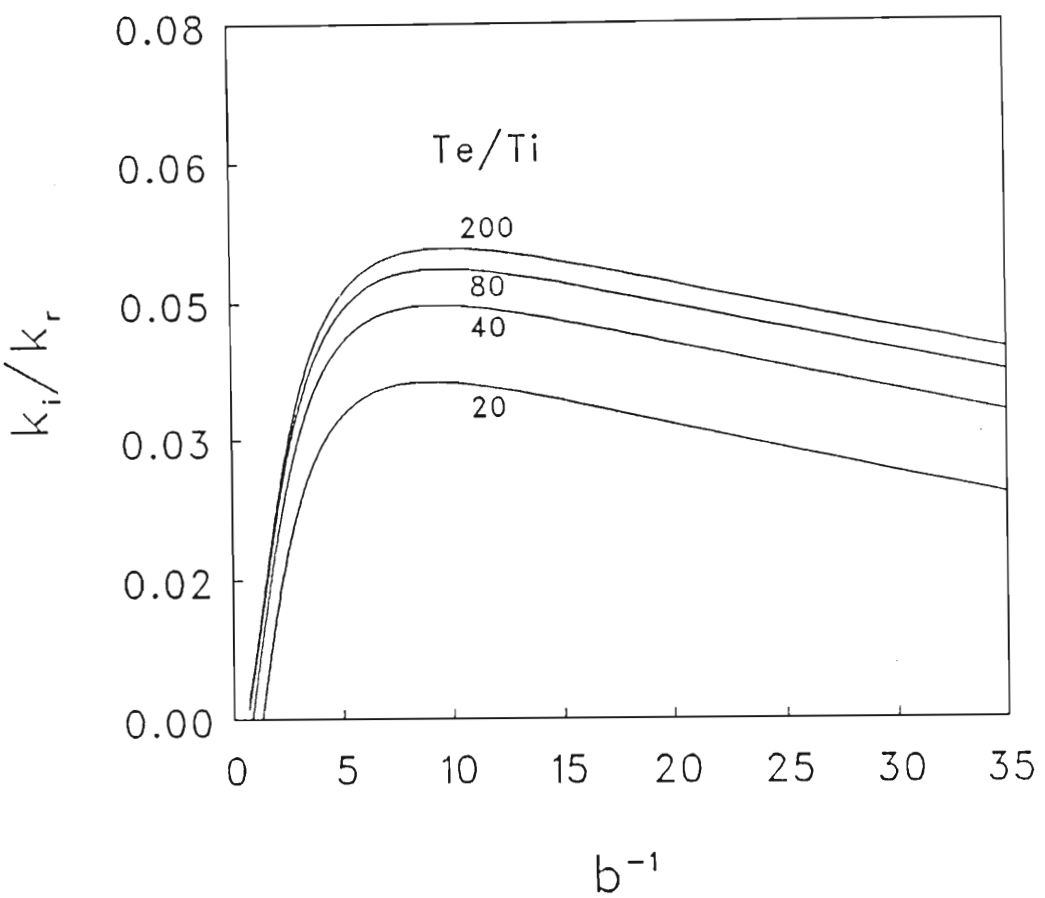

Figure 2.9: Growth rate as a function of the parameter $b^{-1} = 2(k\rho_e)^{-2}$ for the conditions: $B = 23$ gauss, $W_o = 32$ eV, $N_o = 1 \times 10^8$ cm^{-3}, $m_i/m_e = 73440$, $k_\parallel/k_\perp = 0.015$, $x = 35$ cm, $\lambda_{ce}/\lambda_{ci} = 100$, $\lambda_{ci} = 25$ cm. The parameter labeling the curves is T_e/T_i with T_e fixed at 2.0 eV.

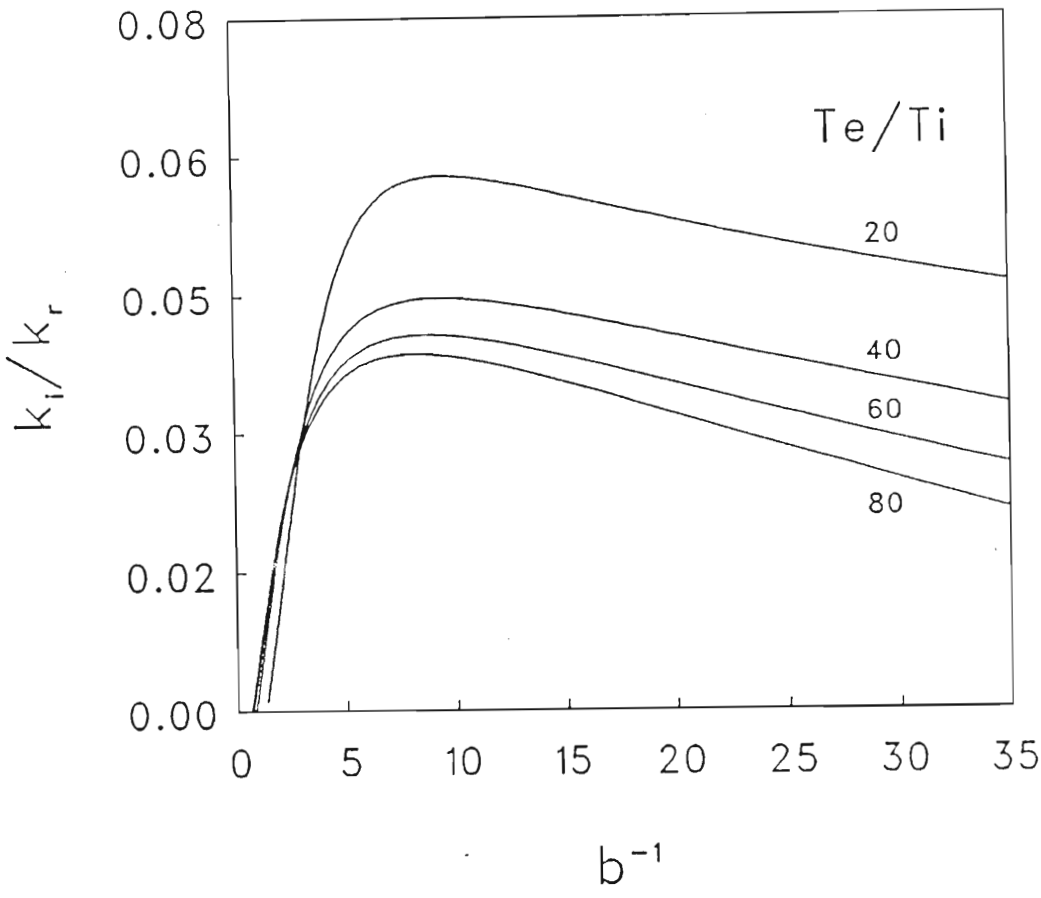

Figure 2.10: Growth rate as a function of the parameter $b^{-1} = 2(k\rho_e)^{-2}$ for the conditions: $B = 23$ gauss, $W_o = 32$ eV, $N_o = 1 \times 10^8$ cm^{-3}, $m_i/m_e = 73440$, $k_\parallel/k_\perp = 0.015$, $x = 35$ cm, $\lambda_{ce}/\lambda_{ci} = 100$, $\lambda_{ci} = 25$ cm. The parameter labeling the curves is T_e/T_i, and T_i is fixed at 0.05 eV.

When considering the effect of change in electron temperature it is important to know the position of the inflection point of the electron velocity distribution function relative to the phase velocity as the slope determines the growth rate. The maximum value of $\partial f_e/\partial v$ occurs at $v = C_e/\sqrt{2}$. If the phase velocity is less than $C_e/\sqrt{2}$ an increase in electron temperature means a decrease in $\partial f_e/\partial v$ and therefore a lower growth rate.

2.4.4 The effect of electron density on the growth rate

In Figure 2.11 growth rate curves are shown at different values of the plasma density. As density is decreased the growth rate decreases. This is explained in terms of particle-instability resonance. The higher the plasma density, the greater the number of particles that can supply energy to the instability, thus increasing the growth rate.

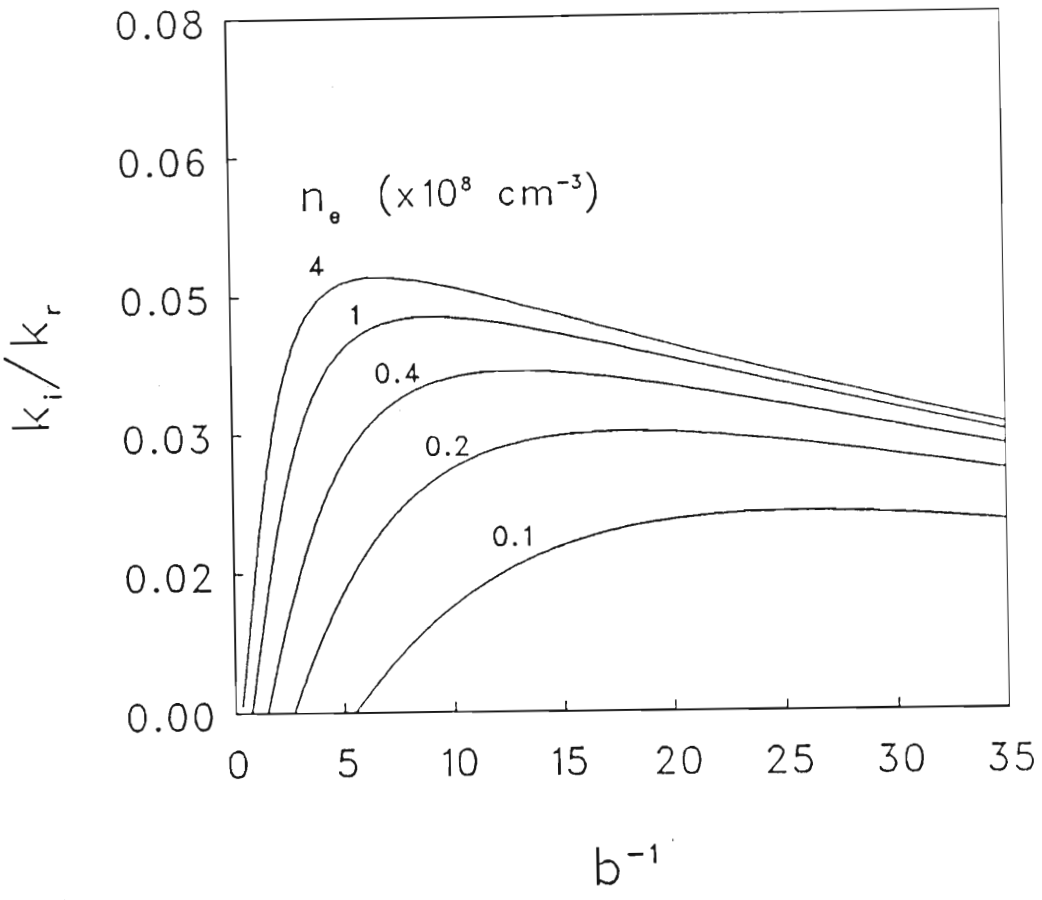

Figure 2.11: Growth rate as a function of the parameter $b^{-1} = 2(k_\perp \rho_e)^{-2}$ at various values of plasma density, n_e. With: $T_e/T_{ib} = 48$, $T_e = 2.4$ eV, $B = 23$ gauss , $W_o = 32$ eV, $V_o/C_s = 5.2$, $m_i/m_e = 73440$, $k_\parallel/k_\perp = 0.015$, $x = 35$ cm, $\lambda_{ce}/\lambda_{ci} = 100$, $\lambda_{ci} = 25$ cm.

2.4.5 The effect of beam velocity on the instability

The growth rate is represented as a function of $b^{-1} = 2(k_\perp \rho_e)^{-2}$ for different values of beam velocity in figure 2.12. The parameter labeling the curves is the normalized beam velocity V_o/C_s. The larger the beam velocity, the larger the growth rate.

More information can be obtained by plotting the growth rate as a function of V_o/C_s; see figure 2.13. The parameter labeling the curves is frequency (in kHz). For $V_o/C_s \geq 2$ the growth rate decreases as the beam velocity decreases (except at the lowest frequencies). This behavior corresponds to that in Figure 2.12. A new region is however evident for small values of beam energy. Here the growth rate increases as the beam velocity decreases until it reaches a maximum at $V_o/C_s \approx 1$. If the beam velocity is decreased further the growth rate decreases and reach a cut off value at $V_o/C_s \approx 0.5$. This low frequency resonant peak that appears when the beam velocity approaches the ion sound speed, C_s, is characteristic of the ion-ion instability. A similar result was obtained by AKIMOTO and OMIDI [1] and was also referred to by SING [46]. At higher values of the frequency, eg. $f = 400$ kHz, there is a clear separation between the ion acoustic and ion-ion modes: The cut off point for the ion acoustic instability at this frequency is at $V_o/C_s \approx 2$ and the ion-ion instability appears at $V_o/C_s \approx 0.8$.

Reduction of the background plasma is found to decrease the growth rate of the ion-ion instability. In figure 2.14 the effect of background plasma is examined. The frequency is fixed at 250 kHz. It is assumed that no elastic collisions take place and therefore by varying the amount of background ions, the charge exchange mean free path is varied. The charge exchange mean free path labels the curves and as this is increased the growth rate of the ion acoustic instability increases and that of the ion-ion instability decreases. As there are fewer background ions to resonate with the beam ions, the growth rate of the ion-ion instability decreases. Furthermore fewer ions will be lost from the beam, and this leads to a larger growth rate of the cross-field ion acoustic instability.

The ion-ion instability is sensitive to the background ion temperature T_{io} as this instability is driven by the interaction between the beam and background ions [46]. The ion-acoustic instability is insensitive to T_{io} as it is driven unstable by resonant electrons and the plasma wave. Figure 2.15

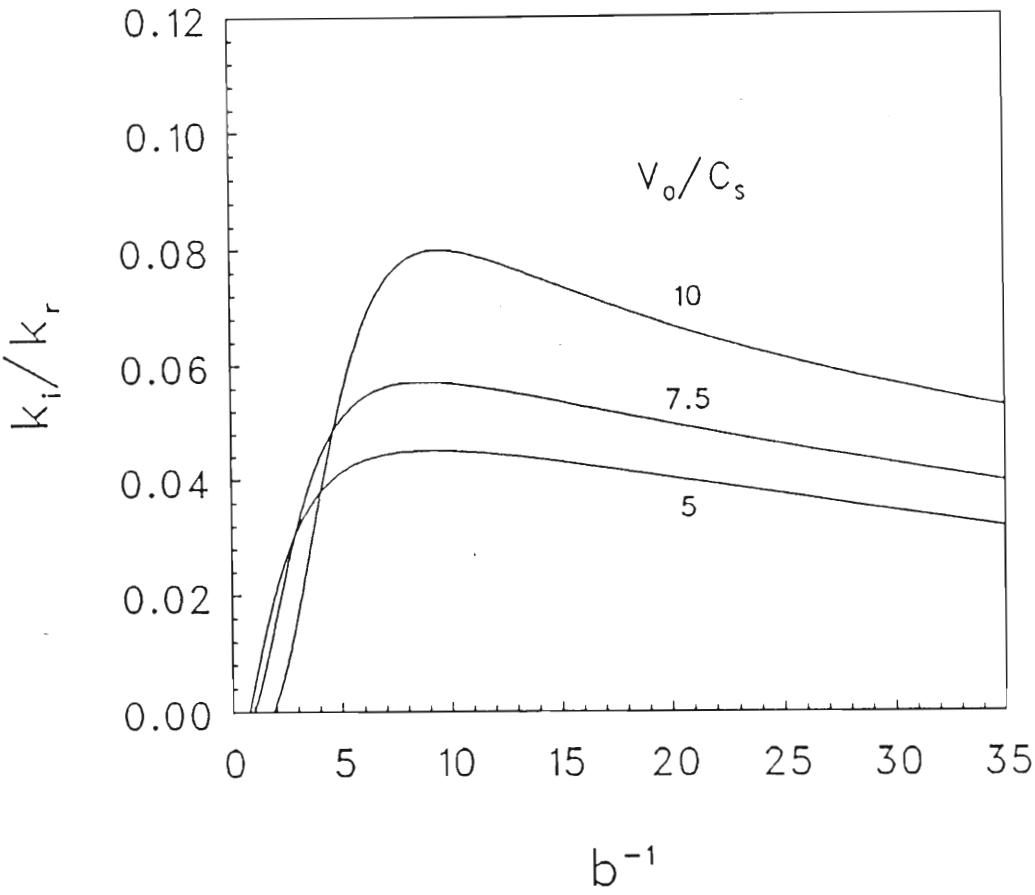

Figure 2.12: Growth rate as a function of the parameter $b^{-1} = 2(k_\perp \rho_e)^{-2}$ at various values of beam velocity for the following conditions: $T_e/T_{ib} = 48$, $T_{io}/T_{ib} = 1$, $T_e = 2.4$ eV, $B = 23$ gauss $N_o = 1 \times 10^8$ cm^{-3}, $m_i/m_e = 73440$, $k_\parallel/k_\perp = 0.015$, $x = 35$ cm, $\lambda_{ce}/\lambda_{ci} = 100$, $\lambda_{ci} = 25$cm. The parameter labeling the curves is V_o/C_s.

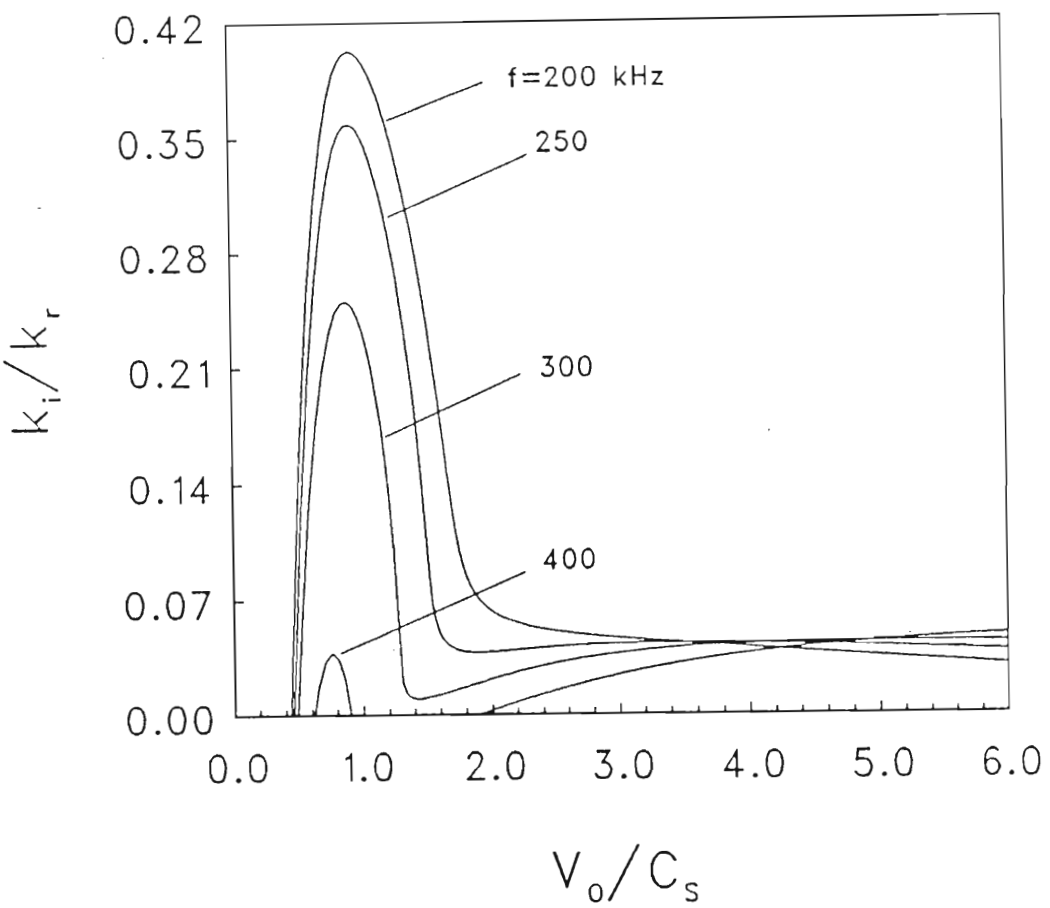

Figure 2.13: Growth rate as a function of normalized beam velocity, V_o/C_s at various frequencies. Where: $T_e/T_{ib} = 48$, $T_{io}/T_{ib} = 1$, $T_e = 2.4$ eV, $B = 23$ gauss $N_o = 1 \times 10^8$ cm^{-3}, $m_i/m_e = 73440$, $k_\parallel/k_\perp = 0.015$, $x = 35$ cm, $\lambda_{ce}/\lambda_{ci} = 100$, $\lambda_{ci} = 25$ cm. The parameter labeling the curves is frequency (kHz).

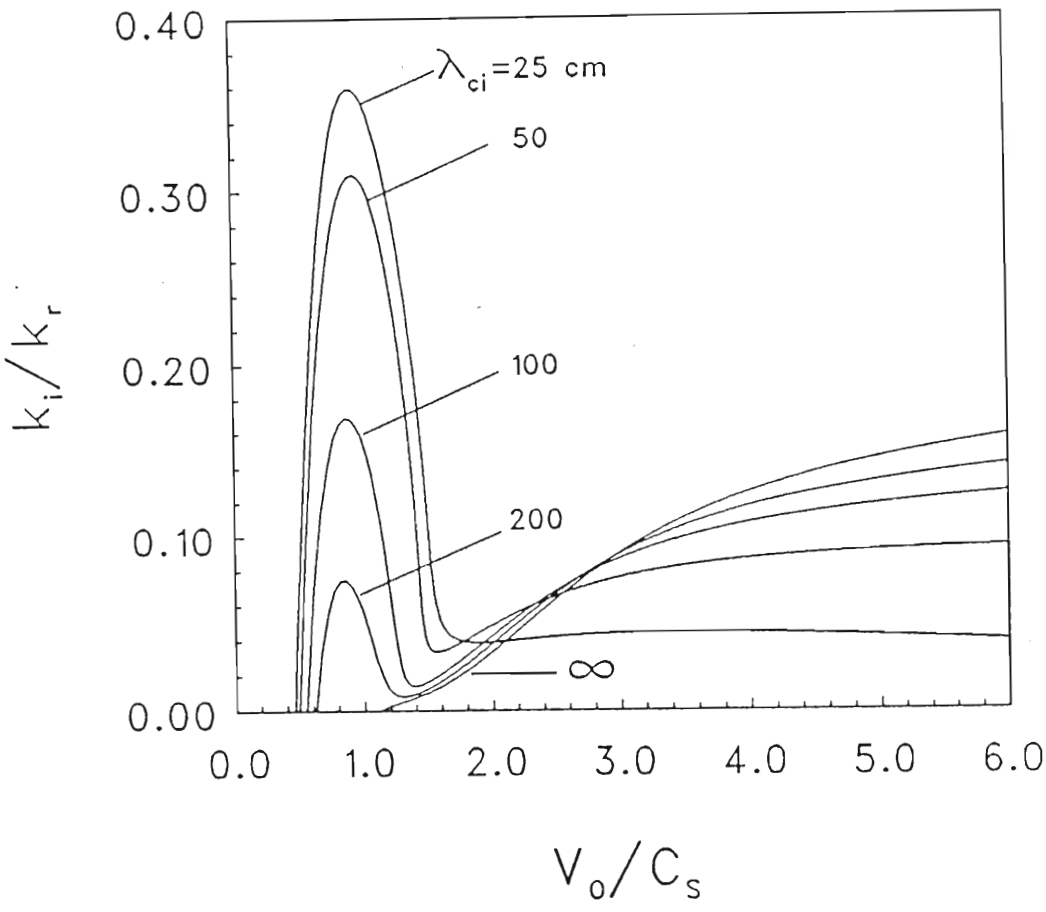

Figure 2.14: Growth rate as a function of V_o/C_s at various values of the charge exchange mean free path. Where: $T_e/T_{ib} = 48$, $T_{io}/T_{ib} = 1$, $T_e = 2.4$ eV, $B = 23$ gauss $N_o = 1 \times 10^8$ cm^{-3}, $m_i/m_e = 73440$, $k_\parallel/k_\perp = 0.015$, $x = 35$ cm, $\lambda_{ce} = \infty$, $f = 250$ kHz. The parameter labeling the curves is λ_{ci}.

illustrates these effects where k_i/k_r is plotted as a function of V_o/C_s at various values of normalized background ion temperature T_{io}. As this ratio increases, the maximum growth rate decreases and occurs at lower values of beam velocity.

It should be noted that the ion beam temperature T_{ib} depends on the beam energy W_o [31,33].

$$T_{ib} = \frac{\Delta W^2}{4 W_o}$$

with ΔW the energy half width of the beam ions. The beam ion temperature will therefore increase as the beam velocity is reduced. The fraction T_e/T_{ib} will therefore decrease, leading to a decreased growth rate as illustrated in Figure 2.9. The ion-ion instability will therefore not be observed, as the growth rate decreases with decreasing V_o/C_s; see Figure 2.16.

2.4.6 The effect of magnetic field on the growth rate

Further growth rate curves (k_i/k_r versus $k\lambda_D$) are shown in Figure 2.17. Here the parameter labelling the curves is the magnetic field. For each curve B is fixed and k is varied by changing the frequency. In the theoretical model only the electrons are considered magnetized as $\omega_{ci} \ll \gamma \ll \omega_{ce}$, γ being the imaginary part of ω and ω_{ci} and ω_{ce} respectively the ion and electron cyclotron frequencies. As the magnetic field increases from zero, the electron motion becomes essentially one-dimensional (along B) and the effective electron temperature as observed in the direction of wave propagation will decrease by a factor $k_\parallel/k_\perp$; see section 2.3. The greater the magnetic field the larger the ratio λ/ρ_e and the more nearly one dimensional is the electron motion (with its consequent enlargement of the growth rate).

Figure 2.18 shows growth rate curves (k_i/k_r versus $1/\sqrt{2}\ k_\perp \rho_e$) corresponding to various frequencies. Here k is fixed (by the frequency) and the magnitude of the magnetic field is varied. As k and ω are increased, the growth rate is increased at fixed B, a maximum is reached (at f $\approx$ 450 kHz) and the growth rate then decreases at higher frequencies. This behaviour is shown explicitly in Figure 2.17.

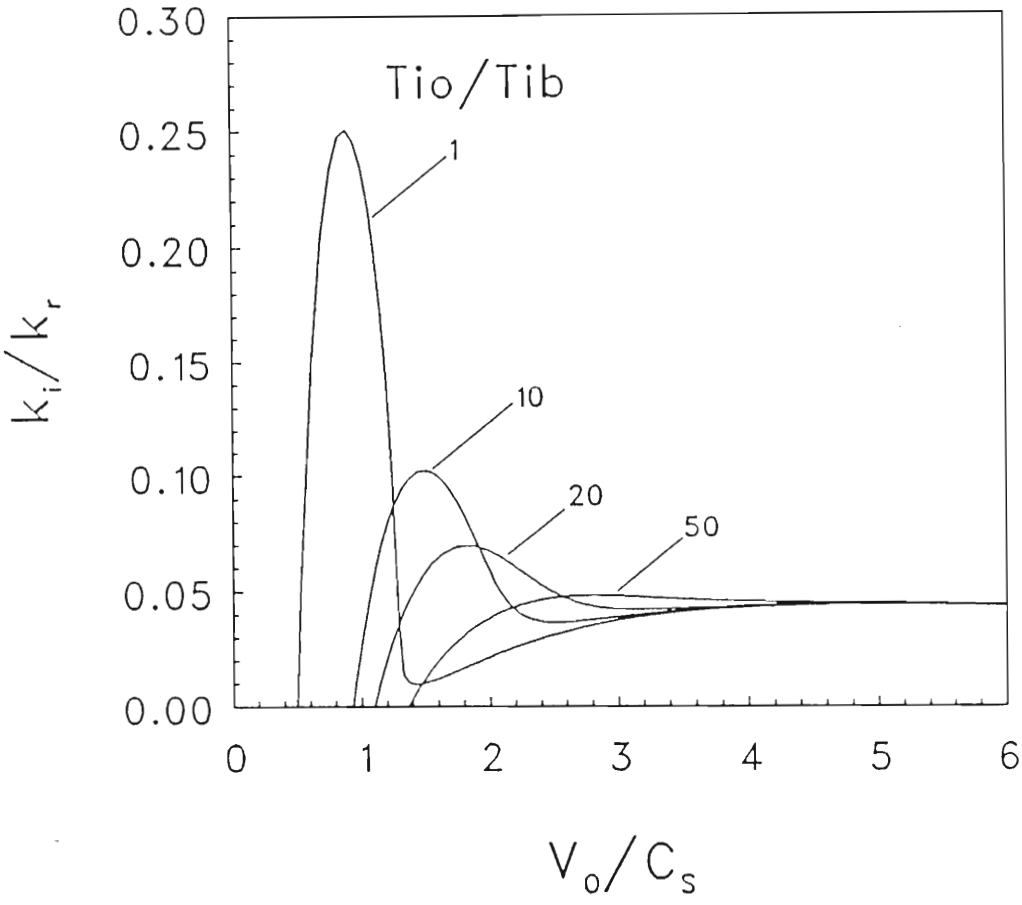

Figure 2.15: Growth rate as a function of V_o/C_s at various values of T_{io}/T_{ib}. Where: $T_e/T_{ib} = 48$, $T_e = 2.4$ eV, $B = 23$ gauss $N_o = 1 \times 10^8$ cm^{-3}, $m_i/m_e = 73440$, $k_\parallel/k_\perp = 0.015$, $x = 35$ cm, $\lambda_{ce} = \infty$, $f = 300$ kHz.

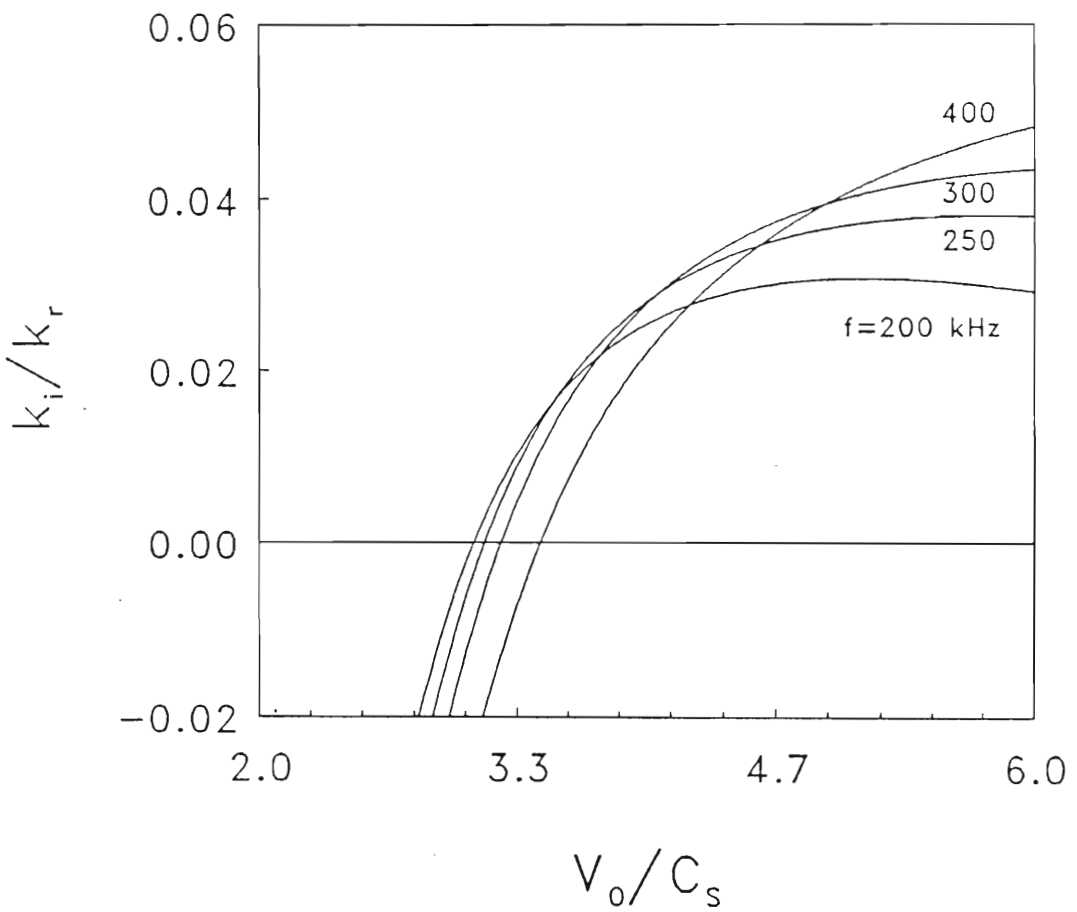

Figure 2.16: Growth rate as a function of V_o/C_s at various values of T_{io}/T_{ib}. Where: $T_{ib} = \frac{\Delta W^2}{4W_o}$, $T_e = 2.4$ eV, $B = 23$ gauss $N_o = 1 \times 10^8$ cm^{-3}, $m_i/m_e = 73440$, $k_\parallel/k_\perp = 0.015$, $x = 35$ cm, $\lambda_{ce} = \infty$, $f = 300$ kHz.

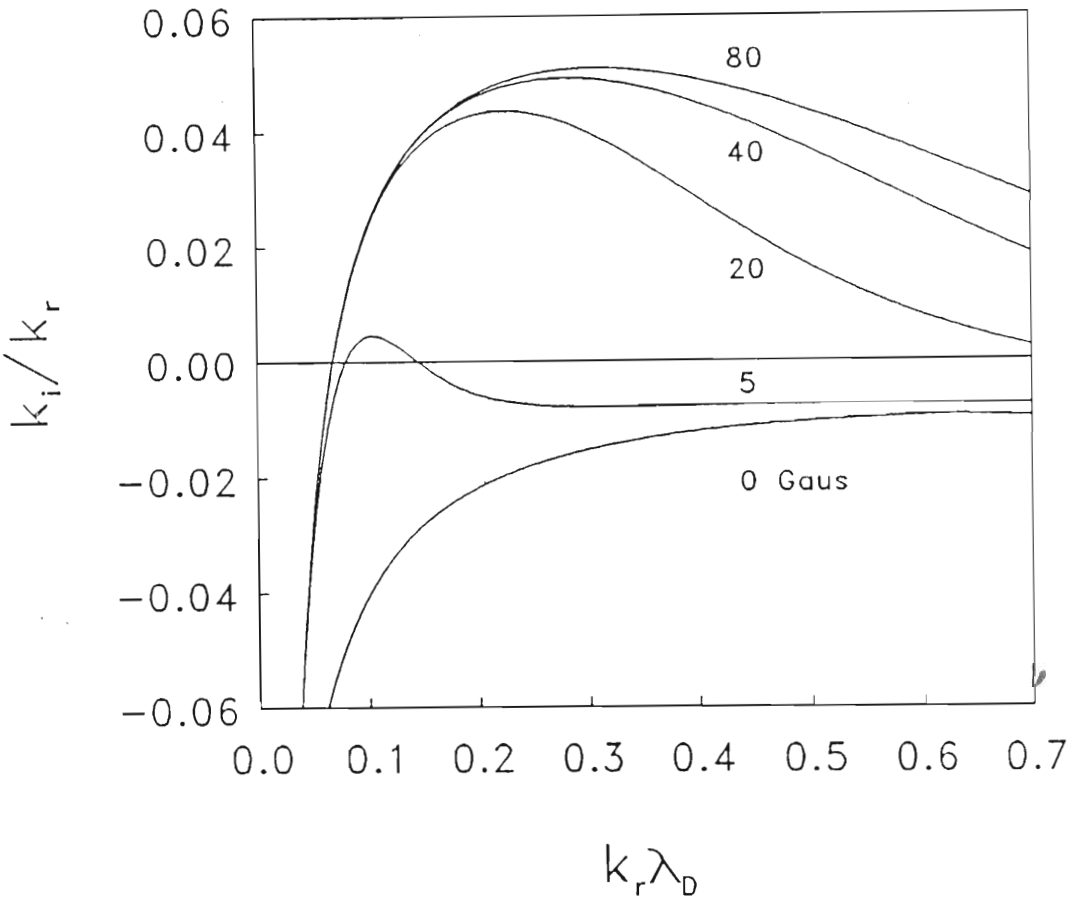

Figure 2.17: Growth rate as a function of the parameter $b^{-1} = 2(k_\perp \rho_e)^{-2}$ at various values of the magnetic field. Where: $T_e/T_{ib} = 48$, $T_e = 2.4$ eV, $W_o = 32$ eV, $V_o/C_s = 5.2$, $N_o = 1 \times 10^8$ cm^{-3}, $m_i/m_e = 73440$, $k_\parallel/k_\perp = 0.015$, $x = 35$ cm, $\lambda_{ce}/\lambda_{ci} = 100$, $\lambda_{ci} = 25$ cm. The parameter labeling the curves is magnetic field (in gauss).

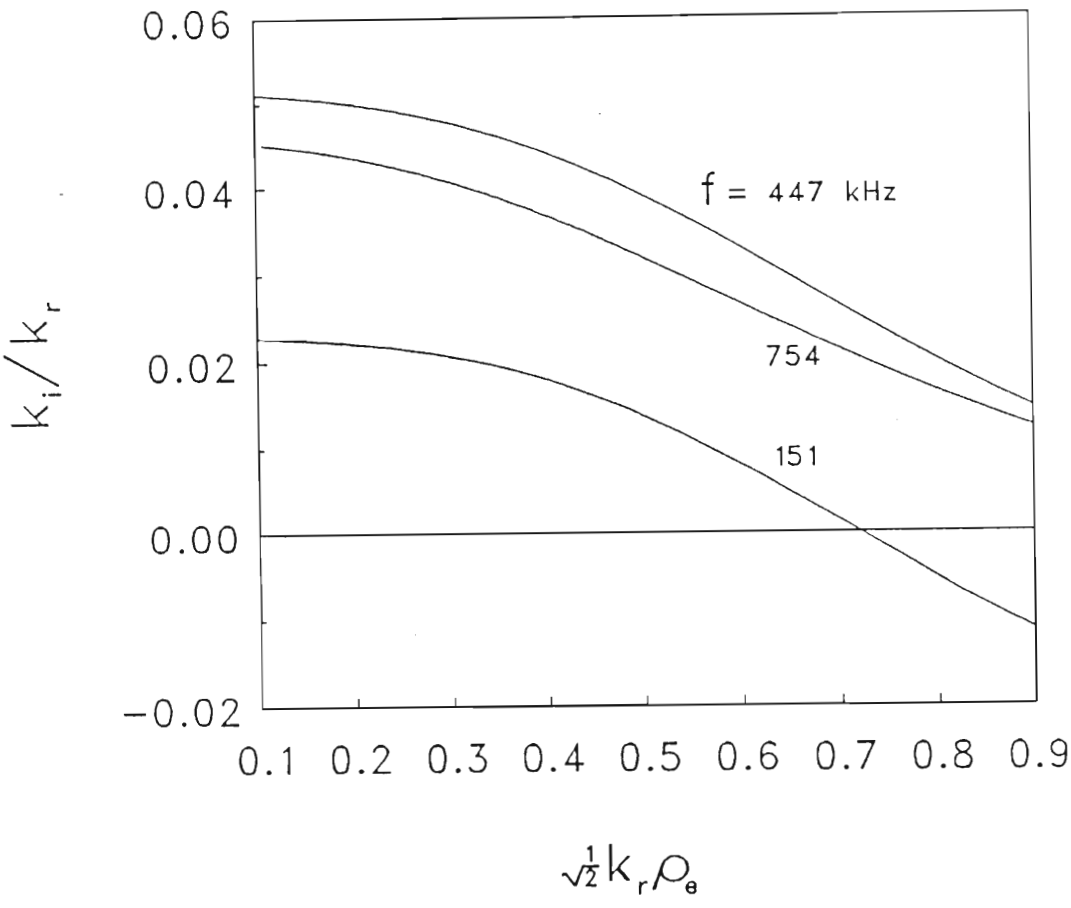

Figure 2.18: Growth rate as a function of the parameter $2^{-1/2}\ k_\perp \rho_e$ at various frequencies. Where: $T_e/T_{ib} = 48$, $T_e = 2.4$ eV, , $W_o = 32$ eV, $V_o/C_s = 5.2$, $N_o = 1 \times 10^8$ cm^{-3}, $m_i/m_e = 73440$, $k_\parallel/k_\perp = 0.015$, $x = 35$ cm, $\lambda_{ce}/\lambda_{ci} = 100$, $\lambda_{ci} = 25$ cm. The parameter labeling the curves is frequency (in kHz) and $2^{-1/2}\ k_\perp \rho_e$ was varied by changing the magnetic field.

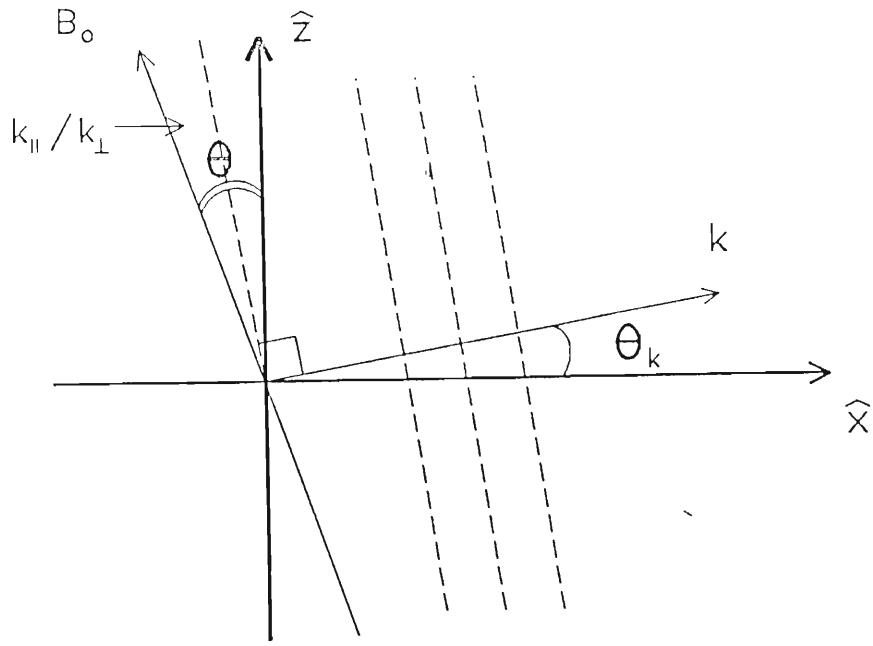

Figure 2.19: Uni-directional wavefronts propagating at an angle θ_k with respect to the ion beam direction $\hat{\mathbf{x}}$. The magnetic field making an angle θ with respect to $\hat{\mathbf{z}}$, effectively limits the electron motion to one dimension thus decreasing the electron thermal velocity C_e by a factor $k_{\parallel}/k_{\perp}$. This factor can also be expressed in terms of the angle between $\mathbf{B}$ and the normal to $\mathbf{k}$: $k_{\parallel}/k_{\perp} = \mid \theta - \theta_k \mid$.

2.4.7 The effect of varying the angle $\mid \theta - \theta_k \mid$ between the magnetic field direction and the direction of beam propagation

It is assumed that the instability propagates with uni-directional wave fronts at an angle θ_k to the beam direction $\hat{\mathbf{x}}$. This is illustrated in Figure 2.19. The angle between the normal to the wave propagation direction and the magnetic field is given by $k_{\parallel}/k_{\perp} = \mid \theta - \theta_k \mid$, with θ the angle between the magnetic field direction and $\hat{\mathbf{z}}$. Experimentally, θ is variable (by rotation of the magnetic field coils) and the wave fronts adjust their direction to some smaller angle θ_k. As explained in section 2.3 the motion of the electrons is limited to the magnetic field direction. The electron thermal velocity is therefore effectively projected onto $\mathbf{k}$, reducing the effective thermal velocity to $C_e' = k_{\parallel}/k_{\perp} C_e$. The growth rate therefore depends strongly on $k_{\parallel}/k_{\perp}$ as is illustrated in Figure 2.20 [5,33]. As $k_{\parallel}/k_{\perp}$ decreases the growth rate increases until a maximum is reached at c. Here $\omega/k_{\parallel}$ corresponds to a large

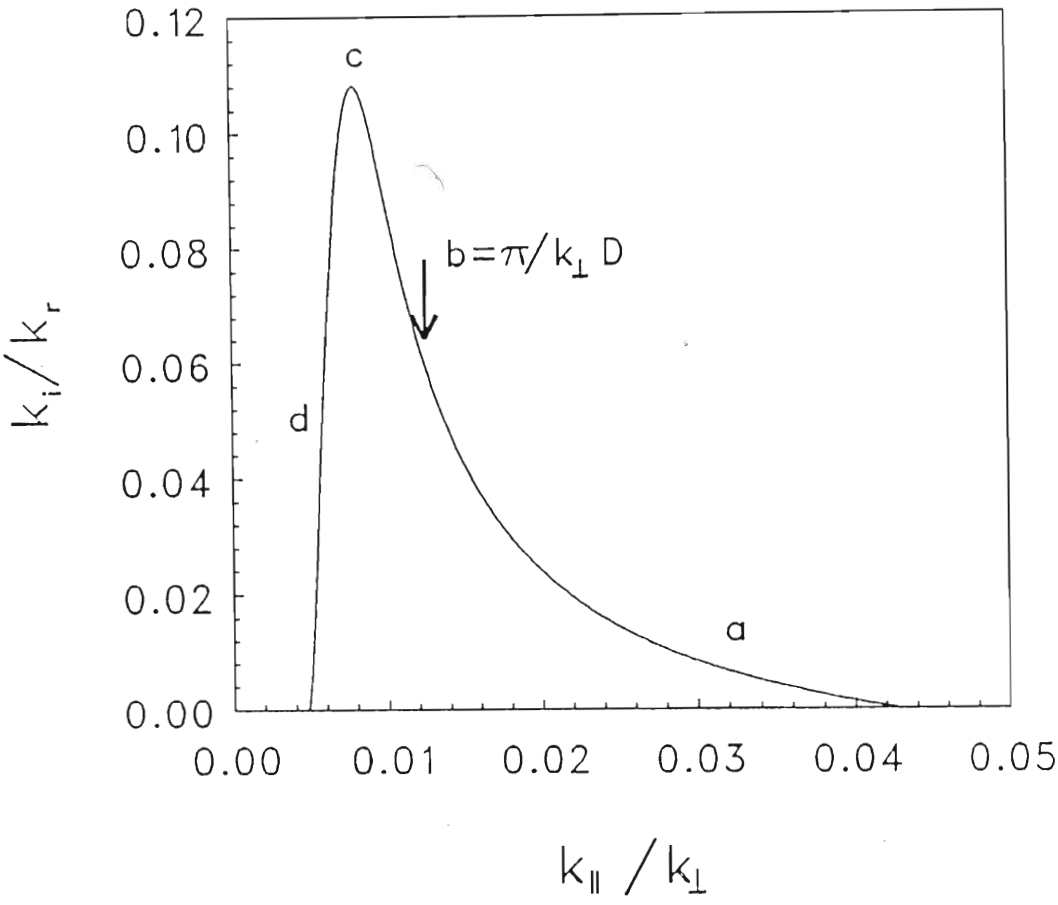

Figure 2.20: Growth rate as a function of the angle $k_\parallel/k_\perp$. Where: $T_e/T_{ib} = 48$, $T_e = 2.4$ eV, $B = 23$ gauss , $W_o = 32$ eV, $V_o/C_s = 5.2$, $N_o = 1 \times 10^8$ cm^{-3}, $m_i/m_e = 73440$, $x = 35$ cm, $\lambda_{ce}/\lambda_{ci} = 100$, $\lambda_{ci} = 25$ cm. The vertical arrow indicates the minimum value of $k_\parallel$ as determined by the parallel length D of the experimental device.

slope of the electron velocity distribution function (leading to maximum inverse Landau damping) at

$$\omega/k \approx k_{\|}/k_{\perp}C_e.$$

Or simply

$$\omega/k_{\|} \approx C_e.$$

The growth rate decreases rapidly over region d where $\omega/k_{\|} > C_e$, because there are few resonant electrons. In Figure 2.21 the growth rate is plotted against the magnetic field angle θ, with the propagation angle θ_k fixed at 0.015 radians.

The curve in Figure 2.21 is symmetrical about this value of θ_k. As explained above, there is a sharp decrease of growth rate as θ approaches θ_k. An equivalent explanation for the decrease is: For electrons to move from a region of low potential to a region of high potential the path is determined by the magnetic field lines. If the magnetic field direction is changed without altering the direction of wave propagation, this distance will increase as θ approaches θ_k. It follows that if $\theta \approx \theta_k$, electrons can no longer equalize regions of different potential, therefore the instability will be strongly damped.

2.4.8 The effect of finite geometry on the growth rate

In Figure 2.20 the growth rate is represented as a function of $k_{\|}/k_{\perp}$ or $(\theta - \theta_k)$ where θ is the angle of the magnetic field relative to $\hat{\mathbf{z}}$, and θ_k is the angle between the beam direction and the wave vector. If it is assumed that the parallel wave length of the instability is limited to twice the width D of the plasma along $\mathbf{B}$, then the maximum parallel wave number is

$$k_{\|} = 2\pi/\lambda_{\|} = \pi/D$$

The growth rate in figure 2.20 will increase from point a to b if $k_{\perp}$ is held constant and $k_{\|}$ is decreased. At b the dimension of the apparatus will restrict the parallel wave length, and prevent $k_{\|}$ from becoming any smaller. The remainder of the growth rate curve, d is therefore not accessible and will have a constant value corresponding to the growth rate at point b.

This is further illustrated in Figure 2.22 for uni-directional wave fronts where the growth rate at various parallel dimensions, D is plotted against magnetic

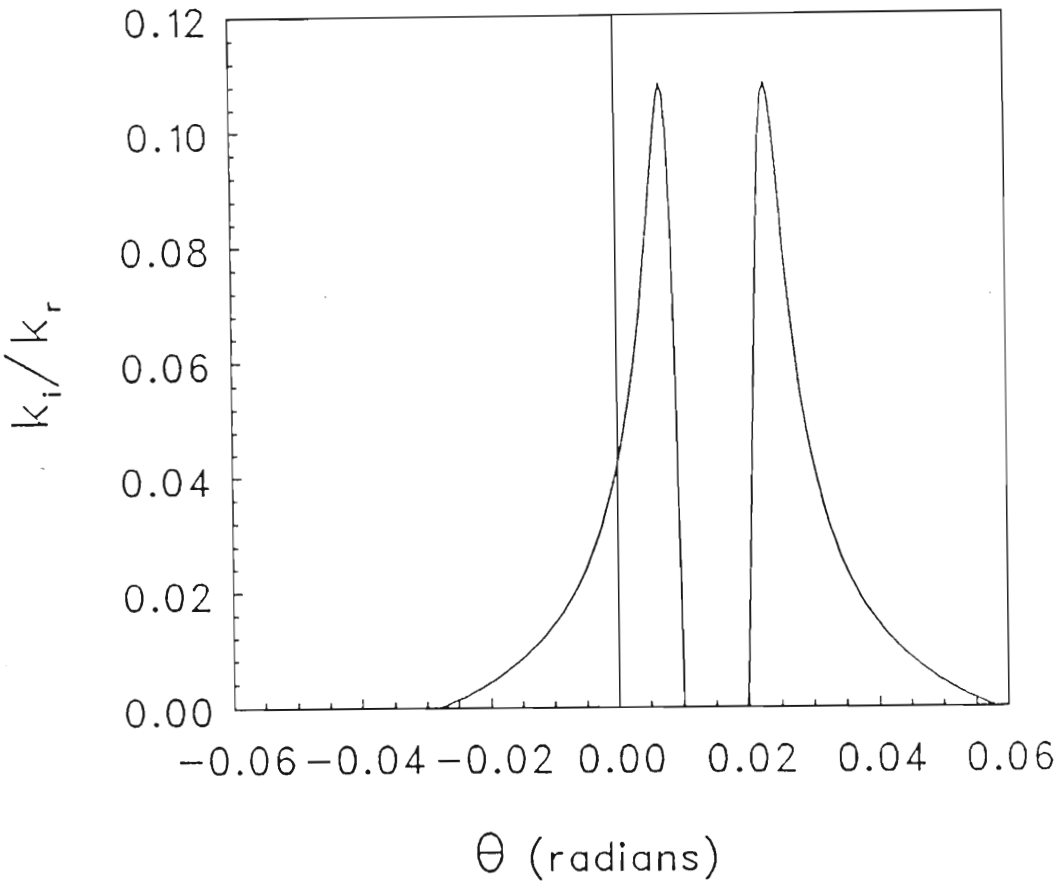

Figure 2.21: Growth rate as a function of angle relative to the magnetic field direction, $k_{\|}/k_{\perp}$. Where: $T_e/T_{ib} = 48$, $T_e = 2.4$ eV, $B = 23$ gauss , $W_o = 32$ eV, $V_o/C_s = 5.2$, $N_o = 1 \times 10^8$ cm^{-3}, $m_i/m_e = 73440$, $k_{\|}/k_{\perp} = 0.015$, $x = 35$ cm, $\lambda_{ce}/\lambda_{ci} = 100$, $\lambda_{ci} = 25$ cm.

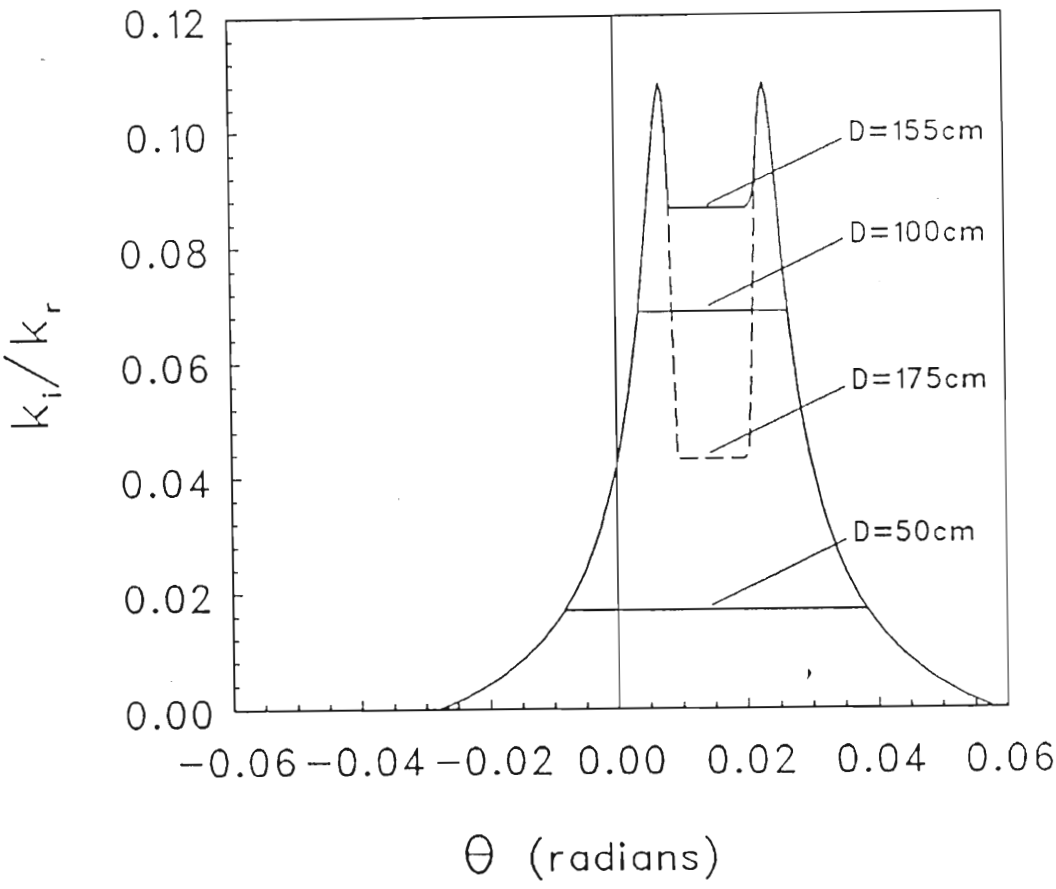

Figure 2.22: Growth rate as a function of magnetic field angle, θ for various values of parallel dimension D. Where: $T_e/T_{ib} = 48$, $T_e = 2.4$ eV, $B = 23$ gauss , $W_o = 32$ eV, $V_o/C_s = 5.2$, $N_o = 1 \times 10^8$ cm^{-3}, $m_i/m_e = 73440$, $k_\parallel/k_\perp = 0.015$, $x = 35$ cm, $\lambda_{ce}/\lambda_{ci} = 100$, $\lambda_{ci} = 25$ cm. The parameter labeling the curves is the plasma width D (in cm). The parallel wavelength is $\lambda_\parallel = 140\,\mathrm{cm}^{-1}$.

field angle θ. As the parallel dimension D increases a larger portion of the curve is accessible and the growth rate increases up to point c and then starts to decrease again. In Figure 2.23 the growth rate is plotted against $b^{-1} = 2(k_r\rho_e)^{-2}$ for various values of parallel dimension D. As the parallel wave length is limited by the dimensions of the apparatus, the growth rate decreases with increasing b^{-1} (i.e. increasing λ). The discontinuities that is appear for larger values D indicate the transition between the case of an infinite plasma and a plasma with a finite width D.

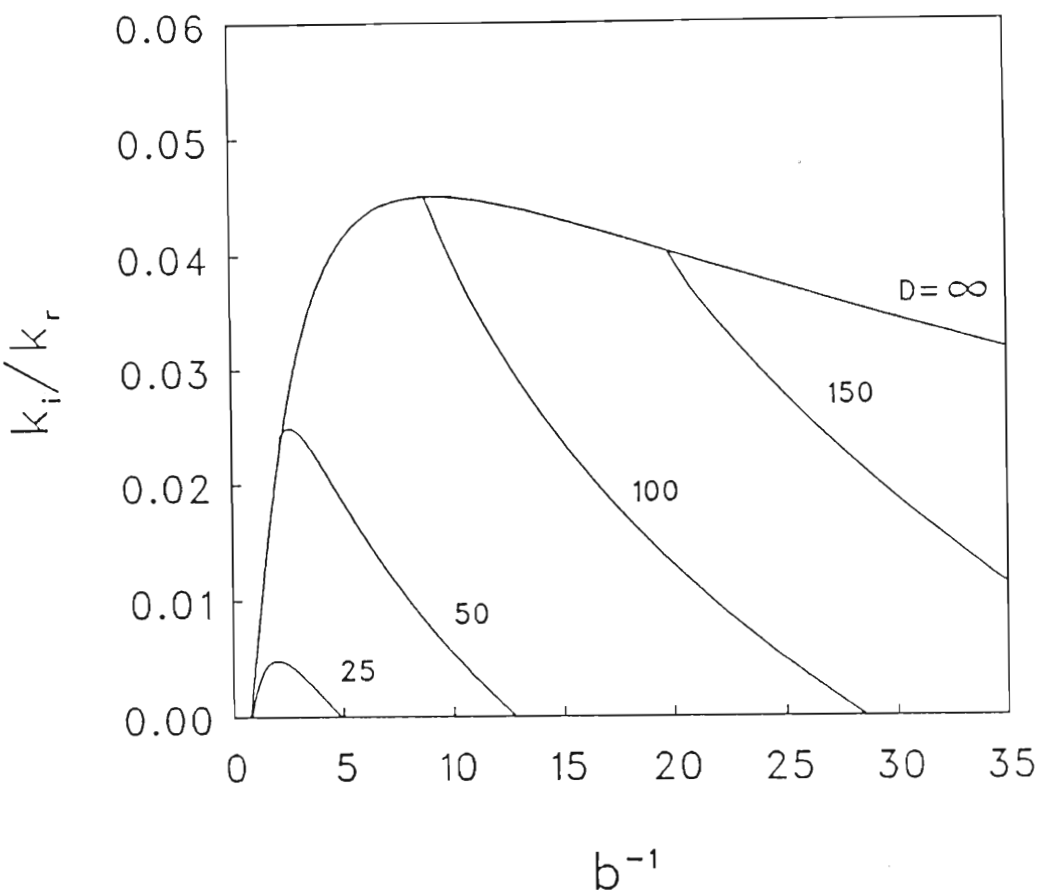

Figure 2.23: Growth rate as a function of $b^{-1} = 2(k_\perp \rho_e)^{-2}$ at various values of parallel dimension, D. Where: $T_e/T_{ib} = 48$, $T_e = 2.4$ eV, $B = 23$ gauss , $W_o = 32$ eV, $V_o/C_s = 5.2$, $N_o = 1 \times 10^8$ cm^{-3}, $m_i/m_e = 73440$, $k_\parallel/k_\perp = 0.015$, $x = 35$ cm, $\lambda_{ce}/\lambda_{ci} = 100$, $\lambda_{ci} = 25$ cm. The parameter labeling the curves is plasma width D (in cm).

Chapter 3

EXPERIMENTAL ARRANGEMENT

The experimental work contained in this thesis was carried out by the author on the Triple Plasma Device (TP) at the University of Natal in Durban. A significant part of this project involved the construction of the ion source chamber and other internal components, together with the commissioning of the device.

A TP is normally arranged to produce two separate ion beams which interstream in the Target region. The experimental device is presently configured as a double plasma device [49] as only one ion beam is used. An argon discharge plasma is created in the source chamber and by biasing this chamber positively with respect to the main chamber an ion beam can be extracted from the source to the target chamber. A negatively biased grid between the two chambers prevents the electrons from flowing into the target chamber. Hot filaments in the target chamber produce electrons that neutralize the ion beam and thereby create a plasma in the target chamber.

3.1 Description of the Triple Plasma Device

The device consists of an aluminium vacuum chamber with large side ports and a main chamber length of 100 cm and diameter of 60 cm; (see Plate 1). Attached to the sides of this main chamber are two smaller auxiliary cham-

bers (20 cm long and with a diameter of 40 cm). In the triple plasma configuration two source chambers can be installed but in the present double plasma configuration only one source chamber is located in the main chamber and the target chamber filaments are located in the auxiliary chambers. See Figures 3.1 and 3.2 for details. The source chamber consists of a stainless steel vessel with a water cooled copper jacket on the outside. Clamped to this jacket are sixteen ceramic magnets (25 cm $\times$ 5 cm $\times$ 3 cm). Smaller ceramic magnets (5 cm $\times$ 2 cm $\times$ 0.5 cm) are attached to the back of the source chamber. These magnets form a multiple cusped field around the source chamber [43]; see Plate 2. The TP is evacuated by an oil diffusion pump to a base pressure of typically 8×10^{-7} Torr. Argon gas is leaked through a needle valve to give an operating pressure of typically 3×10^{-4} Torr.

Six filament supports are led through the end flange of the main chamber into the source chamber and are insulated by Teflon plugs. Sixteen tungsten filaments (diameter .006 inch) each 18 cm long are strung between the supports. These filaments are heated (typically 2 Amps per filament) and biased at -60 Volts with respect to the source chamber to form the cathode of the discharge. With the magnets installed a discharge current of 0.7 Amp will create a plasma in the source chamber of density $\approx 1 \times 10^9\,\mathrm{cm}^{-3}$. Without the magnets a discharge current of 8 Amps was required to produce this density. A separator grid consisting of a stretched stainless steel mesh (170 lines per cm and 70% transparent) sandwiched between two firm stainless steel rings, seals off the open end of the source chamber. It is insulated from the source chamber by pyrophyllite spacers (0.5 cm in thickness). To prevent the plasma from leaking through this opening a circular shielding-plate perpendicular to the grid and fitting into the source chamber opening was biased at -100 V relative to the source chamber to prevent the electron population from drifting into the target chamber. The source chamber can be biased positively with respect to the main chamber. This beam voltage will accelerate the ions into the target chamber, creating an ion beam of diameter $\approx$ 50 cm . (This bias, or beam voltage V_b, could be varied from 10 to $300V$); see Figures 3.2 and 3.3.

The ion beam is neutralized in the target chamber by electrons from hot grounded filaments. Filament supports enter through the auxiliary chambers and can be moved into the ion beam. Attached to the filament supports and about 3 cm behind each bank of filaments , is a thin stainless steel plate.

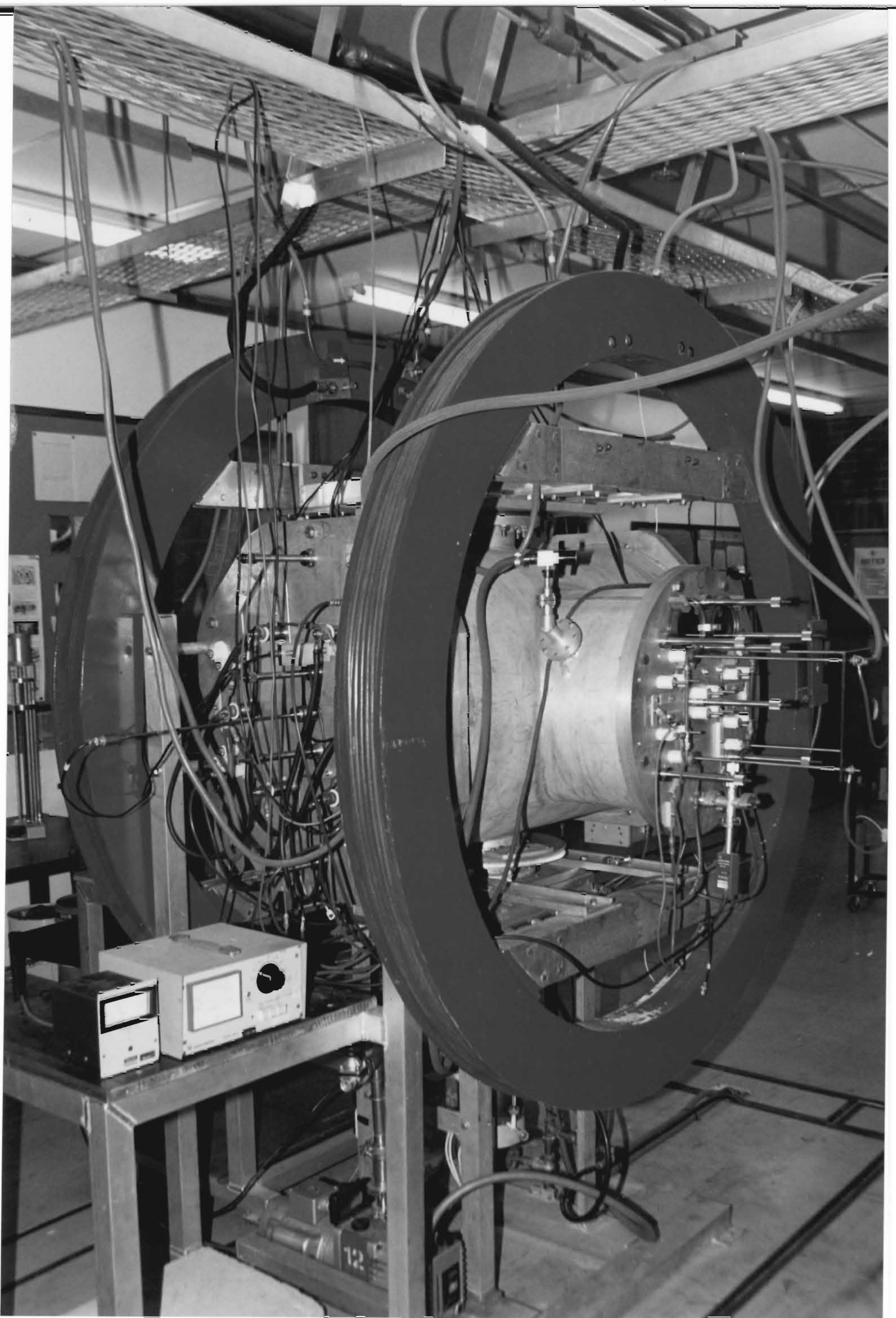

Plate 1
The Triple Plasma Device at the University of Natal, Durban.

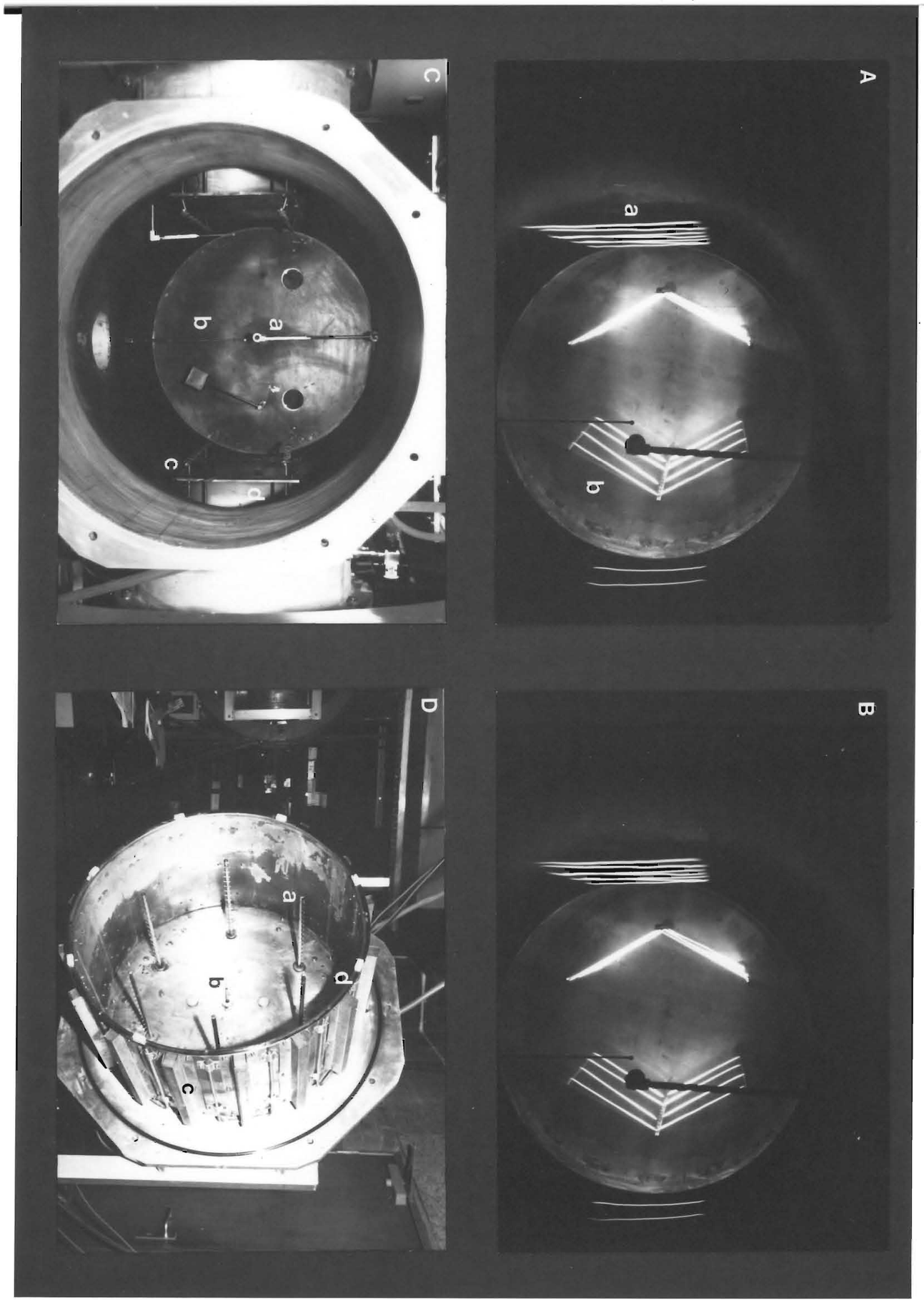

Plate 2 A

A high density discharge in the source chamber as viewed through a port hole in the end flange. The target chamber filaments *a* and source chamber filaments *b* are clearly visible. Due to back lighting the separator grid covering the source chamber is not distinguishable. The energy analyzer (top) and Langmuir probe (bottom) are in the foreground.

Plate 2 B

Close inspection of the purple discharge indicate the position and shape of the cusped magnetic field in the source chamber (no external magnetic field). This is contrasted with plate 2A where the Helmholtz coils provide an external magnetic field of 50 gauss, limiting the discharge in the vertical direction.

Plate 2 C

An axial view of the main chamber with the source chamber removed. Axial movement of the energy analyzer *a* and Langmuir probe *b* is used to characterize the central region of the plasma. The target chamber filaments and support are indicated by *c*. The plasma width is limited by moveable side plates *d*. (Plates 2A&B were taken through the right hand side port hole in the end flange).

Plate 2 D

The source chamber with the separator grid removed. Filament supports *a* are insulated with pyrophyllite plugs. A Langmuir probe *b* was used to determine the electron temperature and density. Ceramic magnets clasped in a water cooled copper jacket *c* provide a cusped field to enhance electron containment in the source chamber. Small ceramic blocks insulate the separator grid (not shown) from the source chamber.

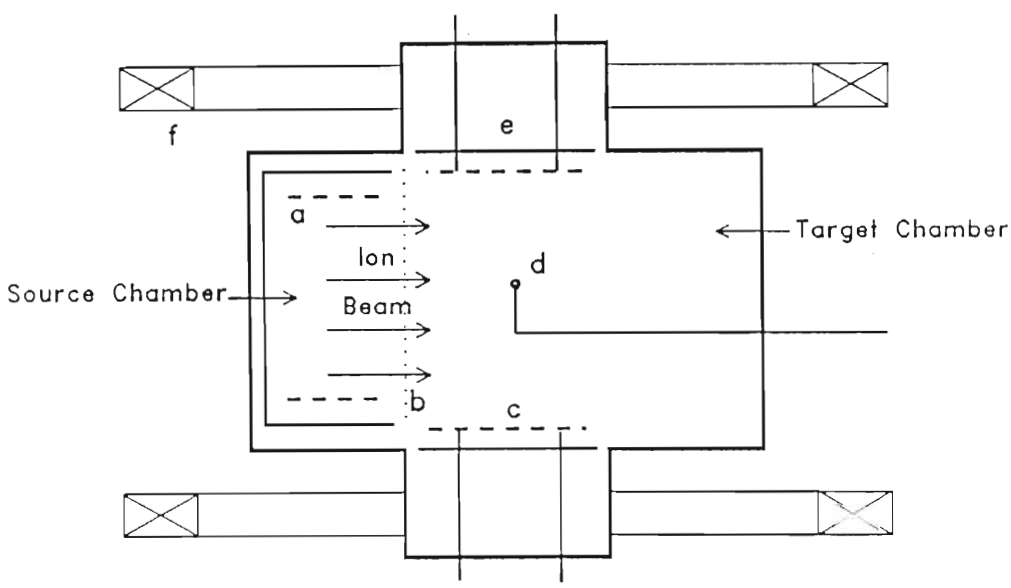

Figure 3.1: A plan view of the Triple plasma device. Biased hot filaments *a* create a discharge plasma in the source chamber. An ion beam is extracted through a negatively biased separator grid *b* into the target chamber where it is neutralized by electrons from hot filaments *c*. A moveable Langmuir probe *d* is used as a diagnostic. The plasma width can be changed with moveable end plates *e*. Two Helmholtz coils *f* create a magnetic field perpendicular to the ion beam direction.

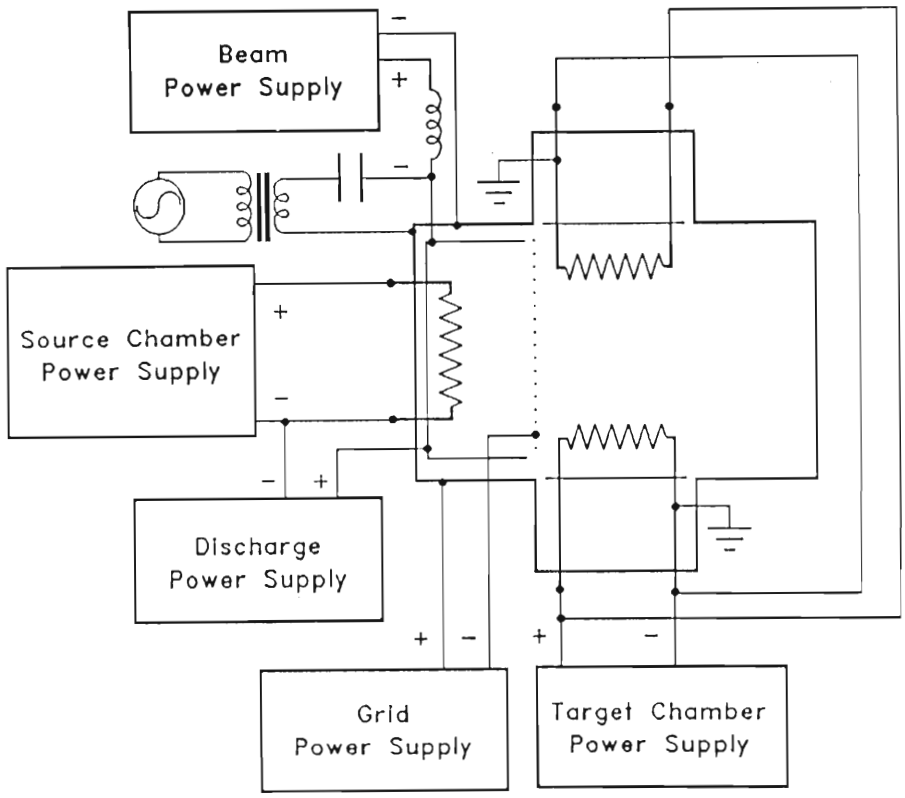

Figure 3.2: A diagram showing the filament power supplies used to operate the experimental device. The beam power supply biases the source chamber positive with respect to the target chamber, while the grid power supply biases the grid negatively to separate the source and target plasmas. This arrangement extracts an ion beam from the source into the target chamber. The ion beam is modulated by a small sinusoidal signal launched via the beam power supply circuit.

This serves two purposes: by moving the filament supports in or out, the dimension of the ion beam and plasma can be changed, and the stainless steel plates provide a good boundary for the plasma. (The main chamber is constructed from aluminium and after running the machine for a while it becomes coated with an oxide layer and ceases to be a good conductor.) A filament bank consists of 8 tantalum filaments (20 cm long and 0.12 mm in diameter) spaced 2 cm apart. In both the source and target chambers there is a potential drop of typically $16V$ across the filaments. Electrons will therefore be emitted with different energies at different positions on the filament. This will lead to an asymmetrical electron distribution which is undesirable, particularly in the target chamber. This effect was countered by biasing filaments so that the voltage drop in the two facing banks was in opposite directions.

Two Helmholtz coils provide a uniform transverse magnetic field in the target chamber region. The coils can provide a magnetic field of up to 80 Gauss. It is possible to change the field direction by rotating the coils with a wormwheel drive. A He-Ne laser mounted on top of the coil support structure is used to indicate the angle through which the coils are rotated by projecting the laser light on an opposite wall. This is illustrated in Figure 3.4.

3.2 Diagnostics

Two types of electrostatic diagnostics were used, a Langmuir probe and an energy analyzer. The Langmuir probe consists of a tantalum disc, (diameter typically 5 mm) coated on one side with ceramic cement and supported by a thin ceramic tube. The probe entered the main chamber from the flange facing the source chamber and a stepping motor drive was used to move it along the beam direction. This probe drive can also be controlled with a microcomputer. The Langmuir probe was used to calculate electron density and temperature, and was also used for interferometer traces. The associated electronics were designed by A. Hayzen [32].

The electrostatic energy analyzer consists of a stainless steel collecting plate 12 mm in diameter and two tungsten grids (70 lines per cm) [35]. This is illustrated in Figure 3.5. The outer grid was floating and the second grid

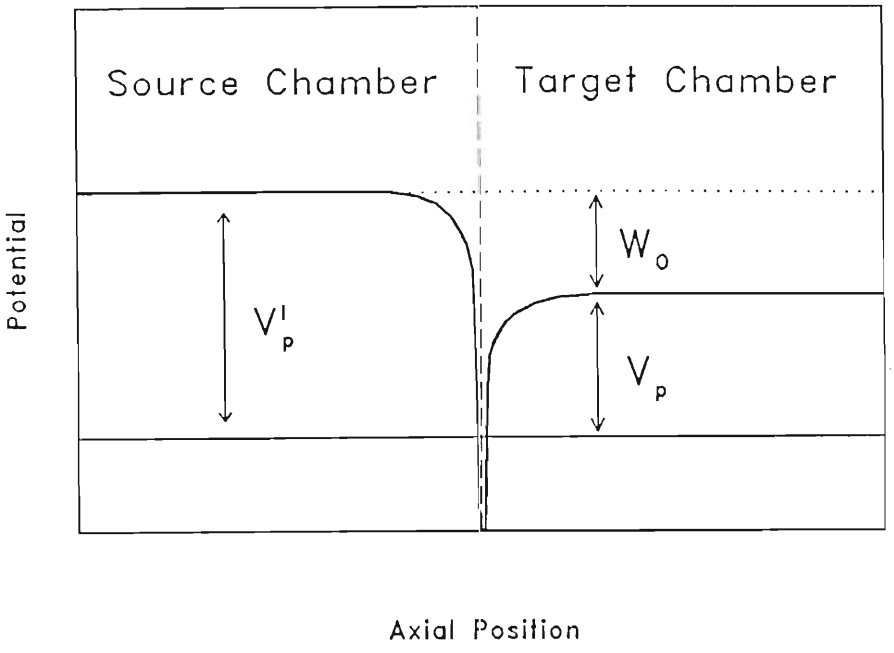

Figure 3.3: Diagram showing the axial potential profile between the source and target chambers, with V_p' and V_p the respective plasma potentials. The potential difference between the chambers accelerate the ions with a beam energy W_o. The separator grid is biased negatively to separate the electron species in the two chambers.

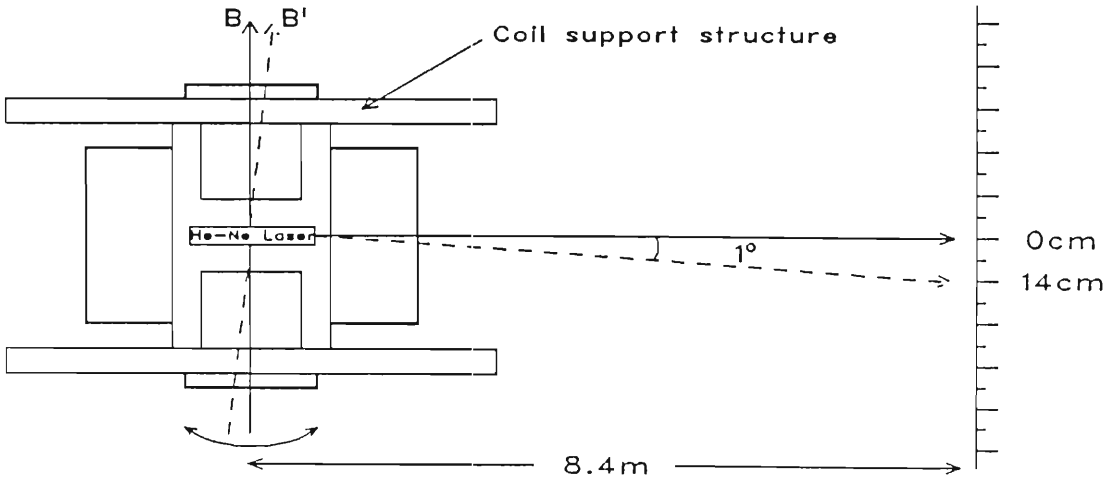

Figure 3.4: The plan view of the experimental device showing a He-Ne laser mounted on the support of the Helmholtz coils. By rotating the coils the change in magnetic field direction θ is read off a scale on the opposite wall ($1° = 14$ cm).

was biased at -30 V to repel incoming electrons. It was found that the grid spacing relative to the collector plate was crucial (≈ 0.1 mm), because with the mica washers too thick the energy analyzer's resolution decreased. The outer surface of the energy analyzer was coated with ceramic cement to minimize the disturbance to the plasma.

3.3 Data Acquisition and Analysis

An IBM-compatible microcomputer and two Gould digital storage oscilloscopes were used for data acquisition and analysis. The programming package used was ASYST, a FORTH-like high level programming environment that is especially suited for data acquisition and graphical display of data. Traces can be captured from the Goulds and analyzed or stored by the microcomputer. The electronic workshop designed a digital sweep that was programmed via the microcomputer.

3.3.1 Langmuir probe

Langmuir traces were obtained by using the probe sweep designed by A. Hayzen. These traces were captured on the Gould oscilloscope and then printed out on a XY-recorder or stored and analyzed on the microcomputer. The Langmuir probe traces were analyzed using the logarithmic method: For a maxwellian electron distribution the probe current I_e as a function of the probe potential V is given by the equation:

$$I_e = I_{eo} e^{(V-V_p)/T_e}$$

where $V < V_p$ (the plasma potential), T_e is the electron temperature in electron volts and I_{eo} is the electron saturation current (corresponding to $V = V_p$)

If we plot the natural logarithm of this equation

$$\ln I_e = \ln I_{eo} + \frac{V - V_p}{T_e},$$

T_e is obtained from the slope of $\ln I_e$ versus $(V - V_p)$. Once T_e and I_{eo} are

known, the electron density n_e can be calculated as from:

$$n_e = \frac{I_{eo}}{eA}\sqrt{\frac{2\pi m_e}{eT_e}}$$

where A is the collecting area of the probe. These results however apply to a collisionless unmagnetized plasma. CHEN *et al.* [17] found that when $r_p/\lambda_D \approx 1$ (where r_p is defined as the probe radius) the probe current is not proportional to n_e. CHEN also points out that the simple probe theory is inaccurate when $1 < r_p/\lambda_D < 10$ and if $r_p \geq \rho_e$. Typical parameters for this experiment are: $r_p/\lambda_D \approx 3$ and $r_p \approx \rho_e$ It would therefore be advisable to calculate the plasma density by using the ion saturation current instead as $\rho_i \gg \rho_e$. The uncertainty in measuring the ion saturation current is however much larger than that of I_{eo}. The density n_e was therefore calculated from I_{eo} as indicated above. The density measurements are therefore only to be taken as an indication of order of magnitude.

3.3.2 Energy analyzer

The collector plate of the energy analyzer was swept using the microcomputer controlled digital sweep. The external bias output on this sweep was fed to a current to voltage converter and thereafter differentiated using the AC input on the Gould oscilloscope. The circuit is illustrated in Figure 3.6 and typical outputs are presented in Figure 3.7. The ion temperature was then calculated from the differentiated traces. The beam speed is given by:

$$V_o = \sqrt{\frac{2eW_o}{m_i}}$$

The kinetic energy of the beam ions (in eV) is equal to the voltage separation of the beam and background ion peaks in the differentiated energy analyzer trace; Figure 3.7. which correspond to the beam and background ions respectively.

As explained by HAYZEN [31] the effective ion temperature T_{ib} is given by:

$$T_{ib} = \frac{\Delta W^2}{4W_o},$$

where ΔW is the energy half width of the beam ion energy distribution. The normalized rest ion density n_R/n_o is calculated from the energy analyzer

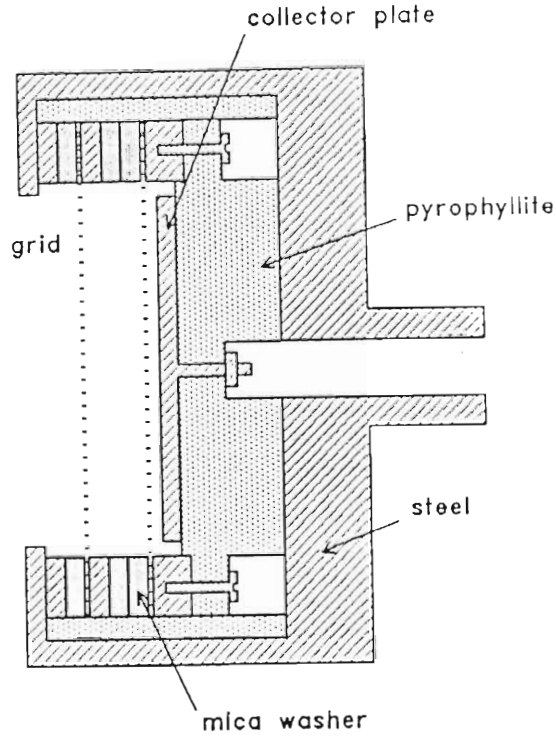

Figure 3.5: The electrostatic energy analyzer. There are two grids; the outer grid is floating and the inner grid is swept from 0 - 100 V.

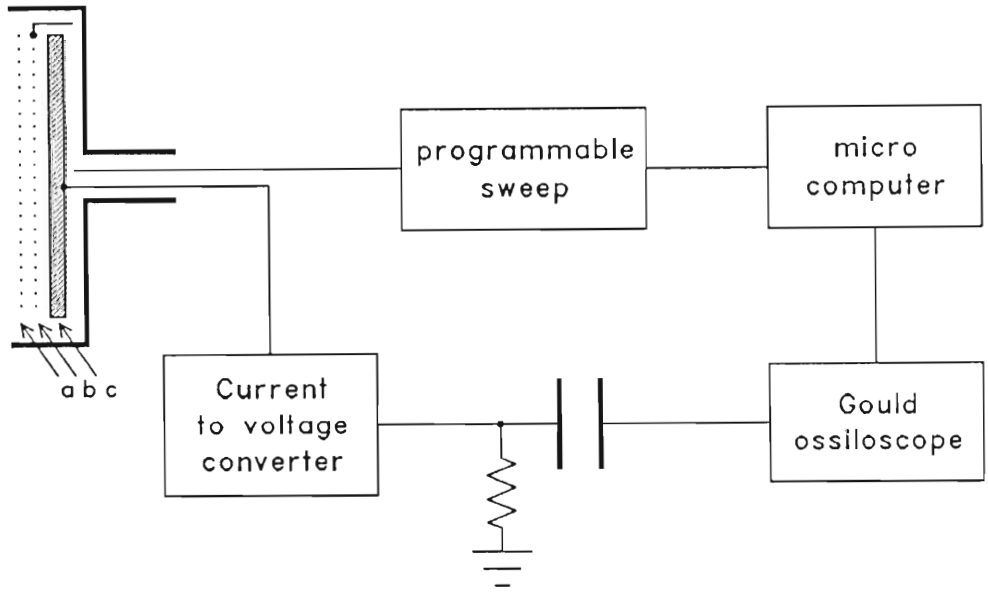

Figure 3.6: The electrostatic energy analyzer circuit. The outer floating grid *a* repels electrons and grid *b* is swept from 0 - 100 V to characterize the energy of the incoming ions. These ions are collected on collector plate *c*.

trace; Figure 3.7 (a). The current density for the rest ions is given by

$$j_R = n_R e \sqrt{\frac{eT_e}{m_i}}$$

and that for the beam ions by

$$j_B = n_B e \sqrt{\frac{2eW_o}{m_i}},$$

where n_R and n_B are respectively the rest and beam ion densities and W_b is the ion beam energy. The density ratio of rest to beam ions is therefore

$$\frac{n_R}{n_B} = \frac{j_R}{j_B} \sqrt{\frac{2W_o}{T_e}}$$

and

$$\alpha = \frac{n_R}{N_o} = \frac{1}{\frac{n_R}{n_B} + 1},$$

where $N_o = n_R + n_B$ is the total ion density.

3.4 Interferometer Traces

A plane wave is launched in the plasma by applying a small sinusoidal signal from a signal generator to the source chamber. Waves propagate from the separator grid and are detected at a distance x downstream with a Langmuir probe. The position of the probe is controlled by a stepping motor. The wave potential can be written as

$$V \propto e^{i(kx - \omega t)}$$

where k is the wave vector and $\omega/2\pi$ the frequency of the wave.

The interferometer consisting of a mixer and a low-pass filter is used to determine the relative amplitude and phase of two signals. The mixer stage multiplies the detected signal with part of the original launch signal from the generator. The output is therefore of the form

$$V = A_1 A_2 e^{i(kx - \omega t)} e^{-i\omega t}$$

where A_1 and A_2 are the amplitudes of the respective signals. Integrating this (low-pass filter) gives for the average signal

$$\begin{aligned} \bar{V} &= \frac{1}{2}A_1A_2\mathrm{Re}[e^{i(kx-\omega t)}(e^{-i\omega t})^*] \\ &= \frac{1}{2}A_1A_2\mathrm{Re}[e^{ikx}]. \end{aligned}$$

(the real part of e^{ikx}).

The position of the probe x is recorded against the interferometer output V (Figure 3.8). Generally k is a complex quantity:

$$k = k_r + ik_i$$

where k_r and k_i are respectively the real and imaginary components of the wave number. Then

$$\begin{aligned} \bar{V} &\propto e^{k_i x}\mathrm{Re}(e^{ik_r x}) \\ &\propto e^{k_i x}\cos k_r x, \end{aligned}$$

From the interferometer trace we can determine k_r from the wavelength and $1/k_i$ from the distance over which the amplitude changes by a factor e. From these values the normalized growth rate k_i/k_r can be calculated. A typical interferometer trace is illustrated in Figure 3.9.

3.5 Wave Front Measurements

Wave front measurements were made by moving a Langmuir probe axially through the plasma and recording the interferometer trace. By repeating this procedure at various radial positions a picture of the spatial development of the wave fronts was obtained by joining regions of equal phase. As the probe had to be rotated to change the radial position, the vertical height y changes with radius as is illustrated in Figure 3.10. The variation in y is neglected as the variation in plasma parameters over this distance is very small.

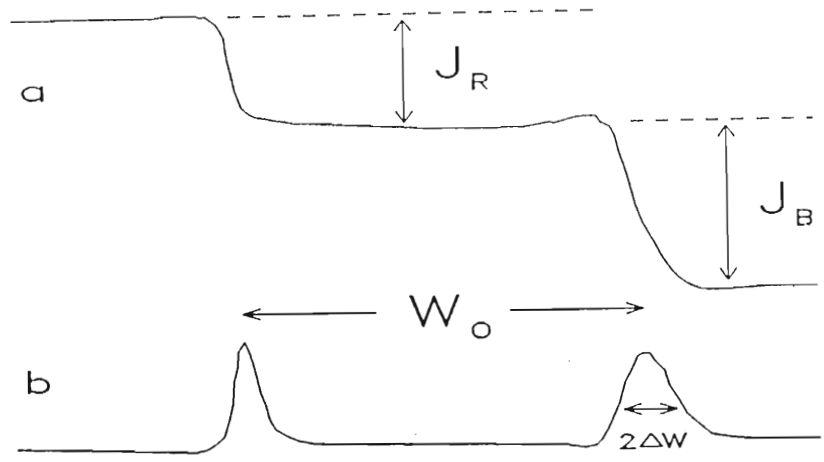

Figure 3.7: Typical output from the analyzer circuit *a* with the rest and beam ion current densities indicated by j_R and j_B. The beam energy W_o corresponds to the separation between the rest and beam ion peaks in the differentiated trace *b*. The beam ion temperature is calculated from the energy half width ΔW of the beam ion peak.

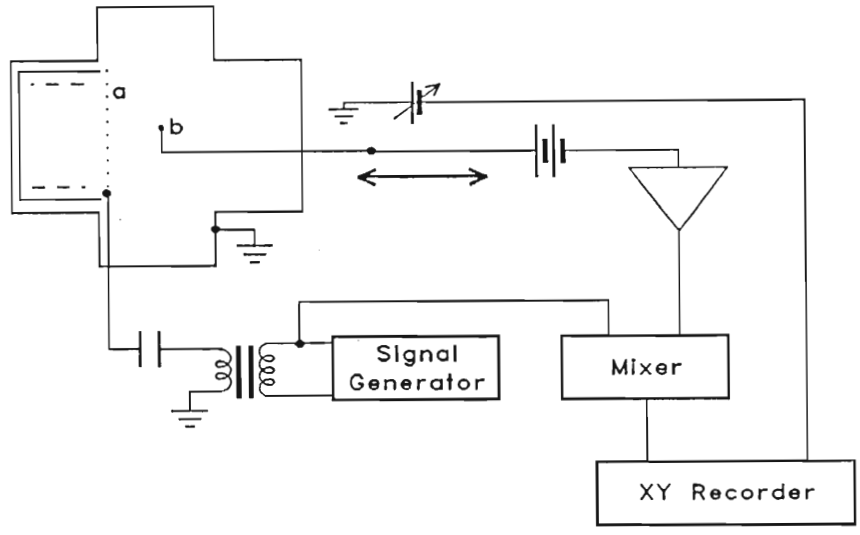

Figure 3.8: The interferometer circuit used to obtain wave form traces. A small sinusoidal signal is injected into the plasma via the separator grid *a* and is multiplied with the amplified signal from a moveable probe in the plasma *b*. This signal is then recorded on an X-Y recorder against the axial position of the probe. The position is determined by a variable voltage source calibrated to indicate axial position.

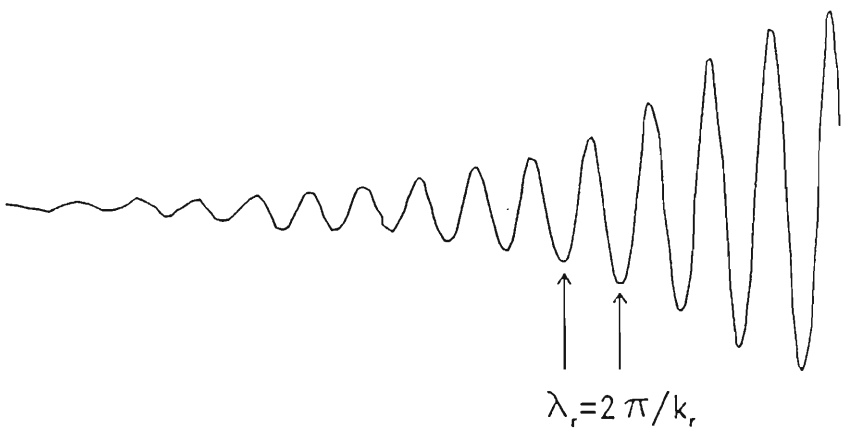

Figure 3.9: A typical growing wave trace from which k_r was calculated from the wavelength and $1/k_i$ from the distance over which the amplitude changes by a factor e.

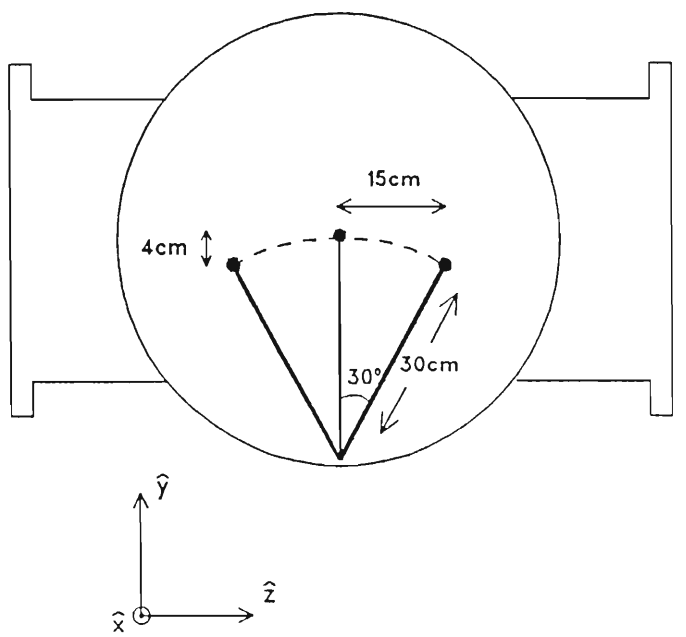

Figure 3.10: An axial cross section of the TP illustrates the radial movement of the Langmuir probe used in wave front measurements. The three probe positions shown corresponds to z = -15, 0 and +15 cm. The rotation of the probe also causes vertical displacement (maximum 4 cm) which is neglected in the wave front construction.

Chapter 4

EXPERIMENTAL OBSERVATIONS

The study of the growth rate dependence of the CFIAI undertaken in this chapter extends the work carried out by HAYZEN [31] on a similar DP device by measuring the growth rate under a wider range of plasma parameters.

The chapter is organized in the following way: A survey of the steady state plasma is carried out in section 4.1 , including radial and axial profiles of T_e, n_e, v_p and also an axial profile of the ion beam density. Measurements of the dispersion relation are presented in section 4.2. In section 4.3 to 4.5 the growth rate is examined as a function of wave number, beam energy and magnetic field respectively. Data on the spatial development of wave fronts are presented in section 4.6. Section 4.7 deals with the effect of varying the magnetic field angle with respect to the ion beam and the dependence of growth rate on the plasma diameter is discussed in section 4.8. Section 4.9 constitutes the main conclusions.

4.1 The Steady State Plasma

The theoretical model for the CFIAI as discussed in Chapter 2 assumes an isotropic ion beam streaming into an infinite homogeneous plasma. There is an external magnetic field present, but no external electric field. An

experimental survey was carried out to determine the validity of these assumptions.

Two large diameter Helmholtz coils provide a uniform magnetic field in the target chamber region — measurements showed no significant variation in magnetic field strength. The magnetic field gradient drift velocity [13] is therefore negligible.

Axial variation of T_e, V_p and n_e

The steady state plasma for the target chamber was mapped out axially and radially by using Langmuir probe diagnostics. This provided the spatial variation of plasma potential, electron temperature and density. Figure 4.1 shows the variation of electron temperature with distance into the plasma. During the steady state measurements the magnetic field was constant at 23 gauss and the beam energy 30 eV. Growth rate measurements were taken over the region 10 – 30 cm. Over this region the electron temperature gradient is negligible. The temperature gradient drift velocity is neglected compared to the beam velocity. Figure 4.2 indicates that the plasma potential does not vary axially and there is therefore no electric field due to potential gradients. In Figure 4.3 the variation in electron density into the plasma is illustrated. The density gradient over the measurement region is negligible, but there is a sharp decrease over the first few centimeters. This distance is too large to be explained by a grid sheath effect. It will be discussed later in this section.

Radial variation of T_e, V_p and n_e

Radial measurements were taken at a distance 30 cm into the plasma. The Langmuir disc probe was fixed to a 30 cm tall stem that could be rotated through an angle of 30° each side of vertical. The probe could therefore scan through 30 cm in the z-direction. At the extreme radial positions the probe tip was 4 cm lower than at the middle position due to the rotation, but the effect of the vertical displacement was neglected. In Figure 4.4 the radial variation of temperature is $\approx$ 17% and is neglected. It should be noted that the discrepancy in the values of T_e in figures 4.1 and 4.4 (for similar values of p, B and W_o) may be due to a difference in the wall conditions. In Figure 4.5 the radial variation in plasma potential is illustrated. There is a radial decrease of potential of $\approx$ 16% over a distance of 15 cm from the centre of the plasma. The radial change in density is illustrated in Figure 4.6. The over all radial variation is $\approx$ 30% over the total region, but it is small over

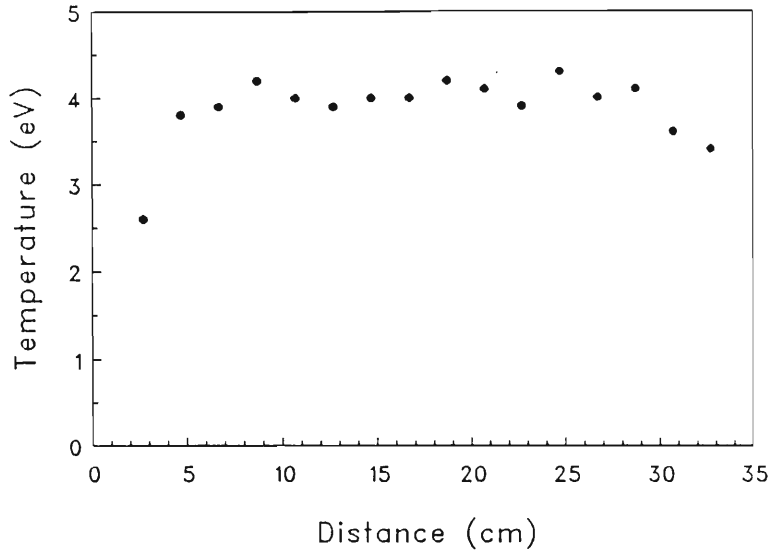

Figure 4.1: The axial variation of electron temperature in the target chamber; $p = 3 \times 10^{-4}$ Torr, $B = 20$ gauss, $W_o = 50$ eV, $y = 0$ cm.

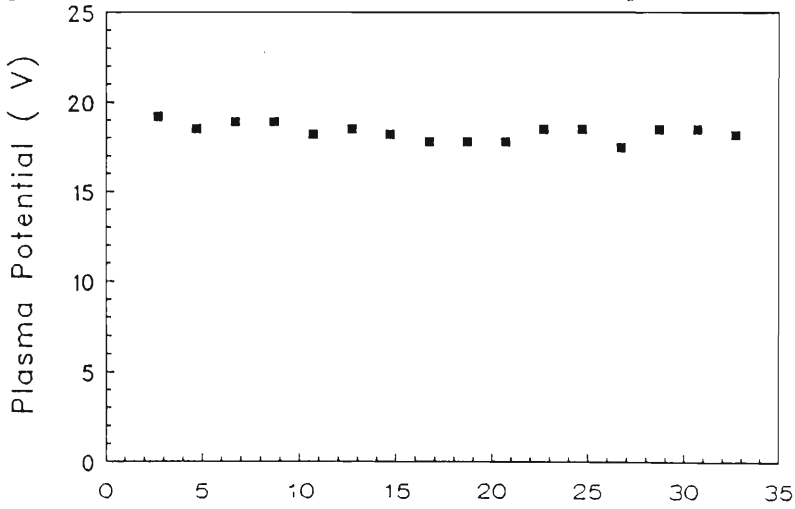

Figure 4.2: The axial variation of plasma potential in the target chamber; $p = 3 \times 10^{-4}$ Torr, $B = 20$ gauss, $W_o = 50$ eV, $y = 0$ cm.

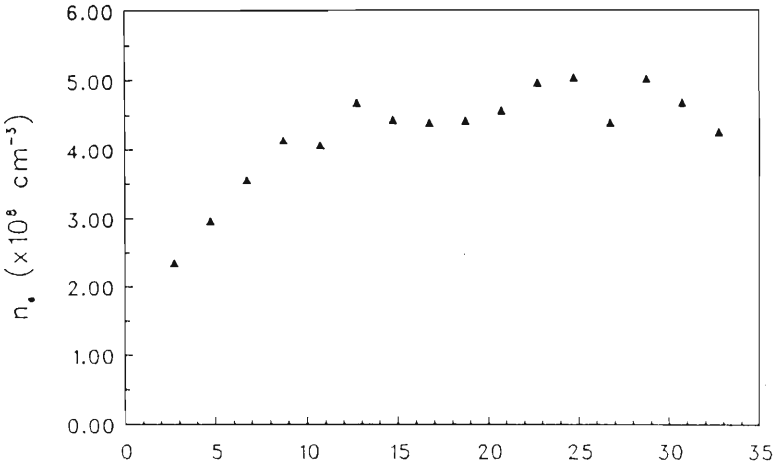

Figure 4.3: The axial variation of electron density in the target chamber; $p = 3 \times 10^{-4}$ Torr, $B = 20$ gauss, $W_o = 50$ eV, $y = 0$ cm.

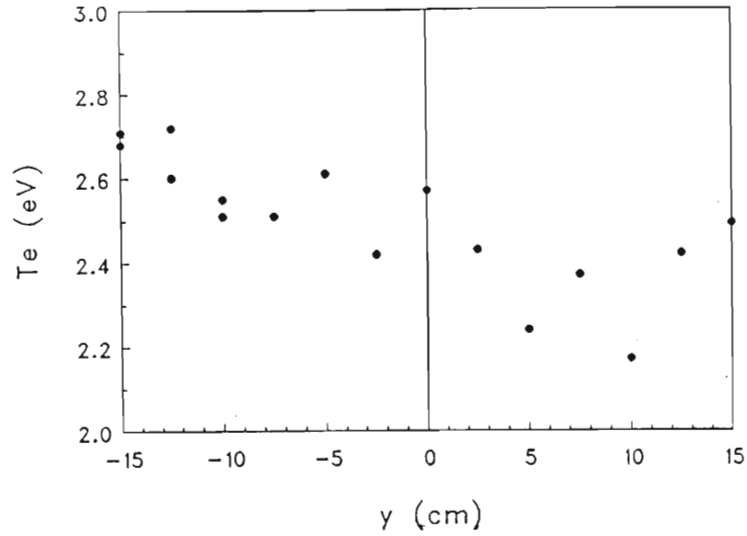

Figure 4.4: The radial variation of electron temperature in the target chamber; $p = 3 \times 10^{-4}$ Torr, $B = 23$ gauss, $W_o = 50$ eV, $x = 32$ cm.

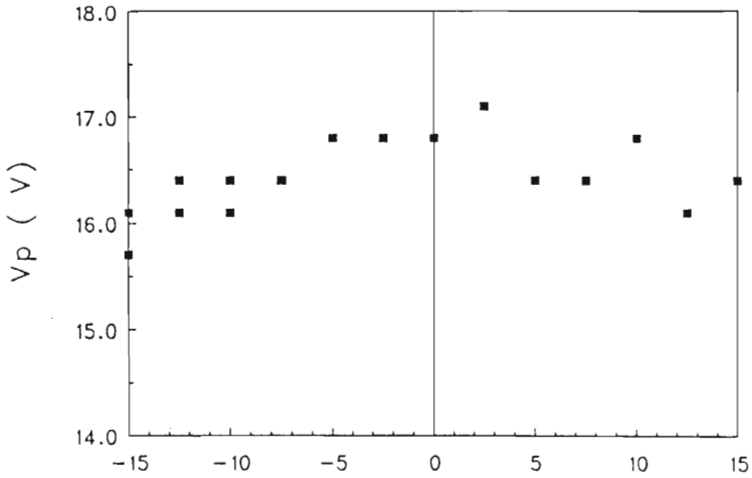

Figure 4.5: The radial variation of plasma potential in the target chamber; $p = 3 \times 10^{-4}$ Torr, $B = 23$ gauss, $W_o = 50$ eV, $x = 32$ cm.

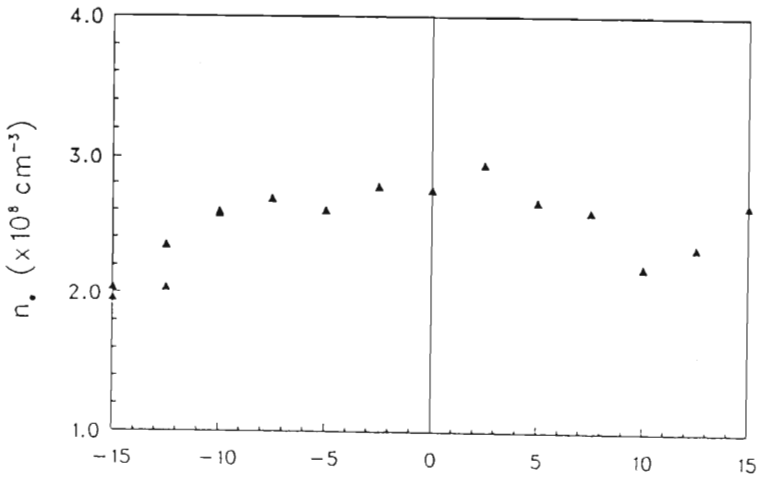

Figure 4.6: The radial variation of plasma density in the target chamber; $p = 3 \times 10^{-4}$ Torr, $B = 23$ gauss, $W_o = 50$ eV, $x = 32$ cm.

the central portion.

Variation of T_e with magnetic field

The electron temperature is found to be dependent on the magnetic field. This is illustrated in Figure 4.7. The temperature increases sharply with magnetic field until it begins to level off at about 20 gauss. The dependence of T_e on magnetic field is not believed to be a probe – effect since orthogonal Langmuir disc probes give equivalent values of T_e. A possible explanation of this effect is the increase in turbulence with magnetic field which can lead to electron heating [36,5].

Variation of T_e with neutral pressure

The electron temperature also depends on the neutral gas pressure – The larger the pressure the lower T_e. See Figure 4.8. The wall conditions of the vacuum chamber also affect T_e. The two sets of data represent measurements of T_e under similar plasma conditions, but at different times. Data taken just after the device had been serviced are indicated by filled – in circles and the open circles are data taken after the machine had been in continuous operation for more than 2 months.

Axial variation of total ion density

An electrostatic energy analyzer was used to measure the axial total ion density distribution. In Figure 4.9 the ion density is displayed at various neutral pressures as a function of distance into the plasma. The values obtained for the ion density from the energy analyzer are much smaller than that for electron density as obtained from the Langmuir probe. Charge neutrality however requires that $N_o = n_e$. The energy analyzer is constructed using two grids of 200 lines per cm and with a 70% transparency. The combined transparency of the grids is unknown and contributes to the lower density value. The energy analyzer is also physically large and tends to modify the local plasma parameters. Although the absolute density measurements of the energy analyzer are inaccurate, its main use is to measure change in density and to determine the ion beam energy. Over approximately the first 6 cm there is a sharp increase in plasma density – Figure 4.9. This decrease is more pronounced for higher values of neutral pressure. Comparing this with Figure 4.3 where the density was measured with a Langmuir probe, a similar behaviour is observed close to the grid. The scale length of the decrease in density near the grid is two orders of magnitude greater than the Debye length, which implies that this decrease is not a sheath effect. It is

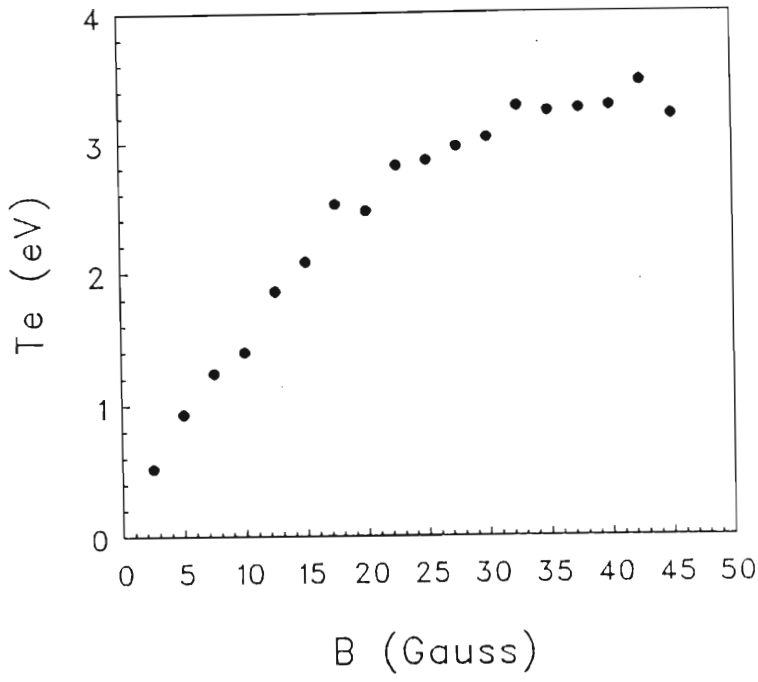

Figure 4.7: The dependence of electron temperature on the magnetic field; $p = 3 \times 10^{-4}$ Torr, $W_o = 50$ eV, $x = 18$ cm.

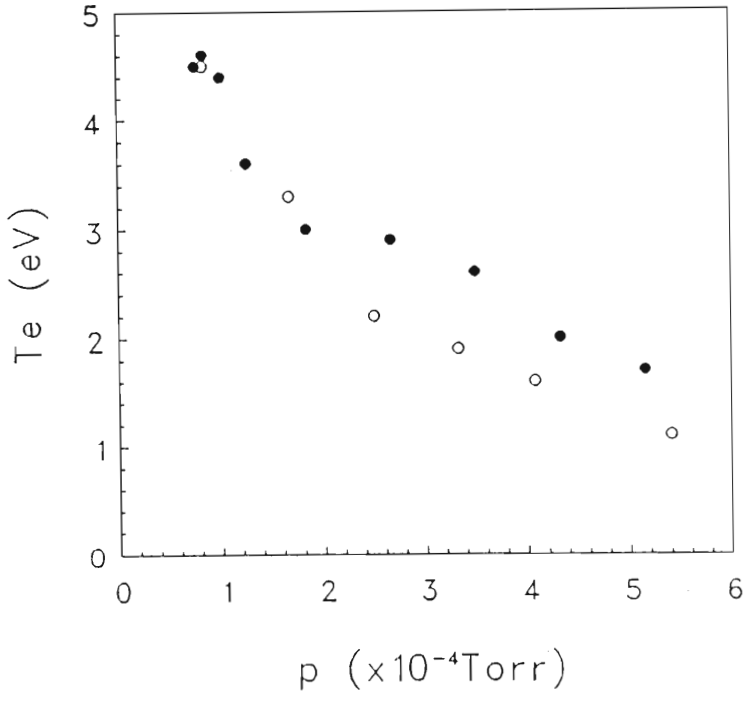

Figure 4.8: The dependence of electron temperature on neutral pressure; $W_o = 50$ eV, $B = 23$ gauss, $n_e = 1.8 \times 10^8$ cm^{-3}, $x = 18$ cm. The two data sets correspond to different plasma chamber wall conditions; the filled–in and open circles correspond respectively to clean and dirty wall conditions.

explained in terms of the construction of the target chamber: The distance between the separator grid (at 0 cm) and the first filaments corresponds to the depleted region. As the electrons are closely tied to the magnetic field lines, their axial diffusion will be restrained. The plasma is formed by these electrons neutralizing some beam ions, and few electrons close to the grid will result in a lower plasma density. The bunching of electrons from the filaments by the magnetic field is also evident from the data at the neutral pressure of 0.83×10^{-4} Torr. A sinusoidal variation in density is observed. The period of the oscillation is comparable to the distance between the filaments. This effect is not apparent at higher pressures, because of increased collisions. The typical operating pressure for the growth rate measurements is 2.5×10^{-4} Torr and over the region of measurement (10 – 30 cm) the density gradient is negligible. At high values of the neutral pressure the density gradient becomes significant and has to be taken into account.

Axial variation of beam ion density

In Figure 4.10 the variation of ion beam density is plotted against distance into the plasma. It should be noted that the plasma density was kept approximately constant as the neutral pressure was changed in order to obtain the different sets of data. The lower values for the 2.5×10^{-4} Torr curve are due to insufficient density compensation. The ion beam density decreases in an exponential fashion with distance into the plasma. This was also observed by D'Angelo [19] who identified charge exchange collisions and scattering of the ions from the beam by ion acoustic turbulence as the mechanisms which reduce the ion beam density. He identified the charge exchange process to be dominant over the first 30 cm of the plasma. As the present plasma parameters are very similar to those with which D'Angelo operated, it is assumed that charge exchange is the main mechanism causing the decrease. The distance over which the ion beam intensity drops by a factor e is plotted as a function of neutral pressure in Figure 4.11. These data (filled–in circles) are compared to those of D'Angelo (open circles). There is reasonably good agreement between the data sets. The slope of the solid curve corresponds to a charge exchange cross–section of $\approx 5 \times 10^{-15}$ cm^2 which agrees with data of the A^+ ion collision cross–section [19]. This evidence therefore suggest that the ion beam attenuation is caused by charge exchange collisions.

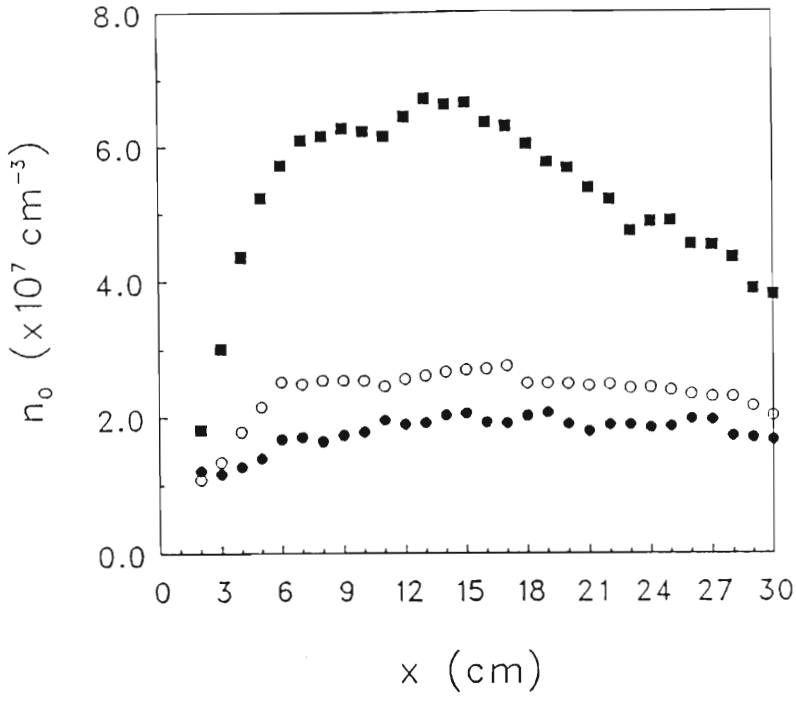

Figure 4.9: The axial variation of total ion density N_o in the target chamber; $W_o = 30$ eV, $B = 23$ gauss, $n_e = 1.8 \times 10^8$ cm^{-3}. Background pressures are represented by: ● 0.83×10^{-4} Torr, ○ 2.5×10^{-4} Torr and ■ 5.8×10^{-4} Torr.

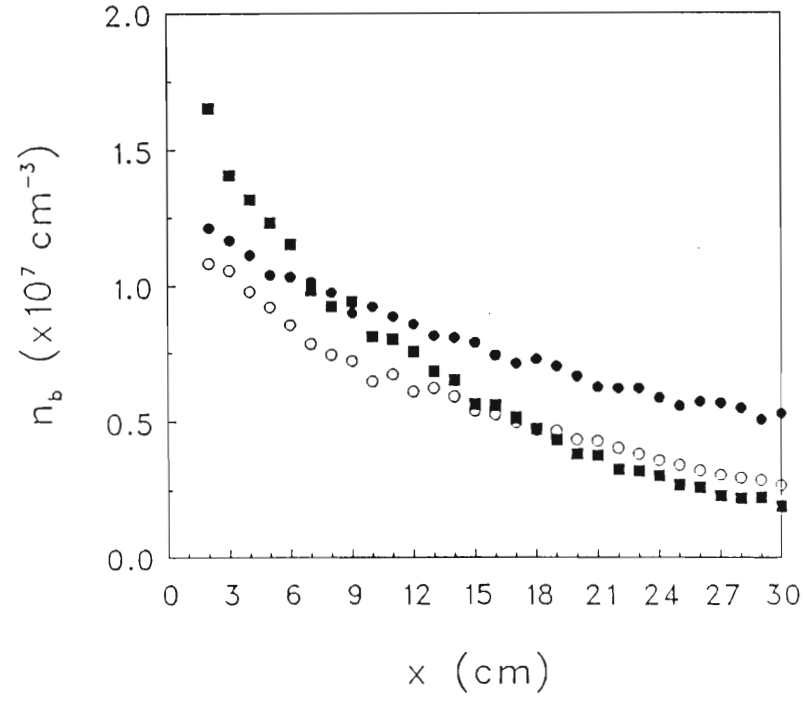

Figure 4.10: The axial variation of ion beam density in the target chamber; $W_o = 30$ eV, $B = 23$ gauss, $n_e = 1.8 \times 10^8$ cm^{-3}. Background pressures are represented by: ● 0.83×10^{-4} Torr, ○ 2.5×10^{-4} Torr and ■ 5.8×10^{-4} Torr.

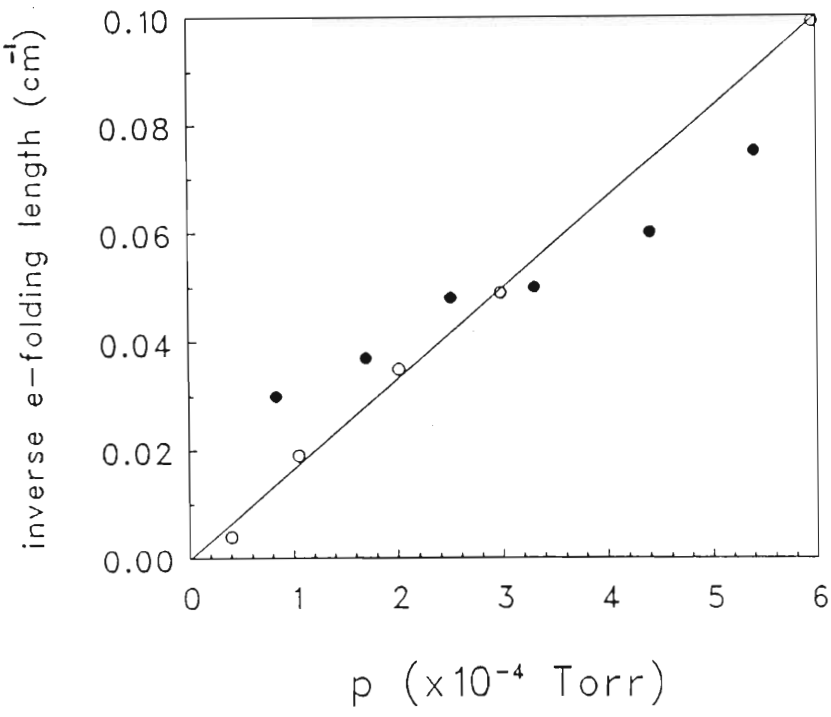

Figure 4.11: The inverse e-folding length of beam density N_o versus neutral pressure; $W_o = 30$ eV, $B = 23$ gauss, $n_e = 1.8 \times 10^8$ cm^{-3}. The data from the present experimental device (•) are compared to those of D'Angelo (○), who used a similar device with similar plasma parameters.

4.2 The Dispersion Relation

The mode of the instability that is observed experimentally is identified by the dispersion relation in Figure 4.12 as the CFIAI propagating at the slow mode of the beam. The measured phase velocity (filled–in circles) is less than the beam velocity, but larger than the approximate phase velocity of the slow mode, $V_o - C_s$. This is explained by taking the background ions into account, which results in the larger phase velocity, $V_o - \sqrt{\alpha}C_s$, where $\alpha = n_b/N_o$; see chapter 2, section 2.2.1. This relation is further verified by plotting $V_o - \omega/k$ against $\sqrt{\alpha}T_e$. This is illustrated in Figure 4.13. The independent variable is T_e and this was varied experimentally by changing the neutral pressure (see Figure 4.8). The solid line corresponds to the gradient predicted from theory: $\sqrt{e/m_i}$, as $C_s = \sqrt{eT_e/m_i}$. There is therefore reasonable agreement between the approximate dispersion relation and the data, bearing in mind that the ordinate represents the small difference between two large quantities.

4.3 Growth Rate as a Function of the Wave Number

The dependence of growth rate (k_i/k_r) on wave number is illustrated in Figure 4.14. The wave number is normalized with respect to the Larmour radius. As $k_r\rho_e$ approaches 1 the electrons become effectively unmagnetized and the growth rate decreases accordingly (see section 2.3). This condition can also be written as

$$\rho_e > \lambda/2,$$

i.e. for large values of k_r the electron Larmour radius becomes of the same order as the distance between a wave crest and peak $(\lambda/2)$. The electrons can then participate in the wave motion without having to move along the field lines and this leads to a reduction in growth rate. The experimental data verify this cut off value of $k_r\rho_e$. In Figure 4.14 theory is compared with experimental data. The solid line corresponds to the complete theoretical model (see equation 2.38) with $k_\parallel/k_\perp$ as the only fitted parameter.

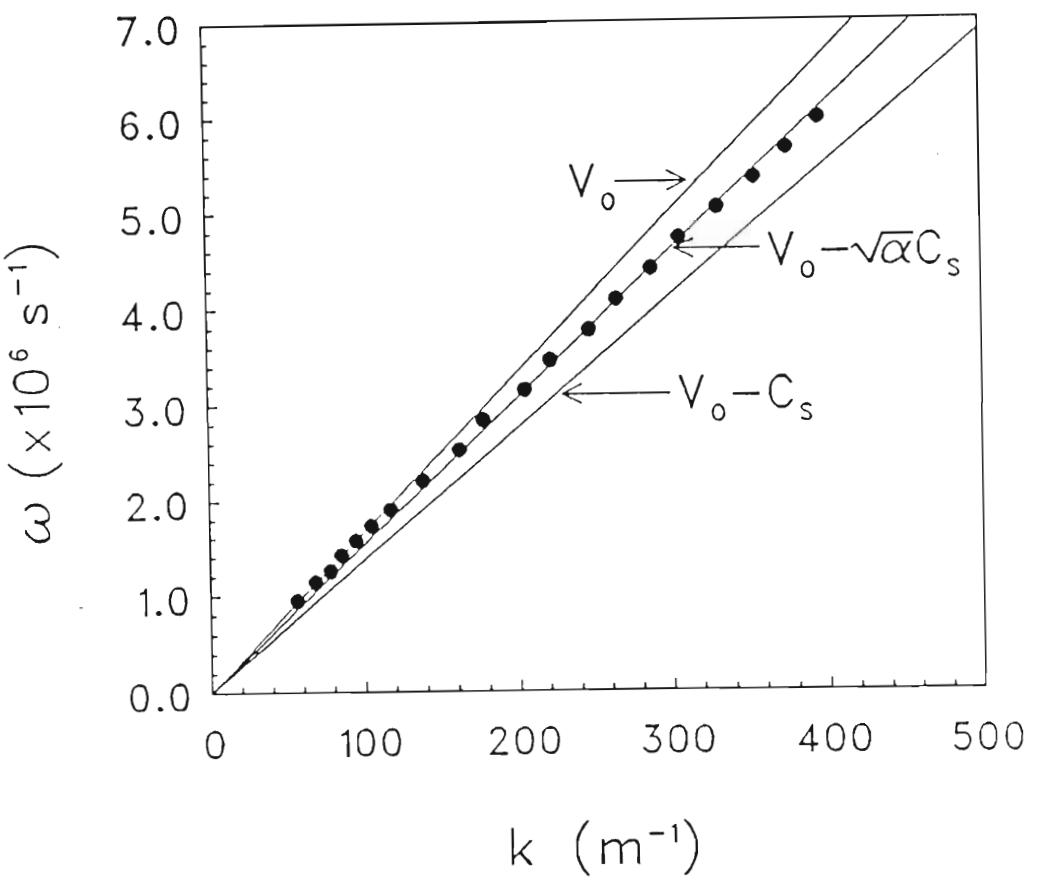

Figure 4.12: The dispersion relation. The phase velocity is given by $V_o - \alpha^{-1/2} C_s$ where $\alpha = n_b/n_e$; $W_o = 58$ eV, $T_e = 3.0$ eV, $T_{ib} = 0.044$ eV, $T_{io} = 1.8$ eV, $B = 23$ gauss, $n_e = 5 \times 10^8$ cm^{-3}, $x = 18$ cm.

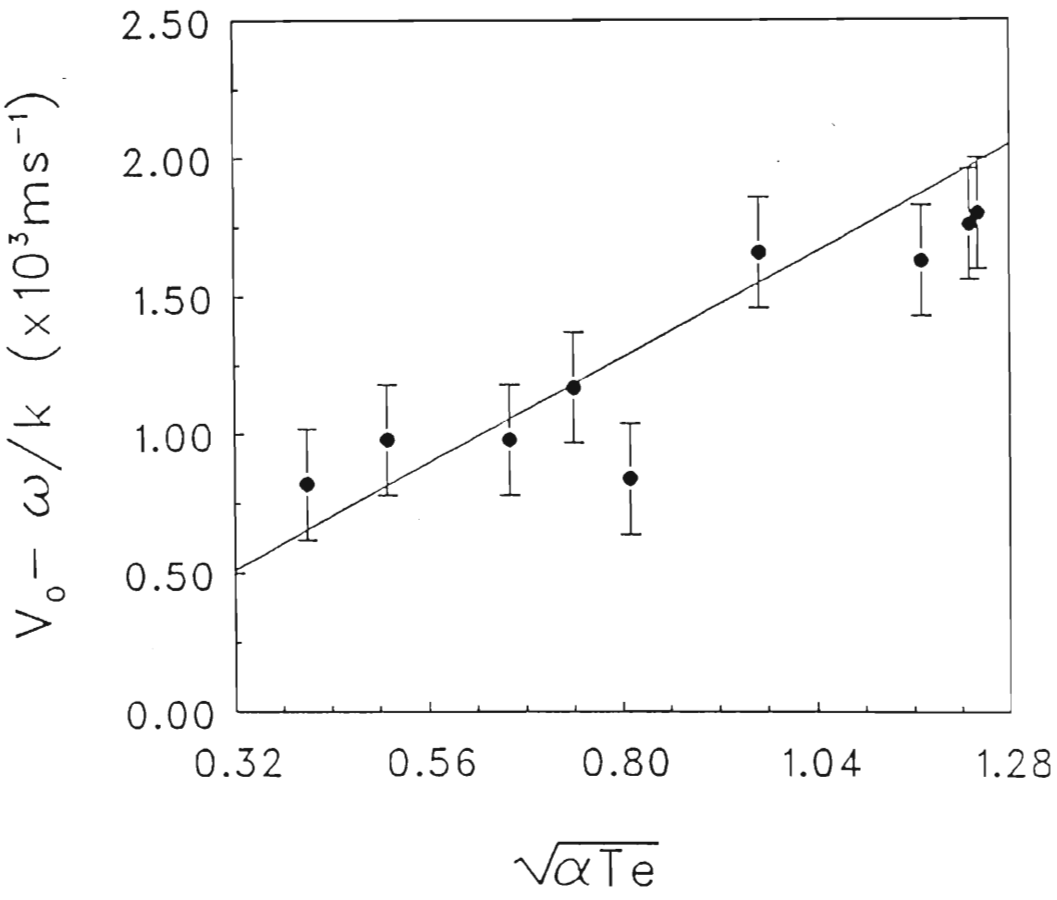

Figure 4.13: Graph of $V_o - \omega/k$ versus $(\alpha T_e)^{-1/2}$. The temperature was varied by changing the neutral pressure; $W_o = 54$ eV, $B = 23$ gauss, $n_e = 1.8 \times 10^8$ cm^{-3}, $x = 18$ cm. The solid line represents the approximate theoretical model predicting a linear relation with a gradient $(e/m_i)^{1/2}$.

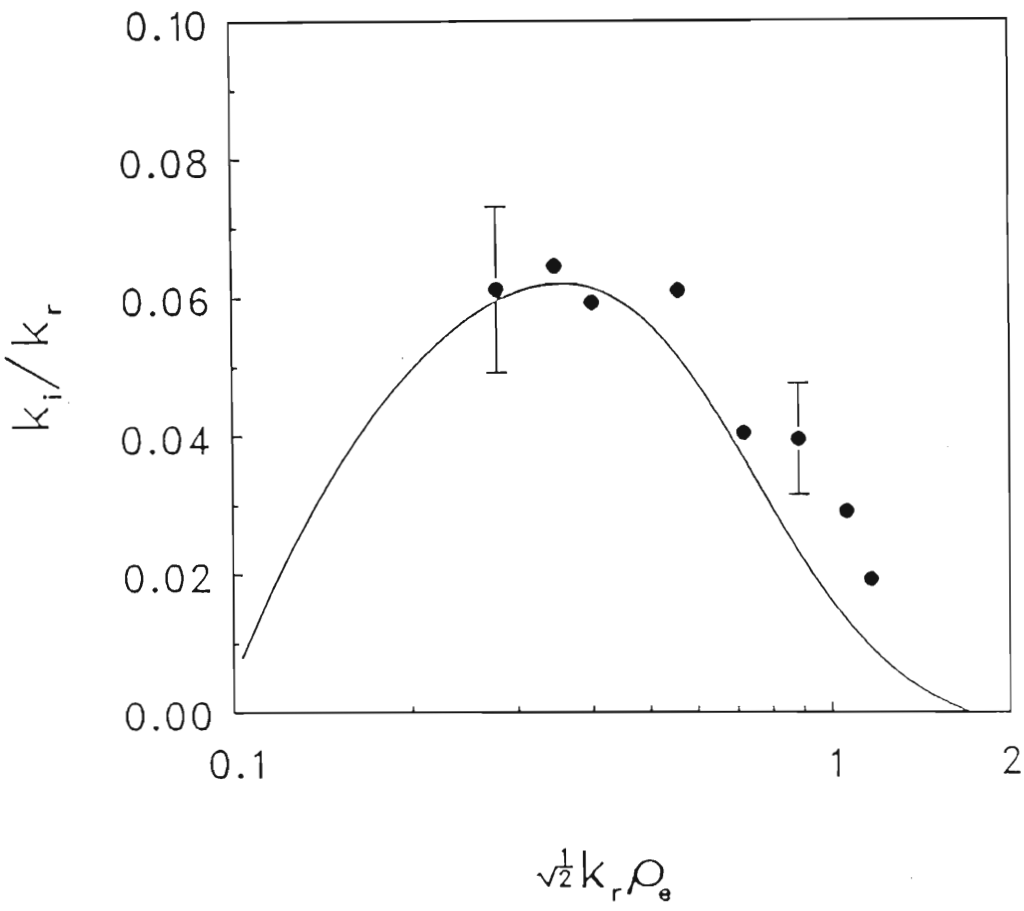

Figure 4.14: Growth rate vs normalized wave number. $k_\parallel/k_\perp = 0.015$, $W_o = 30$ eV, $B = 23$ gauss, $n_e = 1.8 \times 10^8$ cm^{-3}, $x = 18$ cm, $T_e = 2.7$ eV, $T_e/T_{ib} = 60$, $T_{io} = 1.5$ eV, $\lambda_{ci} = 23$ cm, $\lambda_{ci}/\lambda_{ce} = 0.009$. The solid line is obtained by using the full theoretical model with $k_\parallel/k_\perp$ as a fitted parameter.

4.4 Growth Rate as a Function of Beam Energy

It was explained in section 2.3 that the growth rate of the CFIAI depends mainly on the negative gradient of the electron distribution function at the phase velocity of the wave. Referring to sections 2.3 and 2.4.3 it is noted that if $\omega/k > C_e'$ (where C_e' is the projection of the electron thermal velocity onto the direction of wave propagation), a reduction in ω/k gives a larger magnitude of $\partial f_e/\partial v_{\|}$ and therefore a larger growth rate. The opposite applies when $\omega/k < C_e'$, as in the case of the low beam velocities in Figure 4.15. Here the normalized growth rate is plotted against normalized beam velocity, V_o/C_s. The solid line is the theoretical fit to the experimental data. There is a cut-off beam velocity at $V_o \approx 2.5C_s$ below which the instability damps sharply. As the beam ion temperature T_{ib} increases for decreasing beam velocity, the ion-ion instability is not observed for low values of V_o; see section 2.4.5.

4.5 Growth Rate as a Function of Magnetic Field.

As explained in section 2.3 the growth rate depends strongly on the magnetic field. In Figure 4.16 the normalized growth rate is plotted against $2(k_r\rho_e)^{-2}$. The filled-in circles corresponds to $B = 14$ gauss and the open circles to $B = 10$ gauss. The solid and dashed lines are the theoretical fits to these data respectively. There is little difference between the two cases for $2(k_r\rho_e)^{-2} \leq 2$, i.e. when $\lambda/2 \leq \rho_e$.

In Figure 4.17 the magnetic field is varied while the wave number is held constant. The open circles correspond to data taken at $k_r = 160$ m^{-1} The magnetic field was varied between 5 and 30 gauss. The variation in electron temperature was taken into account in the calculation of the theoretical fit. (See Figure 4.7).

4.6 Wave Front Measurements

Wave front measurements were made by moving a Langmuir probe axially through the plasma and recording the interferometer traces; (see sec-

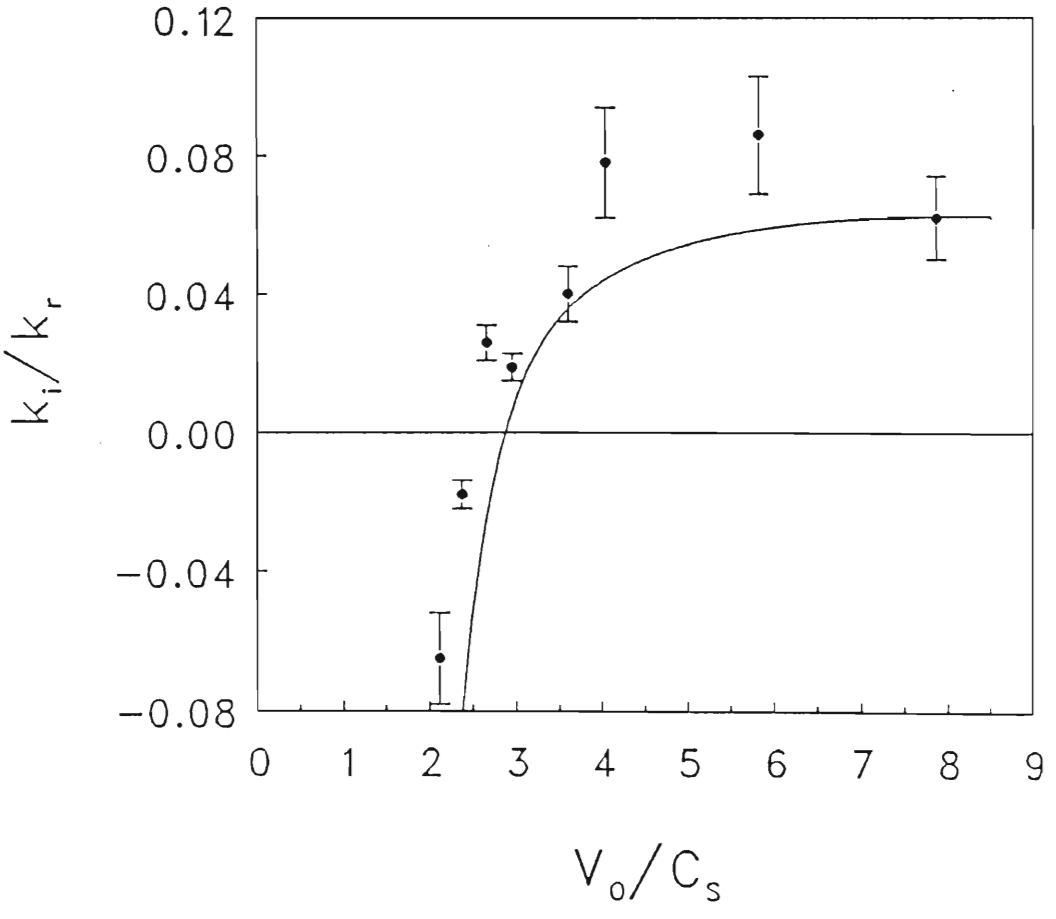

Figure 4.15: Normalized growth rate vs normalized beam velocity. $k_\parallel/k_\perp = 0.015$, $B = 23$ gauss, $n_e = 1.8 \times 10^8$ cm^{-3}, $x = 18$ cm, $T_e = 2.7$ eV, $T_e/T_{ib} = 60$, $T_{io} = 1.5$ eV, $\lambda_{ci} = 23$ cm, $\lambda_{ci}/\lambda_{ce} = 0.009$. The solid curve is obtained by using the full theoretical model with $k_\parallel/k_\perp$ the only fitted parameter.

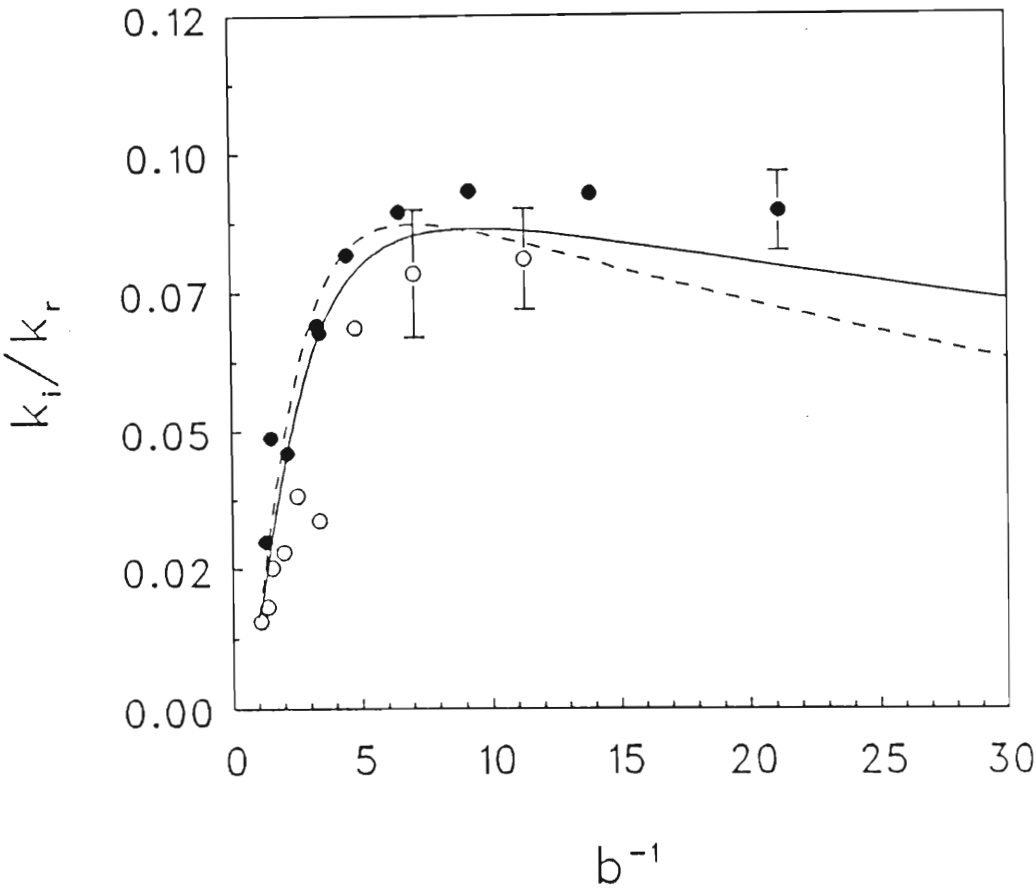

Figure 4.16: Normalized growth rate versus $b^{-1} = 2(k_r\rho_e)^{-2}$ at ● $B = 14$ gauss and ○ $B = 10$ gauss. With: $k_\parallel/k_\perp = 0.015$, $W_o = 48.8$ eV, $n_e = 1.8 \times 10^8$ cm^{-3}, $x = 25$ cm, $T_e = 2.7$ eV, $T_e/T_{ib} = 60$, $T_{io} = 1.4$ eV, $\lambda_{ci} = 30$ cm, $\lambda_{ci}/\lambda_{ce} = 0.012$ and at $B = 10$ gauss $T_e = 1.86$ eV. The curves are obtained by using the full theoretical model with $k_\parallel/k_\perp$ the only fitted parameter

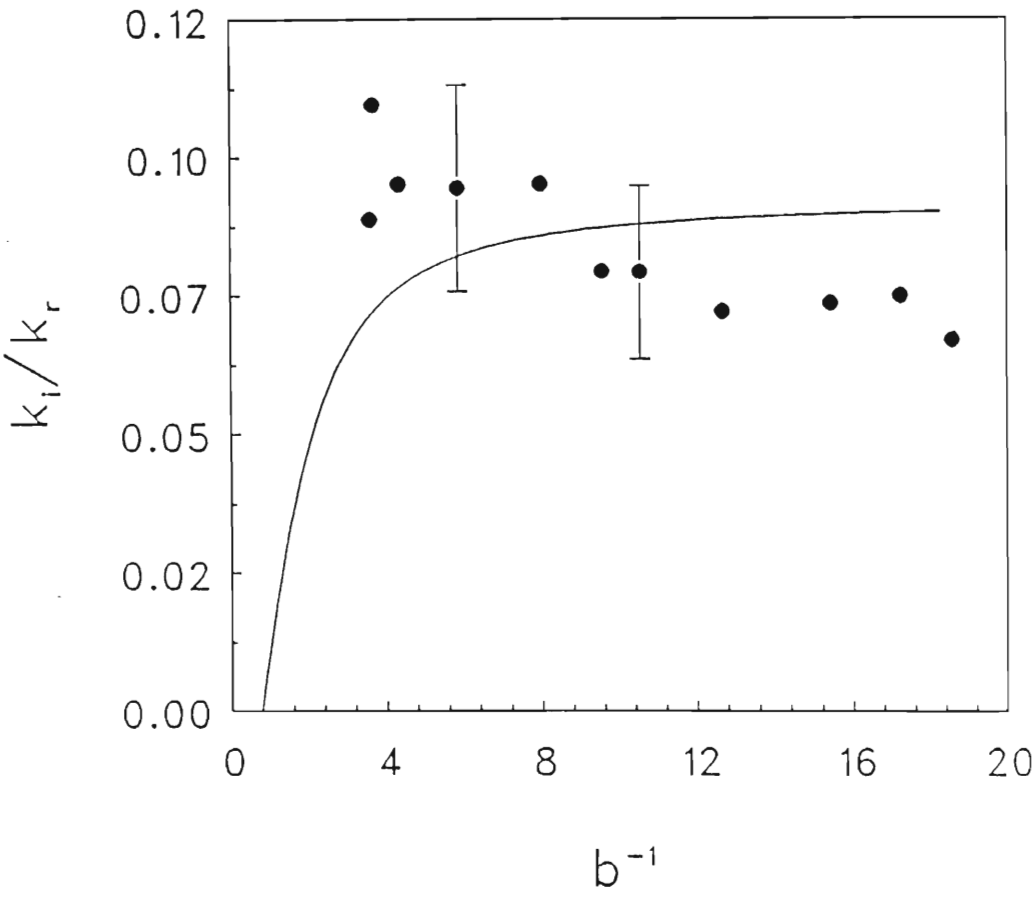

Figure 4.17: Normalized growth rate versus $b^{-1} = 2(k_r\rho_e)^{-2}$ with the magnetic field varying. The wave number is constant at $k_r = 1.6$ cm. $k_\parallel/k_\perp = 0.012$, $W_o = 30$ eV, $n_e = 1.8 \times 10^8$ cm^{-3}, $x = 18$ cm, $T_e/T_{ib} = 60$, $T_{io} = 1.4$ eV, $\lambda_{ci} = 30$ cm, $\lambda_{ci}/\lambda_{ce} = 0.012$. The solid curve is obtained by using the full theoretical model with $k_\parallel/k_\perp$ the fitted parameter and including the variation of T_e with B ($T_e = 2.4$ eV at $B = 30$ gauss).

tion 3.5). By repeating this procedure at various radial positions a picture of the spatial development of the wave fronts is obtained. As the probe had to be rotated to change the radial position, the vertical height y changes. Figures 4.5, 4.4 and 4.6 indicate that the radial change in plasma parameters is small and the effect of the vertical variation can therefore be neglected. Typical raw data are displayed in Figure 4.18. Wave traces were taken at radial positions $z = -15, -7.5, 0, +7.5$ and $+15$ cm. The magnetic field angle θ was fixed at 0°, as estimated from the symmetry of the wave fronts about the beam direction; see Chapter 3.

A fundamental assumption made by HAYZEN [31,33] is that the wave fronts are not affected by the variation of θ. To test this assumption wave front plots were obtained at three different values of θ as illustrated in Figure 4.19. It is clear from these results that the wave fronts are indeed affected by changes in θ. The wave fronts are not plain, but are bi-directional (with the direction of k slightly different on each side of the axis and denoted by k_L and k_R) with the central region lagging in phase. The direction of wave propagation is taken as the average direction of the two uni-directional wave fronts, k_L and k_R. The angle between the resultant $\mathbf{k}$ vector and $\mathbf{x}$ is defined in section 2.4.7 as θ_k. When the magnetic field direction is changed the direction of $\mathbf{k}$ also changes so that θ_k is always $\approx \theta/2$. Furthermore $\mathbf{B}$ and k rotates in the same direction. It is noted that $\theta = 0$ when $\mathbf{B} \parallel \hat{\mathbf{z}}$ and $\mathbf{k} \parallel \mathbf{V_o} \parallel \hat{\mathbf{x}}$. This corresponds to the central region of lower growth observed in Figure 4.22.

In the theoretical model, the maximum parallel wavelength in the case of uni-directional wave fronts is assumed to be $\lambda_\parallel = 2D$. In the case for bi-directional wave fronts the following condition is required for electrons to move from a wave crest to a wave trough,

$$\frac{\mid \theta - \theta_k \mid D}{2} = \frac{k_\parallel / k_\perp \; D}{2} \geq \frac{\lambda}{2}.$$

This is illustrated in Figure 4.21. It follows that $\lambda_\parallel \leq D$ if bi-directional wavefronts are limited by the plasma width D.

Another implicit assumption of the theoretical model is that the propagation direction of the wave $(k_\perp / k_\parallel)$ is independent of the axial distance into the plasma. In Figure 4.20 the axial variation of $k_\parallel / k_\perp$ is displayed at various plasma width D. The axial distance is displayed in units of half wave length measured from the point $x \approx 18$ cm.

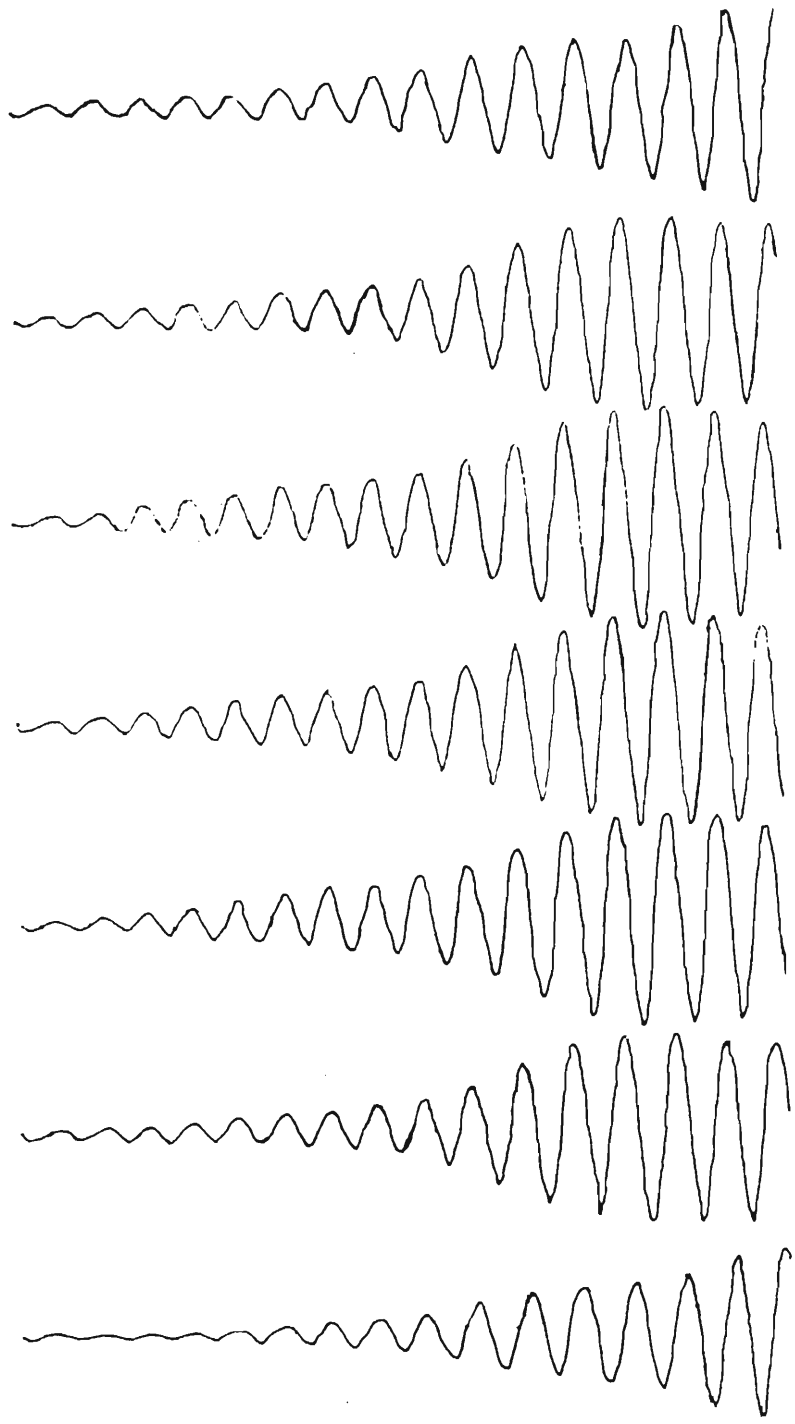

Figure 4.18: Typical raw data used to calculate wave fronts. Interferometer traces are taken at different radial positions and regions of equal phase are joined. The traces from the top to the bottom correspond to radial position $z = +15, +10, +5, 0, -5, -10$, and -15 cm. Here $\theta = 0°$

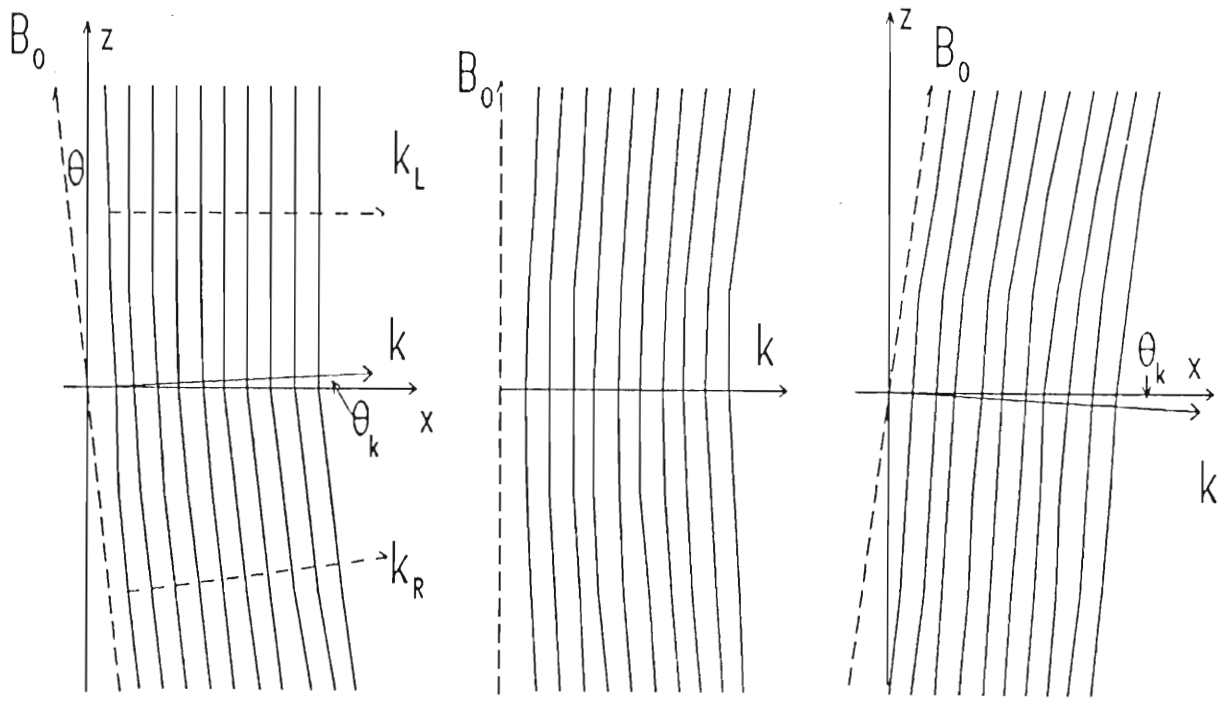

Figure 4.19: Wave fronts at θ = -4, 0 and 5°. θ_k is defined as the angle between $\mathbf{k}$ and $\hat{\mathbf{x}}$ and θ is the angle between $\mathbf{B}$ and $\hat{z}$. The wave fronts to the left and right are labeled by k_l and k_r respectively.

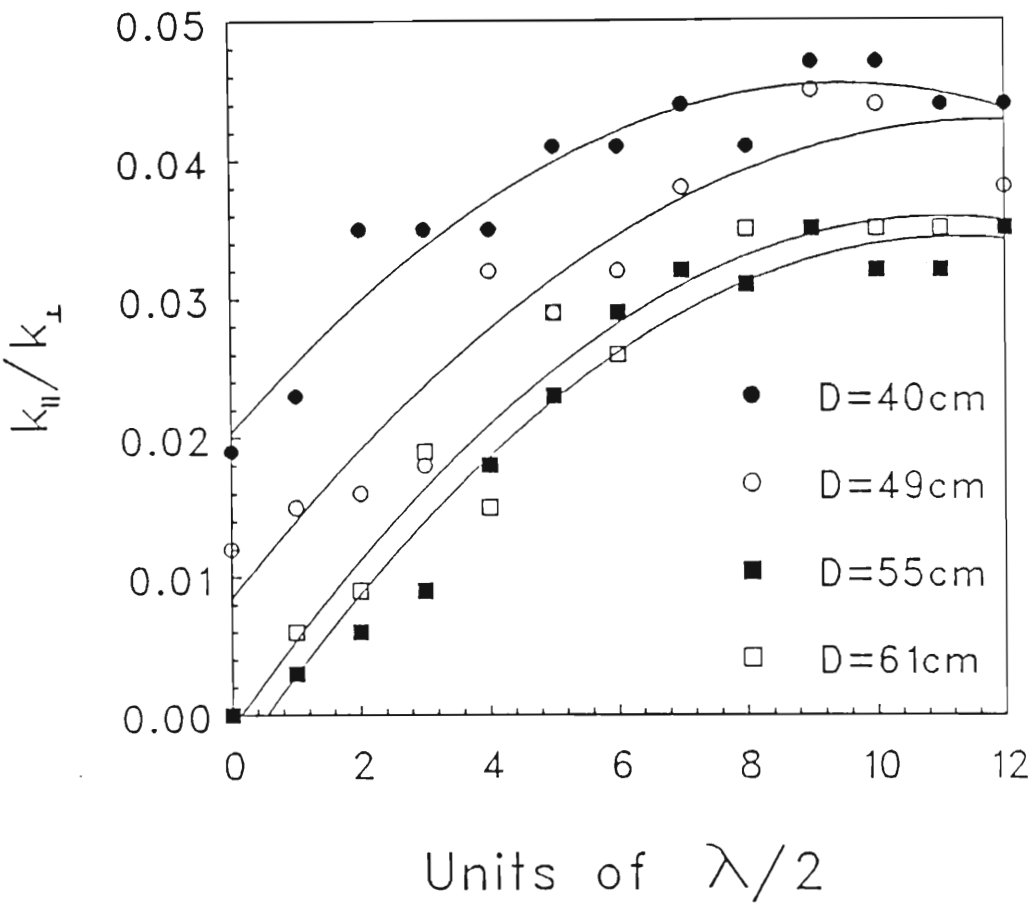

Figure 4.20: Experimental data displaying the axial variation (measured in units of half wave length starting from $x = 18$ cm) of $k_\perp/k_\parallel$ at various values of D, with: $W_o = 35$ eV, $n_e = 1.8 \times 10^8$ cm^{-3}, $T_e = 2.7$ eV, $T_e/T_{ib} = 60$, $B = 23$ gauss and $\lambda_{ci}/\lambda_{ce} = 0.012$. Note that the solid lines are best fit curves to the data and are not obtained by using the theoretical model.

The solid curves in the diagram are the best fit polynomials to the data at various values of D. It is evident from the diagram that $k_\perp/k_\parallel$ increases with distance into the plasma, which is not accounted for by the theory.

At small values of x the wave fronts are found to be approximately plane and parallel to the grid; the growth rate is then negligible, as one would expect from the fact that there are no resonant electrons. As x increases, the wave fronts become increasingly oblique to the plane of the grid, thus allowing ω/k to approach C_e', the condition for maximum growth rate. The oblique angle, $k_\parallel/k_\perp$, remains approximately constant over the larger values of x. This behaviour is found for all four sets of data in Figure 4.20. Furthermore, it is found that in the region of large x, the quantity $\theta_k D$ corresponding to each of the four values of D, is constant ($\theta_k D = 1.7 \pm 0.1$, 1.9 ± 0.3, 1.8 ± 0.2 and 2.0 ± 0.3 cm are calculated by taking the average value of θ_k over the last 6 half wave lengths at $D = 40$, 49, 55 and 61 cm) As the wave fronts therefore propagate through the plasma, the angle of curvature increases until $\theta_k D/2 \approx \lambda/2$.

4.7 Growth Rate as a Function of Magnetic Field Angle.

In this section the experimental data are compared to the theoretical results in section 2.4.7 for the growth rate dependence on magnetic field angle θ.

By rotating the Helmholtz coils about the vertical axis of the experimental device, the direction of magnetic field relative to the ion beam direction was changed. The angle θ (in degrees) is defined as the angle between the magnetic field direction and $\hat{\mathbf{z}}$. As the exact ion beam direction was not known experimentally, the value of $\theta = 0$ was taken to correspond to the symmetry axis displayed in all the growth rate data.

With the plasma width fixed at $D = 50$ cm, growth rate data were obtained for a fixed wave number $k_r = 3.0$ cm^{-1} with the magnetic field angle varying from +8 to -8 degrees; see Figure 4.22. As there is a large scatter in the data, a best fit curve (not theoretical) is used to illustrate the overall growth rate behaviour. The main feature to note is a small dip at $\theta \approx 0°$; The assumption is made that $k_\parallel/k_\perp = 0.015$, in accordance with values in Figure 4.20 at small

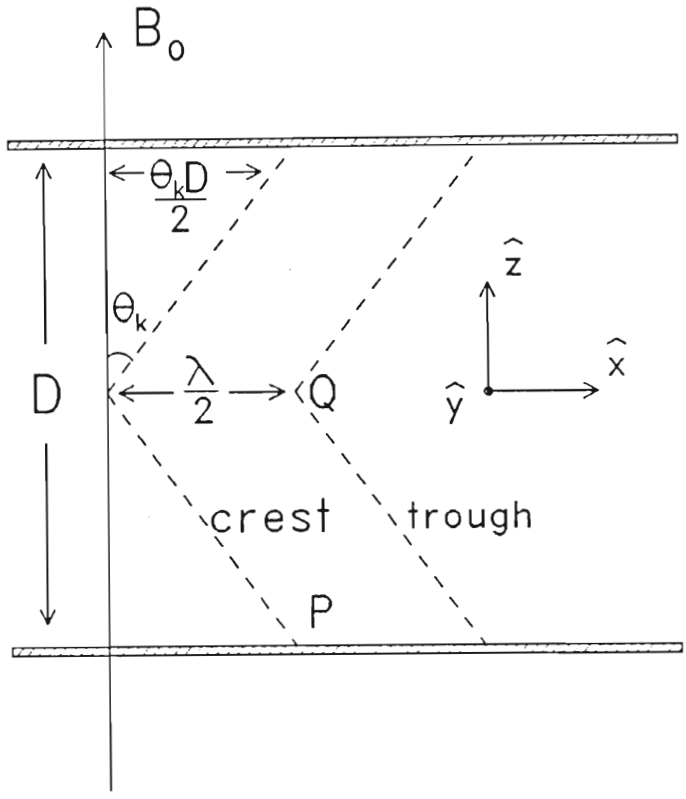

Figure 4.21: A diagram of two wave fronts (crest and trough) in the target chamber. Two plates limit the plasma width to D. The distance between the wave crest and trough is $\lambda/2$. As θ_k is a very small angle one wave front will span an axial distance of $\theta_k D/2$ (limited by the side plates). Electrons can move from region P (crest) to region Q (trough) if $\theta_k D/2 \geq \lambda/2$, where λ is typically 2 cm.

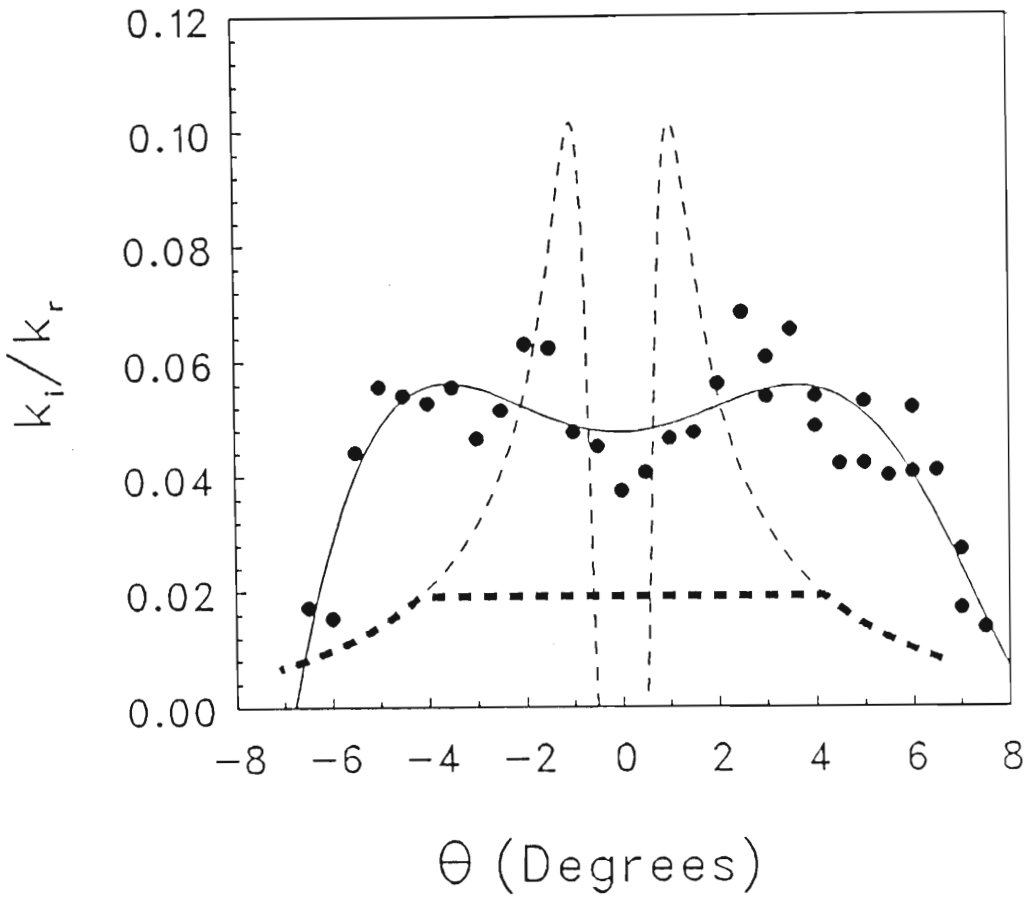

Figure 4.22: Normalized growth rate versus magnetic field angle θ at $D = 50$ cm and $k_r = 3.0$ cm^{-1}. The solid line (not theoretical) represents the best fit to the data. The bold-dashed line is a theoretical fit to the data with $k_\parallel/k_\perp = 0.015$ and assuming $\lambda_\parallel \leq D$. The thin-dashed line corresponds to the infinite plasma case. The measured plasma parameters are $W_o = 35$ eV, $n_e = 1.8 \times 10^8$ cm^{-3}, $T_e = 2.6$ eV, $B = 23$ gauss.

x. This implies that the parallel wavelength is $\lambda_{\|} = 140\,\mathrm{cm}$, which is larger than D (this is the appropriate condition to use as bi-directional wave fronts are observed). The bold-dashed curve in Figure 4.22 is a theoretical fit to the data with $D = 50\,\mathrm{cm}$ including the limit on parallel wave length $\lambda_{\|} \leq D$ and the experimentally observed change in θ_k as θ is varied (section 4.6); it does not contain the dip in growth rate at $\theta \approx 0$ and underestimates the angular width and magnitude of the growth rate data. The thin-dashed curve corresponds to the theory for an infinite plasma and shows the absence of growth at $\theta \approx 0°$.

These results may be explained by taking the wave fronts into account. Since $k_{\|}/k_{\perp} \approx 0.015$ at the middle of the growth rate region, the condition $\theta_k D/2 \geq \lambda/2$ is not satisfied and the electrons will not be able to move easily from crest to trough in order to sustain the wave for $\theta \approx 0$. The growth rate in this region should therefore be small as in the infinite plasma case. A possible explanation for observing only a small dip in growth rate is the diffusion of electrons across magnetic field lines. It is also not clear why the experimental curve is much wider than the theoretical curve - this may be related to the bi-directionality of the wave fronts.

4.8 Variation of Growth Rate with Plasma Width.

In working with a similar DP device, HAYZEN [31,33] found that the growth rate was limited by the parallel dimension of the plasma, which he took to be the fixed distance between the two banks of filaments in the target chamber. He concluded that the maximum parallel wavelength (and therefore also the growth rate) was limited by this fixed parallel dimension. In the current experiment the parallel dimension of the experimental device can be varied.

The most direct measurement of the dependence of the growth rate on plasma width was carried out with θ and k_r fixed while D was varied (between 39 and 61 cm) These results are presented in Figure 4.23. The solid line corresponds to an infinite plasma (with $k_{\|}/k_{\perp} = 0.015$) and therefore displays a constant growth rate independent of D. The dashed and dotted lines correspond to a parallel wave length of $2D$ and D (for uni- and bi-directional wave fronts respectively).

Measurements indicate that $\theta_k D/2 \leq \lambda/2$ for the growth rate data. Al-

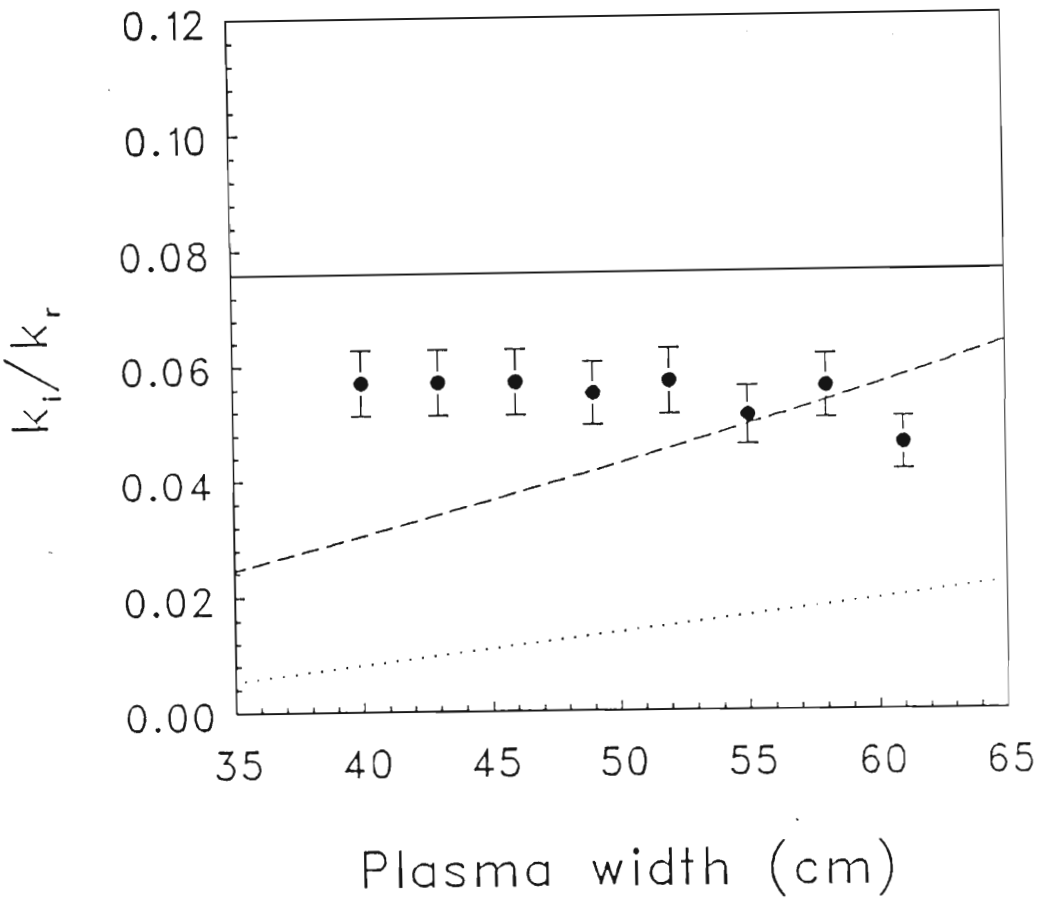

Figure 4.23: Normalized growth rate vs plasma diameter D, with: $k_r = 3$ cm^{-1}, $W_o = 35$ eV, $n_e = 1 \times 10^8$ cm^{-3}, $x = 18$ cm, $T_e = 2.7$ eV, $T_e/T_{ib} = 60$, $B = 23$ gauss and $\lambda_{ci}/\lambda_{ce} = 0.012$ The solid line is a theoretical fit to the data, assuming an unbounded plasma and $k_{\|}/k_{\perp} = 0.015$. The dashed and dotted-lines are theoretical curves assuming $\lambda = 2D$ and D respectively.

though this condition restricts growth rate (due to the lack of resonant electrons to participate in the wave motion), the measured growth rate value is only slightly less than that of the infinite plasma case. The results presented in Figures 4.22 and 4.23 indicate that the mechanism whereby the plasma width is limited is more involved than the theoretically expected dependence of the growth rate on the parallel dimension of the experimental device. A possible explanation is presented by BERTOTTI *et al.* [6] where a theoretical model is developed for the role of a sheath at the boundary wall on an ion instability. The authors conclude that the space charge boundary layer at the wall effectively shields the plasma and this enables it to appear unbounded. BARRETT *et al.* [5] investigated the growth rate of the CFIAI in two different plasma configurations and found that choosing $k_{\|} = \pi/D$ did not result in a good fit to their data. The authors speculated that the wave electric field falls off rapidly at the wall sheath, but the wavelength in the bulk of the plasma can be larger than $2D$.

4.9 Conclusion

The assumptions made in Chapter 2 concerning plasma gradients are supported by the experimental data on the steady state plasma. The primary collision mechanism has been identified as charge exchange and good agreement between experimental data and theory was obtained. This leads to the assumption that other collision types are negligible. Charge exchange collisions will cause the growth rate to decrease with distance into the plasma (see Figure 2.6), and therefore the growth rate measurements presented in this chapter are actually the average growth rate.

Good agreement is obtained between experiment and theory for the variation of growth rate with beam velocity, wave number and magnetic field. The theory does not adequately explain the growth rate at various values of the magnetic field angle. A qualitative explanation is presented based on the shape of the wave fronts. Spatial development of the wave fronts indicate that $k_{\|}/k_{\perp}$ depends on axial position.

The variation of plasma diameter is found not to affect growth rate, as the wave fronts appear to curve in such a manner as to enable electrons to neutralize regions of different wave potential. This is supported by the

theoretical curves in the previous sections, Figures 4.14, 4.15, 4.16 and 4.17, as they apply to an infinite plasma, whereas the experimental plasma was physically limited to a width D ($\approx$ 50 cm) by two stainless steel plates. The lack of dependence of growth rate on the physical width of the plasma can be explained in terms of a sheath effect at the side plates, effectively creating an infinite plasma.

Chapter 5

CONCLUSION

5.1 Summary of Thesis

5.1.1 Theory

Chapter 2 contains the derivation of the dispersion relation of the cross-field ion acoustic instability (CFIAI) with elastic and inelastic ion-neutral collisions included. By assuming T_{ib} , $T_{io} \ll T_e$, $\lambda_{ce} \gg \lambda_{ci}$ and $V_o \gg C_s$ the real part of the dispersion relation simplifies to

$$\frac{\omega_k^r}{k} = V_o \pm \sqrt{1-(x/\lambda_{ce})}\left(\sqrt{\frac{n_{oB}}{N_o}}\right)\frac{C_s}{\sqrt{1+k^2\lambda_D^2}}. \tag{5.1}$$

A physical explanation of the growth rate of the instability is presented in terms of inverse Landau damping. The theoretical chapter is concluded by a computational survey of the CFIAI. The growth rate (k_i/k_r) is examined as a function of the following parameters:

- Distance x into the plasma.
- Electron and ion temperature T_e, T_{iB}.
- Electron density n_e.
- Beam velocity V_o.
- Background ion temperature T_{io}.

- Magnetic field B.
- The angle θ_k between the beam and $\mathbf{k}$.
- Finite geometry.

5.1.2 Experiment

In Chapter 4 the experimental observations are presented. Data from a steady state plasma survey support the assumption of negligible plasma gradients. The primary collision mechanism is identified as charge exchange ion-neutral collisions. The following were the main results obtained:

- Using the dispersion relation (equation 5.1) good agreement between experiment and theory was obtained. The investigation was extended to cover a range of T_e.
- The growth rate k_i/k_r shows a cut off value for large values of $k_r\rho_e$.
- By reducing the beam velocity V_o, a cut off value in the growth rate is observed at $V_o/C_s \approx 2.5$.
- The growth rate data obtained at various values of k at two fixed values of magnetic field compare well with theory. Data obtained by varying B and keeping k fixed compare less well due to the magnetic field affecting other plasma parameters.
- Wave fronts were found to be slightly convex when viewed along the beam direction, i.e. with the central region lagging in phase. When $\mathbf{B}$ was rotated through an angle θ, the average direction of the wave vector $\mathbf{k}$ rotated in the same sense, through an angle $\theta_k \approx \theta/2$. The obliqueness of the wavefronts, $k_\parallel/k_\perp$, increases with axial distance x, until it reaches a limiting value at large x. The average value of $k_\parallel/k_\perp$ over the measurement region compares well with the theoretically fitted value.
- Growth rate data were measured as a function of magnetic field direction θ with parallel wave lengths set at $\lambda_\parallel \approx 2D$, and were compared to theory. It was found that the model was not adequate to describe the data. A discrepancy between data and theory was also found when the growth rate was examined as a function of the plasma width D.

5.2 Possible Extensions of this Project

The wave fronts of the instability were only examined in the **x**–**z** plane. The study can be extended to include all three dimensions. GREAVES [28] found that the CFIAI propagates at an oblique angle to the beam direction.

The growth rate values obtained in this present work are only average values as the growth rate changes with **x** and measurements were carried out over a region of **x**. Two probe measurements can solve this difficulty and provide much more information than can presently be obtained from an interferometer wave form.

Present work has centered around the linear regime of the CFIAI and can be extended to the non-linear regime. Plasma turbulence measurement techniques will also prove valuable in this study.

The experimental device was commissioned as a double plasma device for this project, but can easily be converted to a triple plasma device. This conversion will open up a relatively unexplored beam-plasma regime.

References

[1] AKIMOTO, K. and OMIDI, N., The Generation of Broadband Electrostatic Noise by an Ion Beam in the Magnetotail, *Geophysical Research Letters*, **13**, 97, 1986.

[2] ALLAN, W. and SANDERSON, J.J., Temperature Gradient Driven Ion Acoustic Instability, *Plasma Physics*, **16**, 753, 1974.

[3] AREFEV, V.I., Instability of a Current-carrying Homogeneous Plasma, *Soviet Physics: Tecknical Physics*, **14**, 1487, 1970.

[4] ASHBY, D.E.T.F. and PATON, A., A High Frequency Electrostatic Instability in a Magnetically Guided Plasma Stream, *Plasma Physics*, **9**, 359, 1967.

[5] BARRETT, P.J., FRIED, B.D., KENNEL, C.F., SELLEN, J.M., and TAYLOR, R.J., Cross-field Current-driven Ion Acoustic Instability, *Physical Review Letters*, **28**, 337, 1972.

[6] BERTOTTI, B., CAVALIERE, A. and GIUPPONI, P., Ion Waves in Bounded Plasma, *Physics of Fluids*, **9**, 265, 1966.

[7] BHARUTHRAM, R., Theoretical Studies of the Crossfield Current-driven Ion Acoustic Instability, Department of Physics, University of Natal, Durban, 1979.

[8] BHARUTHRAM, R. and HELLBERG, M.A., The Effects of Gradients on Electrostatic Instabilities in Collisionless Shocks, *Plasma Physics and Controlled Nuclear Fusion Research*, **2**, 693, (IAEA, Vienna, 1974.)

[9] BHARUTHRAM, R. and HELLBERG, M.A., The Effect of Magnetic Shear on the Crossfield Current-driven Ion-acoustic Instability, *Journal of Plasma Physics*, **28**, 255 1982.

[10] BHARUTHRAM, R., HELLBERG, M.A. and LEE, R.D., The Cross-field Current-driven Ion-acoustic Instability in a Collisional plasma, *Journal of Plasma Physics*, **28**, 358, 1982.

[11] BHATNAGAR, P.L., GROSS, E.P. and KROOK, M., A Model for Collision Processes in Gases, *Physical Review*, **94**, 511, 1954.

[12] BISKAMP, D., Ion Sound Turbulence in a Collisionless Shock Wave, *Journal of Geophysics Research, Space Physics*, **75**, 4659, 1970.

[13] BOYD, T.J.M. and SANDERSON, J.J., Plasma Dynamics, Nelson, 1969.

[14] BROWN, S.C., Basic Data for Plasma Physics, M.I.T. Press, 1961.

[15] CAVALIERE, A., ENGELMAN, F. and SESTERO, A., Propagation of Ion Waves in a Plasma Flow towards a Transonic Point, *Physics of Fluids*, **11**, 158, 1968.

[16] CHEN, F.F., Introduction to Plasma Physics and Controlled Fusion, Plenum, 1984.

[17] CHEN, F.F., ETIEVANT, C. and MOSHER, D., Measurement of Low Plasma Densities in a Magnetic Field, *Physics of Fluids*, **11**, 811, 1968.

[18] CLEMMOW, P.C. and DOUGHERTY, J.P., Electrodynamics of Particles and Waves, Addison-Wesley, 1969.

[19] D'ANGELO, N., Ion Beam Scattering by Ion-acoustic Turbulence, *Plasma Physics*, **21**, 973, 1979.

[20] FUSELIER, S.A. and GURNET, D.A., Short Wavelength Ion Waves Upstream of the Earth's Bow Shock, *Journal of Geophysical Research*, **89**, 91, 1984.

[21] FREDRICS, R.W., KENNEL, C.F., SCARF, F.L., CROOK, G.M. and GREEN, I.M., Detection of Electrostatic Field Turbulence in the Earth's Bow Shock, *Physical Review Letters*, **21**, 1761, 1968.

[22] FRIED, B.D. and CONTE, S.D., The Plasma Dispersion Function, Academic, 1961.

[23] GALLAGHER, D.L., Short-Wavelength Electrostatic Waves in the Earth's Magnetosheath, *Journal of Geophysical Research*, **90**, 1435, 1985.

[24] GARY, S.P., Longitudinal Waves in a Perpendicular Collisionless Plasma Shock, II, Vlasov Ions, *Journal of Plasma Physics*, **4**, 753, 1970.

[25] GARY, S.P., Longitudinal Waves in a Perpendicular Plasma Sheet, III, $T_e \approx T_i$, *Journal of Plasma Physics*, **6**, 561, 1971.

[26] GARY, S.P. and SANDERSON, J.J., Longitudinal Waves in a Perpendicular Collisionless Plasma Shock, I, Cold Ions, *Journal of Plasma Physics*, **4**, 739, 1970.

[27] GARY, S.P and OMIDI, N., The Ion-Ion Acoustic Instability, *Journal of Plasma Physics*, **37**, 45, 1987.

[28] GREAVES, R., Observations of the Crossfield Ion Acoustic Instability in three Dimensions, *MSc thesis*, Department of Physics., University of Natal, Durban, 1985.

[29] GRESILLON, D., DOVELL, F. and BUZZI, J.M., Space Correlation In Ion-Beam-Plasma Turbulence, *Physical Review Letters*, **34**, 197, 1975.

[30] HASEGAWA, A., Theory of Longitudinal Plasma Instabilities, *Physical Review*, **169**, 204, 1968.

[31] HAYZEN, A.J., The Crossfield Ion Acoustic Instability in a Beam Plasma System, PhD thesis, Department of Physics, University of Natal, Durban, 1976.

[32] HAYZEN, A.J., Electronic circuits, Internal report T76/1, Department of Physics, University of Natal, Durban, 1976.

[33] HAYZEN, A.J. and BARRETT, P.J., Cross-field Current-driven Ion Acoustic Instability in a Bounded Plasma with Collisions, *Physics of Fluids*, **20**, 1713, 1977.

[34] HIROSE, A., LONNGREN, K.E. and SKANGARD, H.M., Cross-field Ion-acoustic Instability Observed in a Turbulent Heating Experiment, *Physical Review Letters*, **28**, 270, 1970.

[35] JONES, R., Optimization and Performance of Electrostatic Particle Analyzers, *The Review of Scientific Instruments*, **49**, 21, 1978.

[36] JONES, R. and BARRETT, P.J., Nonlinear Cross-field Ion Acoustic Instability and Plasma Heating, *Physics of Fluids*, **23**, 956, 1980.

[37] KRALL, N.A. and TRIVELPIECE, A.W., Principles of Plasma Physics, McGraw-Hill, 1973.

[38] LASHMORE-DAVIES, C.N., A Possible Mechanism for Instability in a Perpendicular Collisionless Shock Wave, *Journal of Physics A*, **3**, L40, 1970.

[39] LASHMORE-DAVIES, C.N. and MARTIN, T.J., Electrostatic Instabilities Driven by an Electric Current Perpendicular to a Magnetic Field, *Nuclear Fusion*, **13**, 193, 1973.

[40] LEE, R.D., The Effect of Collisions on a Cross-field Current-driven Plasma Instability., Department of Physics, University of Natal, Durban, 1977.

[41] LEE, A. and SCHMIDT, G., Spatial Damping of Large Amplitude Waves, *Physics of Fluids*, **13**, 2546, 1970.

[42] LEMONS, D.S. , ASHBRIDGE, J.R. and BAME, S.J. *et al.*, The Source Of Electrostatic Fluctuations In The Solar Wind, *Journal of Geophysical Research*, **84**, 2135, 1979.

[43] LEUNG, K.N., COLLIER, R.D. and MARSHALL, L.B. *et al.*, Optimization and Performance of Electrostatic Particle Analyzers, *The Review of Scientific Instruments*, **49**, 21, 1978.

[44] PRIEST, E.R. and SANDERSON, J.J., Ion-acoustic Instability in Collisionless Shocks, *Plasma Physics*, **14**, 951, 1972.

[45] ROSA, R. and ALLEN, J.E., One-dimensional Ion-acoustic modes of Bounded Plasmas, *Journal of Plasma Physics*, **4**, 195, 1970.

[46] SINGH, P., A Study of the Interaction of Strong Electromagnetic Waves and Anisotropic Ion Beams with a Background Plasma, Department of Physics, University of Durban Westville, Durban, 1989.

[47] STRINGER, T.E , Electrostatic Instabilities In Current-carrying and Counter streaming Plasmas, *Plasma Physics*, **6**, 267, 1964.

[48] TAYLOR, J.B. and LASHMORE-DAVIES, C.N., Plasma Stabilization by Feedback, *Physical Review Letters*, **24**, 1340, 1970.

[49] TAYLOR, R.J., MACKENZIE, K.R. and IKEZI, H., A Large Double Plasma Device for Plasma Beam and Wave Studies, *The Review of Scientific Instruments*, **43**, 1675, 1972.

[50] WONG, H.V., Electrostatic Electron-ion Instability, *Physics of Fluids*, **13**, 757, 1970.